JOINT TRANSPORTATION
RESEARCH PROGRAM
INDIANA DEPARTMENT OF TRANSPORTATION
AND PURDUE UNIVERSITY

CPT-Based Geotechnical Design Manual, Volume 2: CPT-Based Design of Foundations—Methods

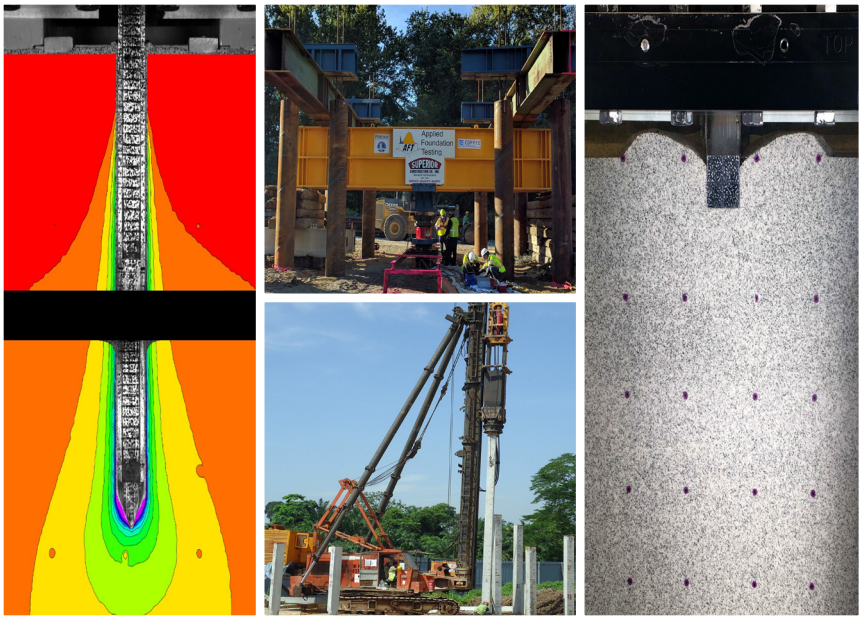

Venkata A. Sakleshpur, Monica Prezzi,
Rodrigo Salgado, Mir Zaheer

SPR-4108 • Report Number: FHWA/IN/JTRP-2021/23 • DOI: 10.5703/1288284317347

RECOMMENDED CITATION

Sakleshpur, V. A., Prezzi, M., Salgado, R., & Zaheer, M. (2021). *CPT-based geotechnical design manual, Volume 2: CPT-based design of foundations—Methods* (Joint Transportation Research Program Publication No. FHWA/IN/JTRP-2021/23). West Lafayette, IN: Purdue University. https://doi.org/10.5703/1288284317347

AUTHORS

Venkata A. Sakleshpur
Graduate Research Assistant
Lyles School of Civil Engineering
Purdue University

Rodrigo Salgado, PhD
Charles Pankow Professor of Civil Engineering
Lyles School of Civil Engineering
Purdue University

Monica Prezzi, PhD
Professor of Civil Engineering
Lyles School of Civil Engineering
Purdue University
(765) 494-5034
mprezzi@ecn.purdue.edu
Corresponding Author

Mir Zaheer, PE
Geotechnical Design Engineer
Indiana Department of Transportation

JOINT TRANSPORTATION RESEARCH PROGRAM

The Joint Transportation Research Program serves as a vehicle for INDOT collaboration with higher education institutions and industry in Indiana to facilitate innovation that results in continuous improvement in the planning, design, construction, operation, management and economic efficiency of the Indiana transportation infrastructure. https://engineering.purdue.edu/JTRP/index_html

Published reports of the Joint Transportation Research Program are available at http://docs.lib.purdue.edu/jtrp/.

NOTICE

ACKNOWLEDGEMENTS

This research was funded with the support provided by the Indiana Department of Transportation (INDOT) through the Joint Transportation Research Program (JTRP) at Purdue University. The authors would like to thank the agency for the support. The authors are very grateful for the support received from the project administrator, Peter Becker, the business owner, Athar Khan, and the study advisory committee, composed of Samy Noureldin and Jose Ortiz, throughout the duration of the project and for their valuable comments and suggestions. The authors are very grateful to Barry Partridge and Darcy Bullock for their valuable support throughout the project. Special thanks are due to Alebachew Tilahun, Jonathan Paauwe, and Nayyar Zia Siddiki for sharing the soil investigation data for sites in Indiana, and to Kamran Ghani, Min Sang Lee, and Victoria Leffel for their comments. The authors would also like to thank Daniel Alzamora and Derrick Dasenbrock from the Federal Highway Administration (FHWA) for their detailed comments and suggestions.

TECHNICAL REPORT DOCUMENTATION PAGE

1. Report No. FHWA/IN/JTRP-2021/23	**2. Government Accession No.**	**3. Recipient's Catalog No.**
4. Title and Subtitle CPT-Based Geotechnical Design Manual, Volume 2: CPT-Based Design of Foundations—Methods		**5. Report Date** June 2021 **6. Performing Organization Code**
7. Author(s) Venkata A. Sakleshpur, Monica Prezzi, Rodrigo Salgado, and Mir Zaheer		**8. Performing Organization Report No.** FHWA/IN/JTRP-2021/23
9. Performing Organization Name and Address Joint Transportation Research Program Hall for Discovery and Learning Research (DLR), Suite 204 207 S. Martin Jischke Drive West Lafayette, IN 47907		**10. Work Unit No.** **11. Contract or Grant No.** SPR-4108
12. Sponsoring Agency Name and Address Indiana Department of Transportation (SPR) State Office Building 100 North Senate Avenue Indianapolis, IN 46204		**13. Type of Report and Period Covered** Final Report **14. Sponsoring Agency Code**

15. Supplementary Notes

Conducted in cooperation with the U.S. Department of Transportation, Federal Highway Administration.

16. Abstract

This manual provides guidance on how to use the cone penetration test (CPT) for site investigation and foundation design. The manual has been organized into three volumes. Volume 1 covers the execution of CPT-based site investigations and presents a comprehensive literature review of CPT-based soil behavior type (SBT) charts and estimation of soil variables from CPT results. Volume 2 covers the methods and equations needed for CPT data interpretation and foundation design in different soil types, while Volume 3 includes several example problems (based on instrumented case histories) with detailed, step-by-step calculations to demonstrate the application of the design methods. The methods included in the manual are current, reliable, and demonstrably the best available for Indiana geology based on extensive CPT research carried out during the past two decades. The design of shallow and pile foundations in the manual is based on the load and resistance factor design (LRFD) framework. The manual also indicates areas of low reliability and limited knowledge, which can be used as indicators for future research.

17. Key Words cone penetration test, soil behavior type, shallow foundation, pile foundation, load and resistance factor design	**18. Distribution Statement** No restrictions. This document is available through the National Technical Information Service, Springfield, VA 22161.

19. Security Classif. (of this report) Unclassified	**20. Security Classif. (of this page)** Unclassified	**21. No. of Pages** 97 including appendices	**22. Price**

EXECUTIVE SUMMARY

Introduction

This manual provides guidance on how to use the cone penetration test (CPT) for site investigation and foundation design. The manual has been organized into three volumes.

Volume I covers the execution of CPT-based site investigations, a comprehensive literature review of CPT-based soil behavior type (SBT) charts, and several correlations for the estimation of a soil variable of interest from CPT results. The volume has been organized into two chapters. Chapter 1 details the components of a CPT system, types of CPT equipment, testing procedures and precautions, maintenance of CPT equipment, and planning and execution of a CPT-based site investigation. Chapter 2 presents a compilation of correlations for the estimation of a soil variable of interest from CPT data, and also presents a comprehensive review of the chronological development of the SBT classification systems that have advanced during the past 55 years of CPT history.

Volume II covers the methods and equations needed for CPT data interpretation and foundation design in different soil types. The volume has been organized into four chapters. Chapter 1 provides an introduction to the manual. Chapter 2 presents an overview of Indiana geology, the typical CPT and soil profiles found in Indiana, and the influence of these profiles on CPT-based site variability assessment. Chapter 3 details the methods for estimation of limit bearing capacity and settlement of shallow foundations from CPT data. Chapter 4 describes the methods for estimation of limit unit shaft resistance and ultimate unit base resistance of displacement, non-displacement, and partial displacement piles and pile groups from CPT data. The design of both shallow and pile foundations is based on the load and resistance factor design (LRFD) framework.

Volume III contains several example problems (based on case histories) with detailed, step-by-step calculations to demonstrate the application of the CPT-based foundation design methods covered in Volume II. The volume has been organized into three chapters. Chapter 1 includes example problems for the estimation of optimal spacing between CPT soundings performed in line and distributed in two dimensions using CPT data obtained from the Sagamore Parkway Bridge construction site in Lafayette, Indiana. Chapter 2 contains example problems for the estimation of limit bearing capacity and settlement of shallow foundations using CPT data reported in literature for sites in the US, UK, and Australia. Chapter 3 includes example problems for the estimation of limit unit shaft resistance and ultimate unit base resistance of displacement, non-displacement, and partial displacement piles using CPT data obtained from three sites in Indiana. The predicted foundation load capacities and settlements were found to be in agreement with the measured load test data reported for these sites.

Findings

Not applicable.

Implementation

The *CPT-Based Geotechnical Design Manual* can be used to train new employees and to facilitate interaction between INDOT engineers, industry, and consultants. Specific implementation items for each volume are listed below.

Volume I

A spreadsheet for the estimation of fundamental soil variables from CPT results was developed. INDOT engineers can use the spreadsheet on a routine basis to interpret CPT data, generate an SBT profile, and obtain the depth profile of a soil property of interest.

Volumes II and III

Spreadsheets for the estimation of optimal spacing between CPT soundings and CPT-based design of shallow and pile foundations were developed. INDOT engineers can use the spreadsheets on a routine basis for the design of transportation infrastructure projects in Indiana.

A relationship between cone resistance q_c, corrected SPT blow count N_{60}, and mean particle size D_{50} was developed using data reported by Robertson et al. (1983) and data obtained from 15 sites in Indiana. The relationship can be used to obtain an estimate of q_c for use in a CPT-based foundation design method when only SPT blow counts are available for a site.

A relationship between critical-state friction angle ϕ_c, mean particle size D_{50}, coefficient of uniformity C_U, and particle roundness R was developed using test data reported for 23 clean silica sands in the literature. In the absence of direct shear or triaxial compression test results, the relationship can be used to obtain an estimate of ϕ_c for poorly-graded, clean silica sands with D_{50}, C_U, and R values ranging from 0.15–2.68 mm (0.006–0.105 in.), 1.2–3.1, and 0.3–0.8, respectively.

CONTENTS

LIST OF TABLES

LIST OF FIGURES

1. INTRODUCTION

1.1 Background

Site investigation is an important component of every infrastructure project and plays a vital role in project planning, design, and construction. It is akin to diagnosing patients in medicine because a project site's pathology (i.e., the origin, type, spatial distribution, and properties of soil and rock layers) is evaluated for engineering purposes (Madhav & Abhishek, 2016, 2017). The main goals of a geotechnical site investigation are to: (1) identify soil and rock stratigraphy, (2) establish groundwater level conditions, and (3) estimate geotechnical design parameters (e.g., strength and stiffness). Although site investigations involve both soil and rock characterization, this manual focuses solely on soil investigations performed using the cone penetration test (CPT).

Over the past two to three decades, *in situ* tests have gained favor over laboratory tests because: (1) *in situ* tests are generally faster to perform than laboratory tests, and (2) laboratory test results are affected by sample disturbance and represent the properties of only a few points within a stratum. In contrast, *in situ* tests, particularly the CPT, significantly increase the volume of material investigated at a site and produce more reliable and repeatable data, thus resulting in substantial cost and time savings.

Among available *in situ* tests, the standard penetration test (SPT) and the cone penetration test (CPT) are the most commonly used tests in practice. The SPT is a crude test that involves driving a standard split-spoon sampler into the ground a distance of 450 mm (18 in.) from multiple blows using a 630 N (140 lb) hammer dropped from a height of 760 mm (30 in.) (Figure 1.1). The number of blows required for the last 300 mm (12 in.) of penetration of the sampler, after an initial seating drive of 150 mm (6 in.), is recorded as the raw SPT blow count N_{SPT} for the tested depth.

The SPT blow count is affected by energy inefficiencies in the drop hammer system and other factors, such as the effects of the operator, rod length, sampler type, and borehole diameter (Ireland et al., 1970). Although corrections have been proposed to normalize the N_{SPT} value with respect to these factors (Anderson et al., 2004; Kulhawy & Mayne, 1990; Skempton, 1986), the reliability of the SPT remains quite low as test results are likely to vary between different crews operating the same equipment (Look, 2016; Look et al., 2015) (Figure 1.2). Consequently, the CPT is gradually replacing the SPT as the preferred *in situ* test for site investigations. The greater availability of powerful CPT rigs has made it easier for engineers to require that CPTs be performed as part of site investigations. Another reason for the increasing reliance on the CPT is the development of sophisticated and reliable foundation design methods based on CPT data.

The CPT is a quasi-static test and is often used as a complement to conventional rotary drilling and sampling methods. The test is performed by pushing a

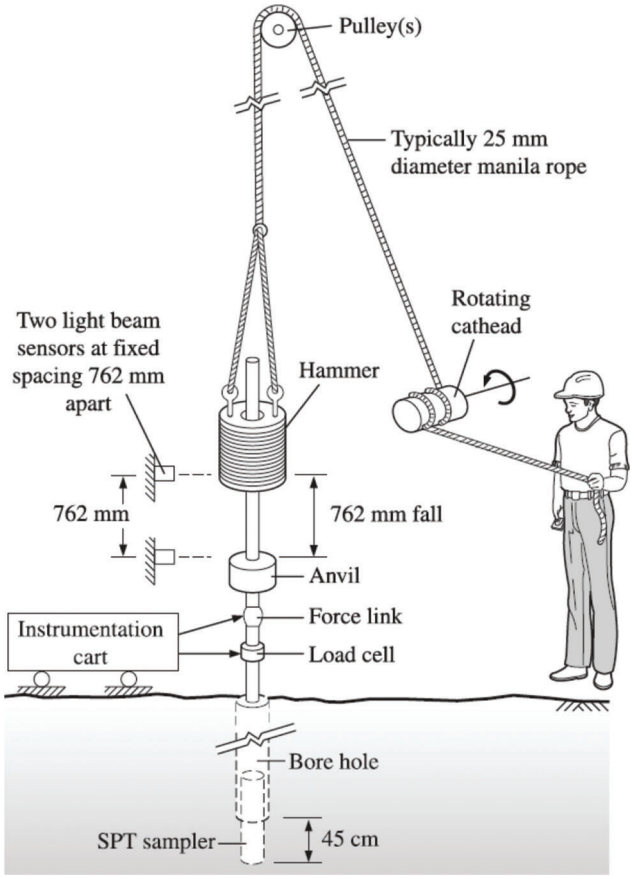

Figure 1.1 Schematic of SPT in progress (Salgado, 2008; USACE, 2001).

penetrometer having a conical tip with 60° apex angle vertically into the ground at a standard rate of 20 mm/s (0.8 in./s) (ASTM, 2012) (Figure 1.3). The penetrometer is connected to the lowest rod among a string of rods pushed down from a truck-mounted, crawler-mounted, or trailer-mounted rig. The cone penetrometer was originally used to measure only the tip or cone resistance q_c, defined as the vertical force acting on the tip of the penetrometer divided by the base area of the tip. The base area of the cone tip is equal to 1,000 mm^2 (1.55 $in.^2$) for typical penetrometers that are in compliance with ASTM (2012), although penetrometer sizes in practice can vary greatly.

Over the years, different sensors have been incorporated into the cone to measure sleeve resistance f_s, shear wave velocity V_s, pore water pressure u, and other parameters (Campanella & Weemees, 1990; Mayne & Campanella, 2005; Mitchell, 1988; Robertson et al., 1986). The CPT data is generally recorded at 1-to-5-cm (0.4-to-2-in.) intervals of cone penetration (ASTM, 2012); however, the data can also be recorded at every 0.2 cm (0.08 in.) of cone penetration depending on the level of sophistication of the penetrometer and the data acquisition system (Salgado et al., 2015). The data is directly logged to a field computer in real-time and can be used to estimate geostratigraphy, soil types, water table elevation, and geotechnical design parameters of interest.

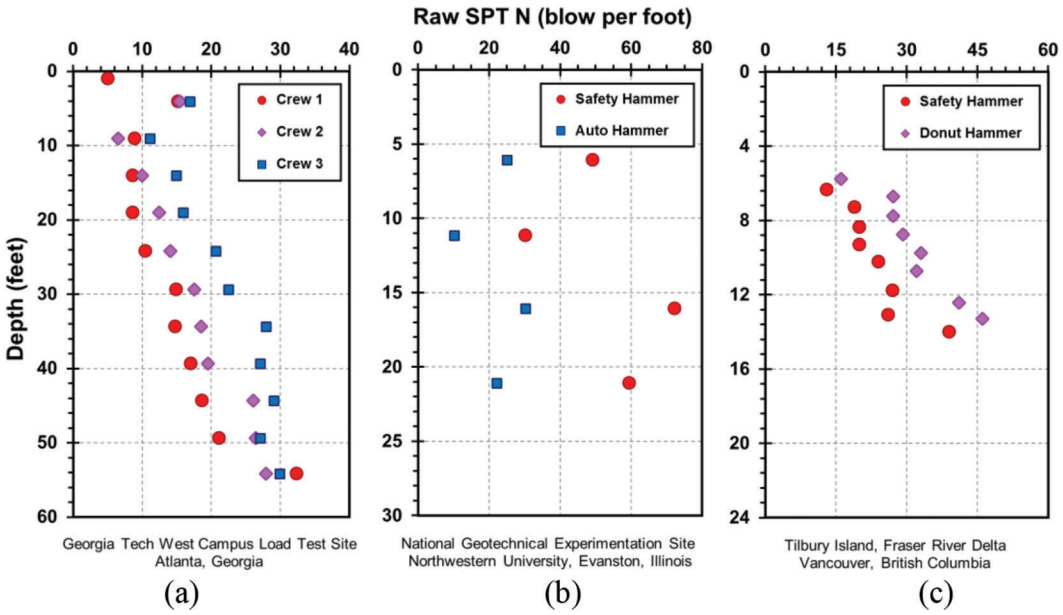

Figure 1.2 Comparison of N_{SPT} values obtained: (a) by different crews using the same SPT equipment (adapted from Mayne & Harris, 1993), (b) using safety and auto hammers (adapted from Finno, 1989), and (c) using safety and donut hammers (adapted from Robertson et al., 1983).

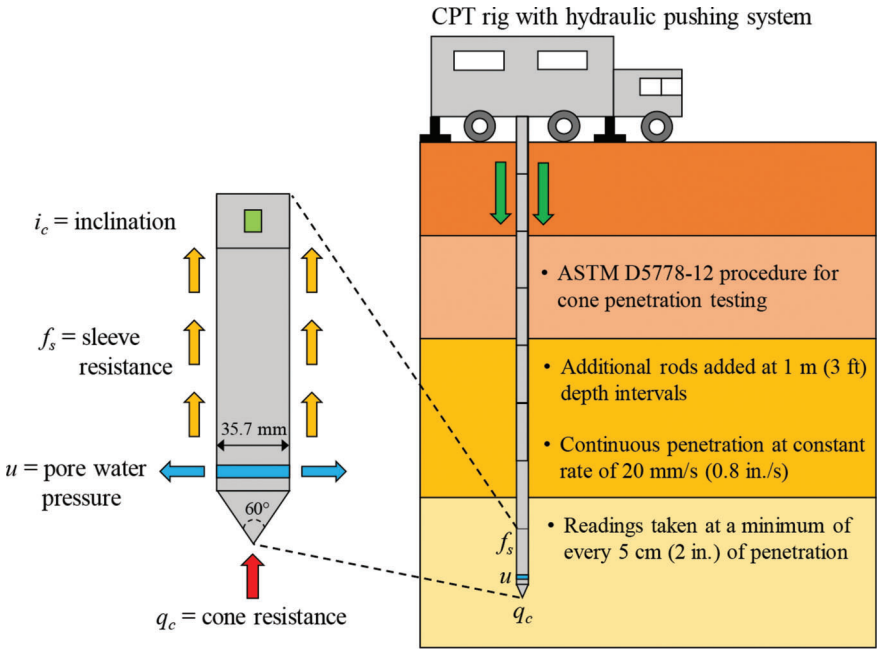

Figure 1.3 Overview of the cone penetration test (after ASTM, 2012).

Figure 1.4 shows a typical CPT log, which always contains the cone resistance q_c and sleeve resistance f_s plotted as a function of depth; it may contain more information if additional measurements are made. Sleeve friction or sleeve resistance f_s is defined as the ratio of the shear force acting along the surface of the cylindrical friction sleeve located above the cone tip to the circumferential area of the sleeve. The circumferential area of the sleeve is equal to 15,000 mm^2 (23.25 in.^{2}) in the standard cone (ASTM, 2012). Sleeve resistance was originally thought of as being useful for estimating pile shaft resistance; however, by means of the friction ratio f_s/q_c, it has more often been used as an indicator of the type of soil through which the cone is advanced (Lunne et al., 1997). In general, a combination of low q_c values and high friction ratio f_s/q_c suggests a clayey soil, whereas for sandy soils, q_c tends to be high and f_s/q_c low (Salgado, 2008). Volume I reviews the charts available in the literature for estimating soil behavior type (SBT) from CPT results.

The seismic piezocone penetration test (SCPTu), a newer version of the CPT, is a hybrid geotechnical-geophysical *in situ* test that provides downhole geophysical measurements of shear wave velocity V_s at 1-m-depth intervals in addition to the regular penetration test data obtained at 1-to-5-cm (0.4-to-2-in.) depth intervals (Campanella et al., 1986; Mayne, 2007; Mayne & Campanella, 2005; Robertson et al., 1986). Figure 1.5 shows the results obtained from a SCPTu sounding performed up to a depth of 95 m (312 ft) at the Golden Ears Bridge site in Vancouver, Canada. Such high-quality subsurface data can be efficiently used to delineate the geostratigraphy of a site and obtain the required geotechnical parameters for use in foundation design.

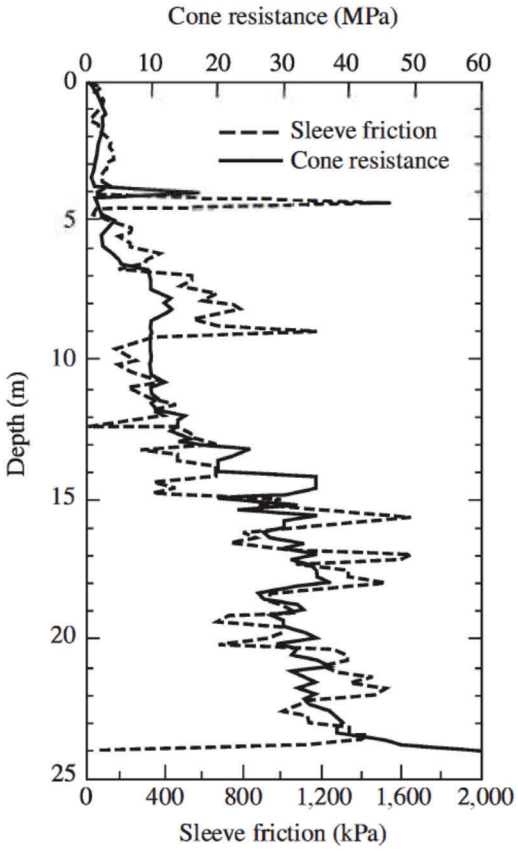

Figure 1.4 Typical CPT log (Salgado, 2008).

In its simplest application, the CPT offers a quick, expedient, and economical way to characterize the ground conditions at a site. According to Mayne (2007), a 10-m (30-ft)-deep CPT sounding can be completed in about 15–20 minutes, whereas a conventional soil boring takes about 3–6 times longer to complete. Since soil samples are not collected and spoils are not generated during testing, the CPT is less disruptive from an environmental standpoint and thus advantageous when investigating environmentally sensitive areas and potentially contaminated sites where the risk of exposure to hazardous material is high (Campanella & Weemees, 1990; Fukue et al., 2001; McKnight et al., 2015; Mondelli et al., 2010; Walker et al., 2009). The CPT can be performed in most soil types, ranging from soft-to-stiff clays and loose-to-dense sands, and silts, but can be difficult to perform in terrain containing gravels, cobbles, boulders, or other such obstacles to penetration (Han et al., 2019a,b). Nonetheless, the almost continuous CPT data permit clear delineations of soil strata including the thickness and lateral extent of each layer. In addition, the penetration process is amenable to theoretical modeling, even if the level of sophistication of the required analyses is such that it remains a topic of advanced research. The penetration resistance can be either correlated with other geotechnical parameters or used

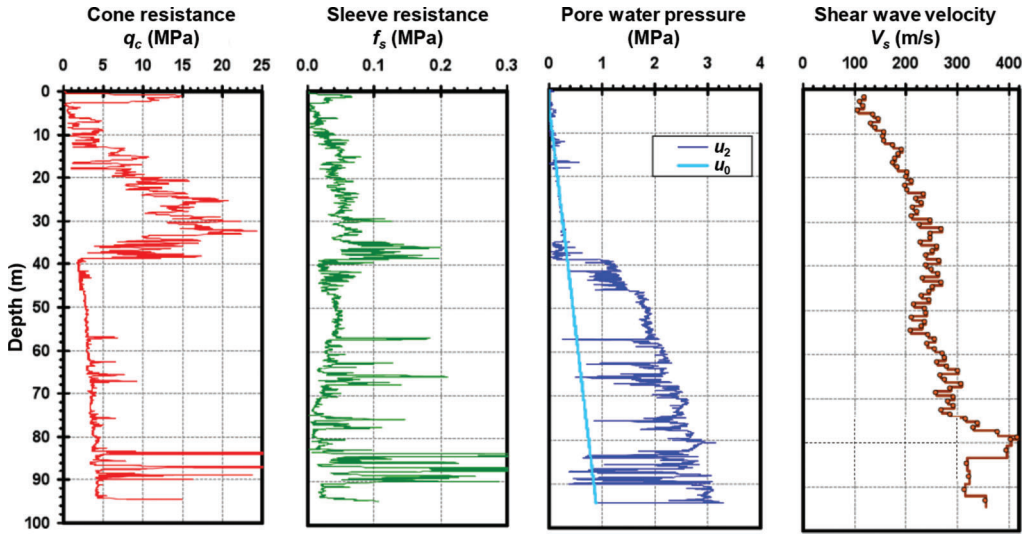

Figure 1.5 Results obtained from a SCPTu sounding performed at the Golden Ears Bridge site in Vancouver, Canada (adapted from Niazi et al., 2010).

directly in design; however, its use in design and interpretation remains a research need.

Soil properties used in geotechnical design are often estimated from a limited number of *in situ* or laboratory tests (due to project budget and time constraints) and are thus subject to uncertainty, raising the question as to how accurately the soil properties derived from these tests represent those of the entire site (Madhira & Sakleshpur, 2018, 2019). Although this uncertainty cannot be eliminated, it can be addressed by quantifying the variability within individual soundings and of clusters of soundings at a site. Because the CPT is a more reliable tool than the SPT, it can be used for both site variability assessment (Salgado et al., 2015, 2019) and load and resistance factor design (LRFD) of foundations (Basu & Salgado, 2012; Han et al., 2015).

1.2 Aim of the Manual

There is a myriad of CPT correlations and CPT-based design protocols in the literature; these correlations and protocols appear in software, producing interpretation results that may be confounding. This leads to confusion among consultants as to which method(s) to use for estimation of soil variables and design of geotechnical structures based on CPT results. This manual does not aim to be an exhaustive review of all that can be done with the CPT or of all the possible ways in which CPT results can be used in geotechnical engineering. The purpose of this manual, written in concise, objective language, is to provide guidance on how to use the CPT specifically for site investigation and foundation design. The primary focus of the manual is on methods that are current, reliable, and demonstrably the best available for Indiana geology based on extensive CPT research carried out during the past two decades. The manual also indicates areas of low reliability and limited knowledge, which can be used as indicators for future research.

1.3 Organization of the Manual

The manual has been organized into three volumes. Volume I contains two chapters—Chapter 1 details the components of a CPT system, types of CPT equipment, testing procedures and precautions, maintenance of CPT equipment, and planning and execution of a CPT-based site investigation. Chapter 2 presents a comprehensive literature review of (a) estimation of soil variables from CPT results and (b) soil behavior type (SBT) charts.

Volume II contains four chapters—Chapter 1 provides an introduction to the manual. Chapter 2 presents an overview of Indiana geology, the typical CPT and soil profiles found in Indiana, and the influence of these profiles on CPT-based site variability assessment. Chapter 3 details the methods for estimation of limit bearing capacity and settlement of shallow foundations from CPT data. Chapter 4 describes the methods for estimation of limit unit shaft resistance and ultimate unit base resistance of displacement, nondisplacement, and partial displacement piles and pile groups from CPT data.

Volume III contains several example problems (based on instrumented case histories) with detailed, step-by-step calculations to demonstrate the application of some CPT-based foundation design methods covered in Volume II.

2. CONSIDERATION OF INDIANA GEOLOGY ON CPT-BASED SITE INVESTIGATIONS

2.1 Overview of Indiana Geology

2.1.1 Bedrock Geology

Indiana's bedrock geology has three important aspects—the first being the topography of the bedrock surface. The bedrock of Indiana has undergone erosion since about 300 million years ago, but it was only during the Ice Age that unconsolidated sediments were deposited over the bedrock due to glacial advances and retreats across the state. The Ice Age, also known as Pleistocene, is a geologic time period that began about two million years ago and ended 10,000 years ago; during this period, the Earth's higher and mid-latitude zones experienced extensive glaciation by large, continental-scale ice sheets (Wilson, 2008). Thus, the bedrock surface is usually not visible in Indiana because nearly two-thirds of the state is covered by glacial material. According to the Indiana Geological and Water Survey (IGWS), Indiana's bedrock is exposed only in the south-central part of the state, which is unglaciated, and in localized areas along the Wabash River—the highest points of the bedrock surface are in Randolph and Wayne counties, while the lowest points are along the Wabash and Ohio Rivers in Posey and Vanderburgh counties.

The types of rocks and their spatial distribution form the second aspect of Indiana's bedrock geology. Figure 2.1 shows the bedrock geologic map of Indiana, which consists of five bedrock units: Pennsylvanian, Mississippian, Devonian, Silurian, and Ordovician units. Each unit or formation is tens to hundreds of feet thick and consists primarily of sedimentary rocks, such as limestone, dolomite, shale, sandstone, and siltstone. Each of these sedimentary rocks weathers at a different rate and produces unique weathering byproducts. For instance, carbonaceous rocks, such as limestone and dolomite, dissolve slowly in acid rain and snow to produce sinkholes, caves, and other features collectively known as karst (West, 2010; White, 1988). Such soluble rocks having karst or the potential to develop karst features account for about 18% of the land area of the United States (Weary & Doctor, 2014).

Figure 2.2 shows the karst regions in southern Indiana, which include the Mitchell and Muscatatuck Plateaus, the Crawford and Norman Uplands, and the Charlestown Hills area. The Mitchell Plateau in south-central Indiana is a karst plateau developed on

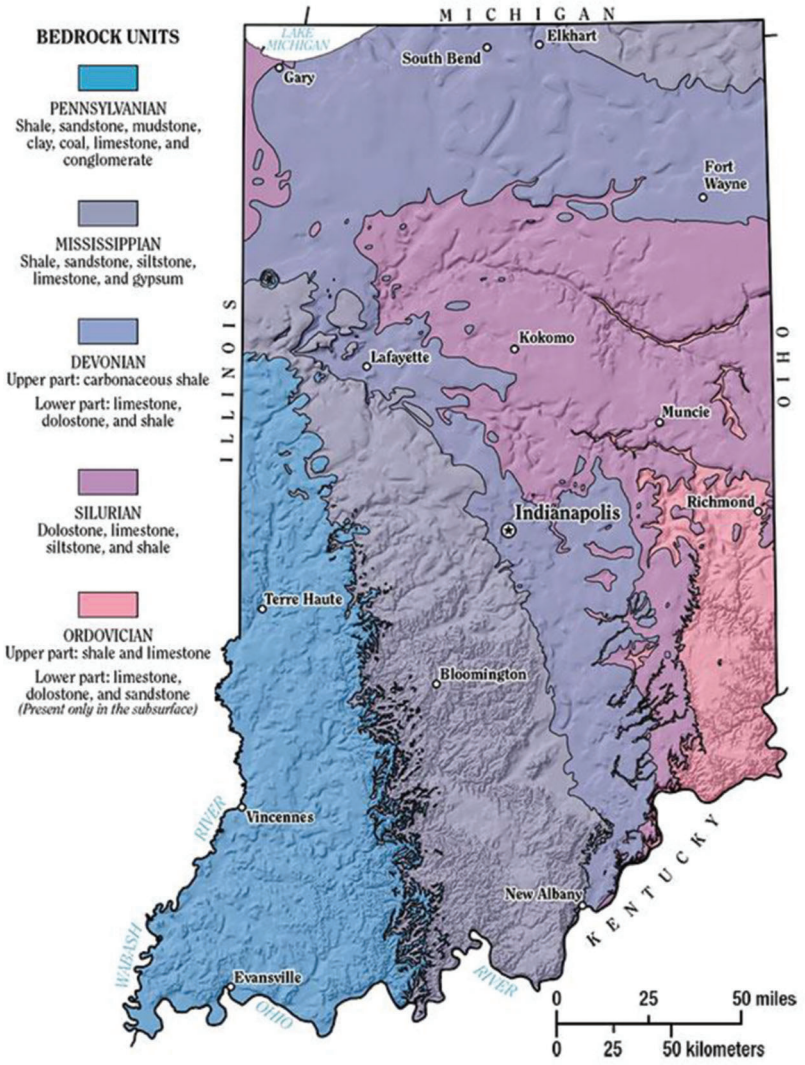

Figure 2.1 Bedrock geologic map of Indiana (Source: IGWS, n.d.).

Mississippian carbonates and extends from the eastern part of Owen County down south to the Ohio River in Harrison County and then into Kentucky (Florea et al., 2018; Gray, 2000; Malott, 1922). The Crawford Upland lies to the west of the Mitchell Plateau and is characterized by ridges and valleys developed on shale, sandstone, and carbonate strata of Mississippian age (Florea et al., 2018). Karst features have also been detected along the western margin of the Norman Upland to the east of the Mitchell Plateau as well as in carbonate strata of Silurian and Devonian age in the Muscatatuck Plateau and the Charlestown Hills area in southeastern Indiana (Gray, 2000) (Figure 2.2). Karst presents difficulties and challenges to geotechnical engineers due to the presence of underground cavities that may collapse, forming sinkholes. Figure 2.3 and Figure 2.4 show photographs of sinkholes in Lawrence County and near the Salem Bypass in Washington County, respectively, in Indiana.

The third aspect of Indiana's bedrock geology is the presence of bends and faults in the stratigraphic units. Figure 2.5 shows the tectonic features of Indiana. The Kankakee Arch and the Cincinnati Arch constitute a broad anticline, which extends from the northwestern to the southeastern part of the state (Rupp, 1991). This anticline is intersected by two faults: the Royal Center Fault and the Fortville Fault. Apart from these two faults, there is the Mt. Carmel Fault (in the Leesville anticline) that extends from Morgan County south through Monroe and Lawrence counties into Washington County, and finally, a concentrated region of faults in the southwestern part of the state called the Wabash Fault Valley System (Ault & Sullivan, 1982; Hildenbrand & Ravat, 1997; René & Stanonis, 1995; Woolery et al., 2018). In general, Indiana is tectonically quiet with practically insignificant movement of the bedrock (Rupp, 1991).

2.1.2 Surficial Geology

Figure 2.6 shows the surficial geologic map of Indiana, which can be broadly divided into four regions

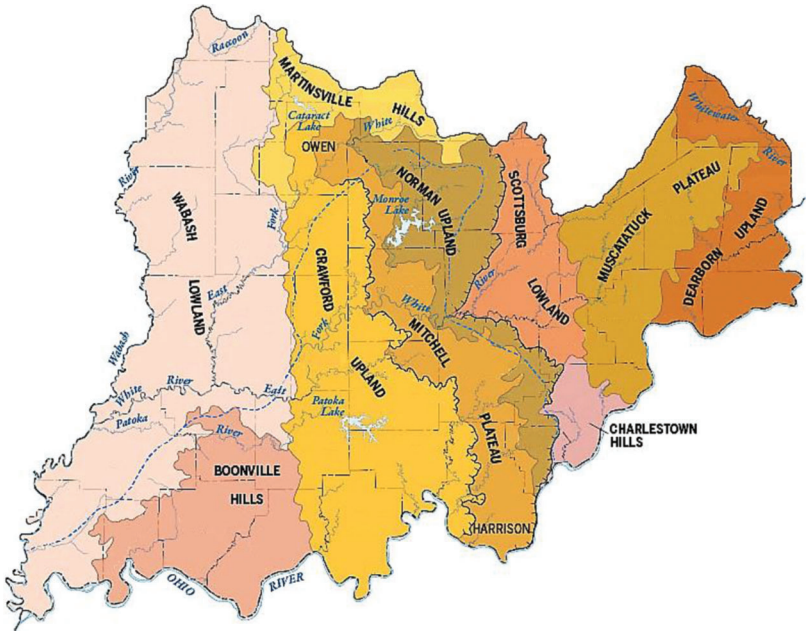

Figure 2.2 Physiographic divisions of southern Indiana (adapted from Gray, 2000).

Figure 2.3 Sinkhole in Mississippian carbonate rock of Mitchell Plateau in Lawrence County, Indiana (Frushour, n.d., as cited in Hasenmueller & Packman, n.d.).

Figure 2.4 Close-up view of a sinkhole near Salem Bypass in Washington County, Indiana (T. Colglazier & N. Z. Siddiki, personal communication, November 14, 2017).

(from north to south) based on the type of deposit encountered. Firstly, large deposits of dune sand, or sand dunes, exist in northern Indiana, particularly along the Lake Michigan shoreline and along the eastern margins of the Wabash and White Rivers (Argyilan et al., 2018; Cressey, 1928; Hill, 1974; Kilibarda & Blockland, 2011; Kilibarda & Shillinglaw, 2014). Secondly, outwash, which is a sorted and stratified mixture of sand and gravel particles transported and deposited by glacial meltwater, exists in northern Indiana and along major river valleys, such as the Eel, Kankakee, Whitewater, Wabash, White, and Ohio Rivers (Logan et al., 1922). Thirdly, glacial till, which is an unsorted, unstratified and heterogeneous mixture of clay-to-boulder size particles deposited by ice, forms flat to hummocky plains in central Indiana (Colgan et al., 2003; Fleming et al., 1993; Gooding, 1973; Loope et al., 2018; Wayne & Thornbury, 1951). These glacial till plains are partly bisected by end moraines, which are long, arcuate ridges of till, in northeastern Indiana (Brown, 2016; Kassab et al., 2017; Wayne, 1965). Finally, thick loess deposits, which contribute to soil fertility, lie east of the Wabash and White Rivers and south of the Wisconsin glacial boundary, as shown in Figure 2.7 (Hall & Anderson, 2000; Kim & Kang, 2013; Shaw, 1915).

Loess is an unstratified, aeolian sediment that consists mostly of silt with small fractions of clay (smectite) and fine sand (quartz/feldspar) along with light carbonate cementation (calcite $\leq$ 30%) at inter-particle contacts (Mitchell & Soga, 2005). Loess deposits are typically characterized by low water content ($\approx$ 10%), low density ($\approx$ 1.2 g/cm^3 or 74.9 lb/ft^3), and loose

Figure 2.5 Map showing the tectonic features in Indiana (Rupp, 1991).

metastable fabric (void ratio = 0.67–1.50)—they are strong and incompressible when dry, as evidenced by several stable vertical cliffs found around the world, but are collapsible either with saturation alone or with saturation and loading (Krinitzsky & Turnbull, 1967; Mitchell & Soga, 2005; Rutledge et al., 1996). In addition to the aforementioned soil types, organic soils, such as peat (with organic content > 30%), are commonly found in the Northern Lake Moraine Physiographic Region in northern Indiana and occasionally in central Indiana as well (Wilcox et al., 1986; Wilcox & Simonin, 1988).

2.2 CPT, SPT, and Soil Profiles in Indiana

One of the primary applications of the cone penetration test is stratigraphic profiling. Figure 2.8 shows the distribution of different soil types in Indiana and 10 select locations where CPTs were performed by the Indiana Department of Transportation (INDOT), the United States Geological Survey (USGS), and Purdue University. Table 2.1 summarizes the geographic details of the CPT locations marked in Figure 2.8. The locations were selected from different parts of the

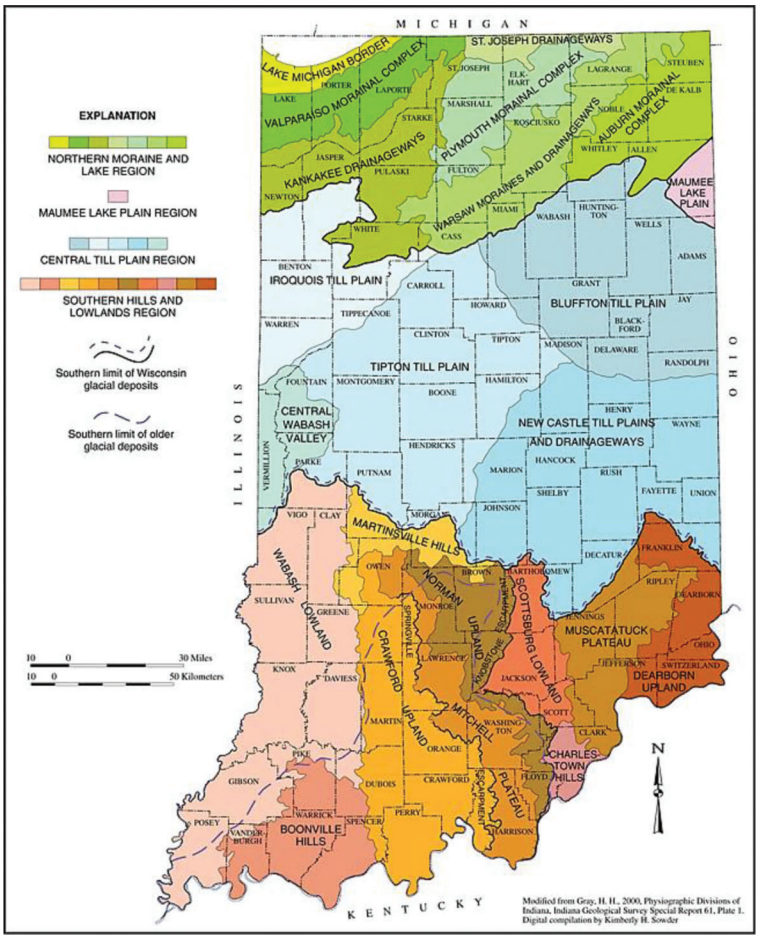

Figure 2.6 Surficial geologic map of Indiana (after Gray, 2000).

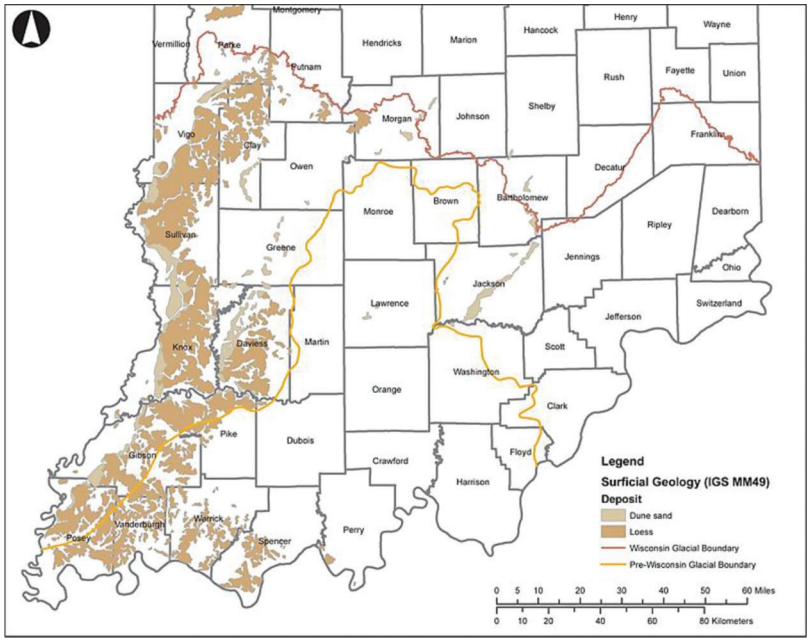

Figure 2.7 Map of southern Indiana showing the distribution of loess deposits (> 1.5 m (5 ft) in thickness) (Source: Gray, n.d.).

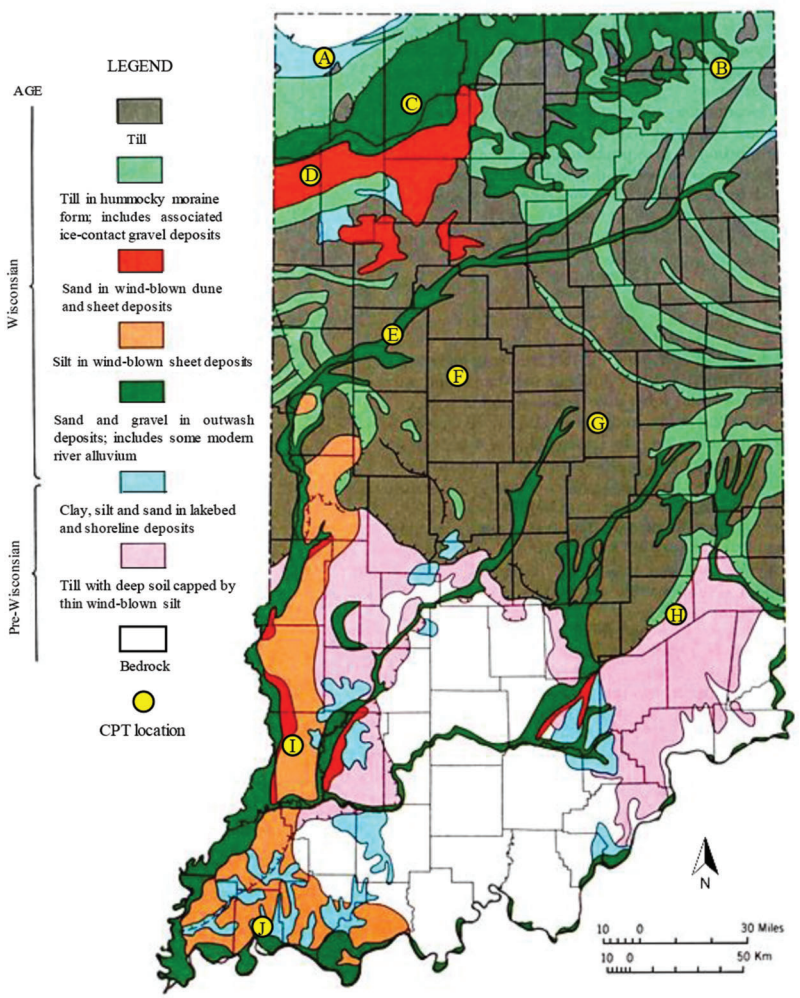

Figure 2.8 Pedological map of Indiana showing the CPT locations.

TABLE 2.1
Geographic information of the CPT locations in Indiana

Notation	Soil Type	County	Approximate Location Details	Latitude	Longitude
A	Dune sand	Lake	On SR-51/US-6, 900 ft south of I-90	41.5903	-87.2403
B	Till in hummocky moraine form	Steuben	On SR-4 over Little Turtle Creek	41.5267	-85.1036
C	Outwash	LaPorte	On US-30 over Turf Farm Ditch	41.4058	-86.7389
D	Aeolian sand	Newton	On SR-55 over Gregory Ditch	41.0906	-87.3336
E	Outwash	Tippecanoe	US-52 bridge over Wabash River, Lafayette	40.4511	-86.8929
F	Glacial till	Clinton	310 ft southwest of INDOT office (1675 IN-28, Frankfort)	40.2777	-86.5342
G	Glacial till	Madison	On SR-32 over Indian Camp Creek	40.0842	-85.8283
H	Glacial till	Decatur	On US-421, 780 ft southeast of Lost Fork Stream	39.3064	-85.4333
I	Loess with sand	Knox	On SR-550 over Smalls Creek, 1.57 miles west of SR-67	38.7892	-87.4383
J	Lacustrine soil	Vanderburgh	On W Delaware St, 2.16 miles west of US-41	37.9840	-87.5816

state to demonstrate the effect of Indiana geology on cone penetration test results.

The raw CPT data collected from each location was post-processed to obtain profiles of cone resistance q_c, sleeve resistance f_s, and friction ratio FR ($= f_s/q_c$). The USGS and INDOT CPT rigs record data at 5 cm depth intervals, while the Purdue CPT rig records data at 2 mm depth intervals (Salgado et al., 2015). The corrected, total cone resistance q_t was calculated by taking into account the unbalanced pore water pressure acting on opposing sides of both the face and joint annulus of the cone tip (Jamiolkowski et al., 1985; Lunne et al., 1997; Robertson et al., 1986; Salgado, 2008):

$$q_t = q_c + (1-a)u_2 \qquad \text{(Eq. 2.1)}$$

where q_c = measured cone resistance, u_2 = pore water pressure measured at the shoulder position behind the cone face, and a = cone area ratio (= 0.8 for the Hogentogler CPT probe (Hogentogler & Co. Inc., 2004)). According to ASTM D5778 (ASTM, 2012), the correction of q_c to q_t is particularly important for CPTs in saturated clays, silts, and soils having considerable amount of fines where substantial pore pressures are generated during penetration; however, for CPTs in clean sands, dense to hard geomaterials, and dry soils, the correction may be ignored without significant error. It is assumed hereafter that this correction has been applied whenever it produces nonnegligible changes to q_c, and thus q_c will not be distinguished from q_t, unless otherwise stated.

A soil profile generation algorithm developed by Ganju et al. (2017) was used to generate stratigraphic profiles from the CPT data obtained at each location. The algorithm requires seven input parameters: depth, corrected cone resistance, sleeve resistance, ground surface elevation, latitude, longitude, and groundwater table depth. The algorithm was implemented for the soil behavior type (SBT) chart proposed originally by Tumay (1985) and modified subsequently by Ganju et al. (2017). The original Tumay (1985) chart was

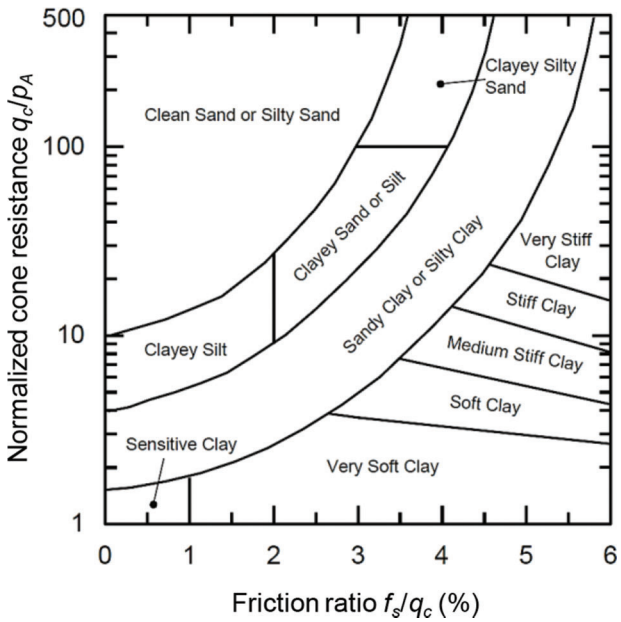

Figure 2.9 Modified Tumay (1985) SBT chart (Ganju et al., 2017; Salgado et al., 2019).

modified in order to (a) minimize ambiguities associated with soil behavior types, and (b) make a clearer distinction between soil intrinsic variables (related closely to soil composition) and soil state variables, such as relative density, stress state, and fabric. Figure 2.9 shows the modified version of the Tumay (1985) SBT chart. In general, a combination of low q_c/p_A (< 10) and high f_s/q_c values (> 4%) suggests a clayey soil, whereas a combination of high q_c/p_A (> 50) and low f_s/q_c values (< 2%) suggests a sandy soil; where p_A = reference stress (= 100 kPa or 14.5 psi).

Table 2.2 summarizes the soil behavior types associated with the modified Tumay (1985) chart. Each soil behavior type that appears in Figure 2.9 is assigned a zone number. For instance, zones 1 to 7 correspond to clays of different stiffnesses, zone 8 corresponds to

TABLE 2.2
Soil behavior types associated with the modified Tumay (1985) chart

Zone	Soil Behavior Type
1	Sensitive clay
2	Very soft clay
3	Soft clay
4	Medium stiff clay
5	Stiff clay
6	Very stiff clay
7	Sandy clay or silty clay
8	Clayey silty sand
9	Clayey sand or silt
10	Clayey silt
11	Very dense sand or silty sand
12	Dense sand or silty sand
13	Medium dense sand or silty sand
14	Loose sand or silty sand
15	Very loose sand or silty sand

sands containing fines, and zones 9 and 10 correspond to clayey sand or silt and clayey silt, respectively. Ganju et al. (2017) further divided the "clean sand or silty sand" region of the modified Tumay (1985) chart into five zones (zones 11 to 15 in Table 2.2) based on the relative density, which can be estimated from CPT data using the correlation of Salgado and Prezzi (2007).

Apart from the modified Tumay (1985) chart, a modified version of the Robertson (1990) SBT chart, which distinguishes clean sand from gravelly sand, was also used to generate the SBT profile, particularly for location E in Tippecanoe County. Figure 2.10 shows the modified Robertson (1990) SBT chart according to Ganju et al. (2017). The chart uses values of normalized cone resistance $q_{tn} = (q_t - \sigma_{v0})/\sigma'_{v0}$ and normalized friction ratio $\mathrm{FR}_n\,(\%) = [f_s/(q_t - \sigma_{v0})] \times 100\%$; where σ_{v0} and σ'_{v0} = *in situ* vertical total and effective stresses, respectively, at the depth being considered. As the values of σ_{v0} and σ'_{v0} depend on the unit weights of the soil layers at the site and the elevation of the groundwater table, the modified Robertson (1990) SBT chart can only be used after the CPT data has been post-processed.

Table 2.3 summarizes the soil behavior types associated with the modified Robertson (1990) chart. Similar to the modified Tumay (1985) chart, each soil behavior type that appears in Figure 2.10 is assigned a zone number. Ganju et al., (2017) further divided the "gravelly sand to sand" region and the "clean sand to silty sand" region of the modified Robertson (1990) chart into five zones each (zones 6 to 10 and 11 to 15 in Table 2.3) based on the relative density, which can be estimated from CPT data using the correlation of Salgado and Prezzi (2007).

A total of 23 CPT soundings were analyzed from locations A–J using the soil profile generation algorithm developed by Ganju et al. (2017). In this algorithm, firstly, an initial soil profile is generated by plotting the q_c and FR values, obtained at each depth

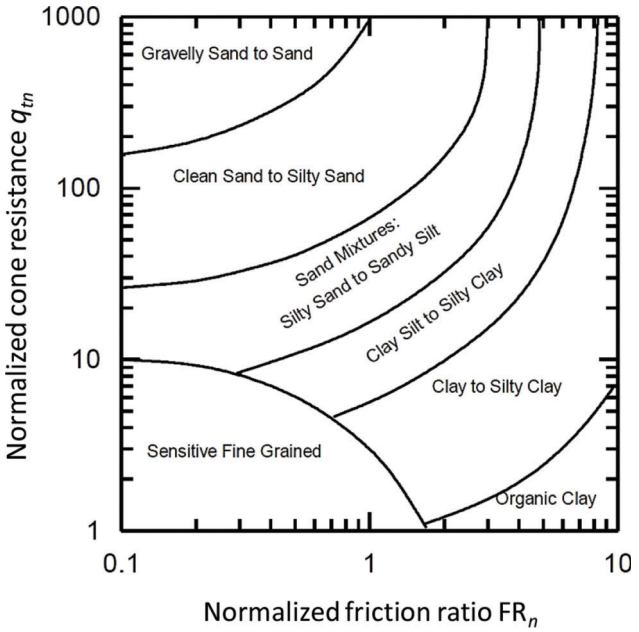

Figure 2.10 Modified Robertson (1990) SBT chart (Ganju et al., 2017; Salgado et al., 2019).

TABLE 2.3
Soil behavior types associated with the modified Robertson (1990) chart

Zone	Soil Behavior Type
1	Sensitive fine-grained
2	Organic clay
3	Clay to silty clay
4	Clay silt to silty clay
5	Sand mixtures: silty sand to sandy silt
6	Very dense gravelly sand to sand
7	Dense gravelly sand to sand
8	Medium dense gravelly sand to sand
9	Loose gravelly sand to sand
10	Very loose gravelly sand to sand
11	Very dense clean sand to silty sand
12	Dense clean sand to silty sand
13	Medium dense clean sand to silty sand
14	Loose clean sand to silty sand
15	Very loose clean sand to silty sand

during cone penetration, on the selected SBT chart. Secondly, any layer in the initial soil profile with thickness less than or equal to 15 cm (5.9 in.) (or 4.2 cone diameters) is tagged as a thin layer—a layer in which the CPT probe is unable to develop a cone resistance that is representative of that layer. Finally, the initial soil profile is reanalyzed with the objective of merging the thin layers into the adjacent thick layers to obtain the final soil profile. This is done using three sequential approaches: (1) the SBT band approach, (2) the soil group approach, and (3) the average q_c approach, all of which are described in detail by Salgado et al. (2015) and Ganju et al. (2017). The significance of this methodology is that the final

generated soil profile will not contain layers thinner than 15 cm (5.9 in.). This mitigates the creation of a significantly fragmented soil profile littered with clusters of layers that are too small to be sensed properly by the standard CPT probe.

Apart from the CPT, additional independent sampling may be performed to corroborate the soil profile at a site. However, soil behavior types obtained from SBT charts may not always fully agree with traditional soil classifications based on grain-size distribution and soil plasticity, such as the Unified Soil Classification System (USCS) (ASTM, 2017) or the American Association of State Highway and Transportation Officials (AASHTO, 1991), because of the role of soil fabric and structure (Robertson, 2016). Nonetheless, a qualitative comparison between the SBT profiles generated using the selected SBT chart and the soil profiles obtained from *in situ* boring logs can be instructive.

To complement the CPT profiles obtained at locations A–J, the corrected SPT blow count N_{60} and the ratio q_c/p_AN_{60} are plotted as a function of depth; where p_A = reference stress (= 100 kPa or 14.5 psi). The SPTs were performed using an automatic trip hammer with an energy ratio of about 80% (Salgado, 2008). As both cone resistance and SPT blow count are essentially penetration resistances, they are closely related. Hence, plots of q_c/p_AN_{60} versus depth may be useful in case a CPT-based design method needs to be used when only SPT blow counts are available for the site. It should be noted that not all the locations marked in Figure 2.8 have SPT borings completed along with CPT soundings. Also, it is important to note that the SPT borings were not carried out at the exact locations of the CPT soundings but were performed within the same project site. Therefore, the following q_c/p_AN_{60} plots for each site should be interpreted with caution.

2.2.1 Dune/Aeolian Sands

Figure 2.11 and Figure 2.12 show the CPT profiles (q_c, f_s, FR), the SBT profile generated using the modified Tumay (1985) chart, the SPT N_{60} and q_c/p_AN_{60} profiles, and the *in situ* layer information (with AASHTO group numbers) reported in the boring logs for location A in Lake County and location D in Newton County, respectively. Location A is in the dune sand region of northern Indiana, while location D is slightly further to the south of location A. The stratigraphic profile obtained from the SPT boring log at location A consists of 8 m (26 ft) of medium dense sandy loam followed by 7 m (23 ft) of very loose-to-medium dense sand and 3 m (10 ft) of dense sandy loam. On the other hand, the stratigraphic profile from the SPT boring log at location D consists of 1.5 m (5 ft) of very loose-to-loose sand followed by 12.5 m (41 ft) of medium dense sand.

The numbers mentioned on the SBT profiles, generated using the modified Tumay (1985) chart, correspond to the soil zones listed in Table 2.2. The SBT profiles generated using the modified Tumay (1985) chart for both locations A and D agree qualitatively with the soil profiles obtained from the corresponding SPT boring logs. The soil profiles obtained from the boring logs are based on laboratory testing of soil samples collected at depth intervals of 1.5 m (5 ft), whereas the SBT profiles generated using the modified Tumay (1985) chart are based on nearly continuous CPT measurements at 5 cm (2 in.) depth intervals. Thus, the SBT profiles contain more soil layers than the soil profiles obtained from the boring logs because some of these layers may lie between consecutive SPT sampling intervals. The q_c/p_AN_{60} values for locations A and D range from about 3 to 8, which is typical for sandy soils based on their mean particle size D_{50} (Robertson et al., 1983).

2.2.2 Outwash

Figure 2.13 shows the CPT profiles (q_c, f_s, FR) and the SBT profile generated using the modified Tumay (1985) chart for location C in LaPorte County, while Figure 2.14 shows the CPT profiles (q_c, f_s, FR), the SBT profile generated using the modified Tumay (1985) chart, the SPT N_{60} and q_c/p_AN_{60} profiles, and the *in situ* layer information (with AASHTO group numbers) reported in the boring log for location E in Tippecanoe County. Location C lies in the outwash region of northern Indiana, while location E is on the bank of the Wabash River near Purdue University. Outwash is a mixture of sand, gravel, cobbles, and boulders that are transported and deposited by glacial meltwater; it may also include some modern river alluvium. The SBT profile at location C consists of multiple layers of loose-to-very dense sand or silty sand (Figure 2.13).

The soil profile reported in the SPT boring log for location E in Tippecanoe County consists of sandy clay loam and loose-to-medium dense sandy gravel in the upper half of the profile and medium dense-to-very dense sand with gravel, cobbles, and boulders in the lower half of the profile (Figure 2.14b). The N_{60} values range from about 2 to 43, and the q_c/p_AN_{60} values range from about 3 to as high as 16 due to the presence of gravel, cobbles, and boulders in the soil profile. The modified Tumay (1985) chart includes soil behavior types ranging from clays to clay-silt-sand mixtures to sands of varying states; however, the chart does not clearly distinguish sands from sand-gravel mixtures and gravelly sands. Therefore, a modified version of the Robertson (1990) SBT chart, which distinguishes clean sand from gravelly sand, was also used to generate the SBT profile for location E.

Figure 2.15 compares the SBT profile generated using the modified Robertson (1990) chart with that obtained using the modified Tumay (1985) chart for location E in Tippecanoe County. In order to classify the coarse-grained soil layers at the site based on their relative density (using the Salgado and Prezzi (2007) correlation), the saturated unit weight γ_{sat}, the critical-state friction angle ϕ_c, and the coefficient of lateral earth pressure at-rest K_0 of the coarse-grained layers

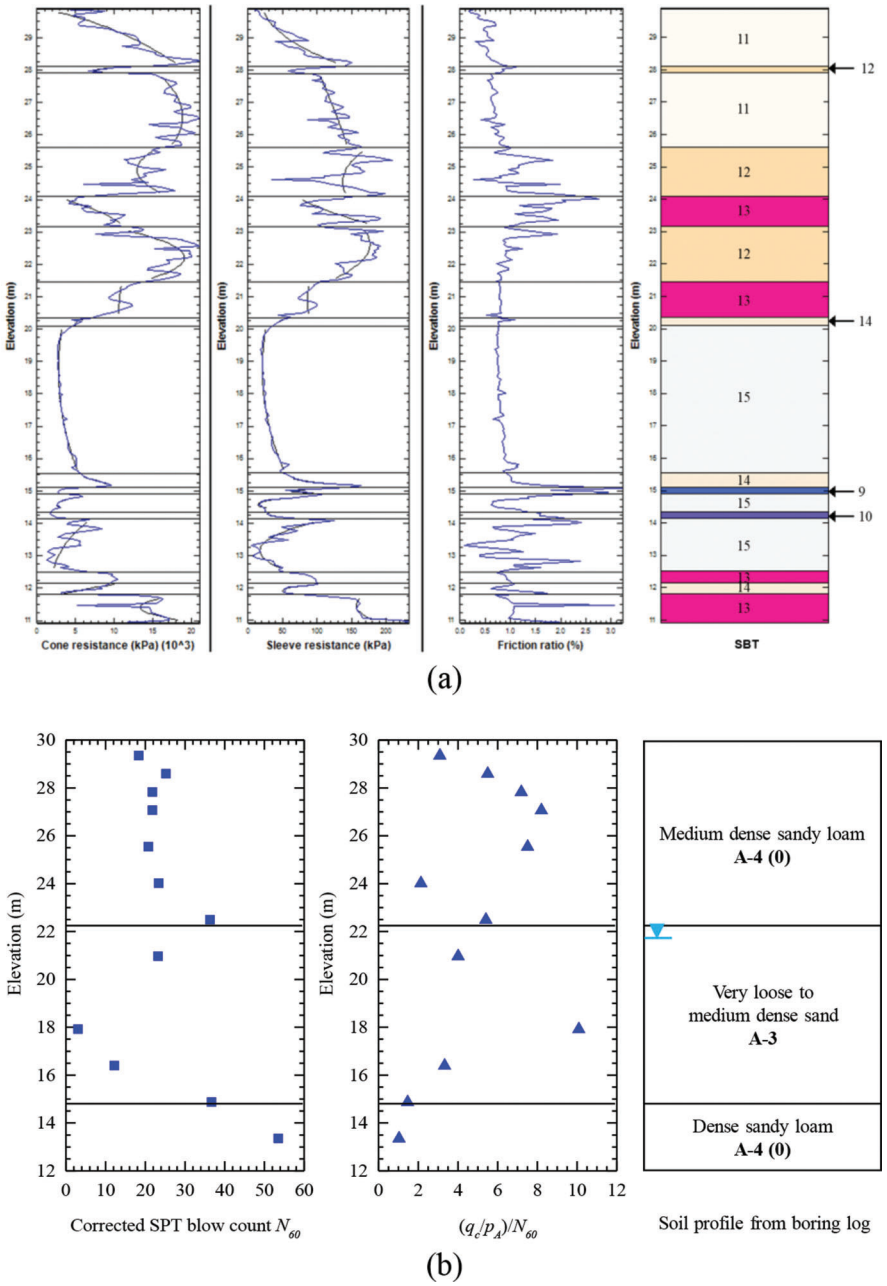

Figure 2.11 *In situ* test profiles for location A in Lake County: (a) CPT-1 profile (q_c, f_s, FR) and SBT interpreted from modified Tumay (1985) chart, and (b) N_{60} profile, $(q_c/p_A)/N_{60}$ profile, and soil profile from SPT boring TB-2 (Data source: A. Tilahun, J. Paauwe, & N. Z. Siddiki, personal communication, December 20, 2017).

were taken as 22.5 kN/m^3 (143.2 lb/ft^3), 32°, and 0.45, respectively. The SBT profile obtained using the modified Robertson (1990) chart shows layers of very dense and medium dense gravelly sand to sand, indicated by zone numbers 6 and 8, respectively (Table 2.3), between elevations ranging from 149–153 m and 137–143 m and a layer of medium dense gravelly sand to sand at the 128–131 m elevation. In contrast, the SBT profile obtained using the modified Tumay (1985) chart shows layers of very dense sand or silty sand (indicated by zone number 11) at these elevations and does not capture the presence of gravelly material in the profile. The mean particle size D_{50} and gravel content at the site are in the range of 0.4–4.5 mm (0.016–0.18 in.) and 5%–50%, respectively (Han et al., 2019b, 2020). Hence, for sites with high gravel content, the modified Robertson (1990) chart is a better option for generating SBT profiles from CPT data than the modified Tumay (1985) chart. The delineation of gravelly material in the profile using a CPT-based SBT chart has implications in foundation design because the constitutive response of a sand-gravel mixture is different from that of clean sand, for instance, when subjected to shearing.

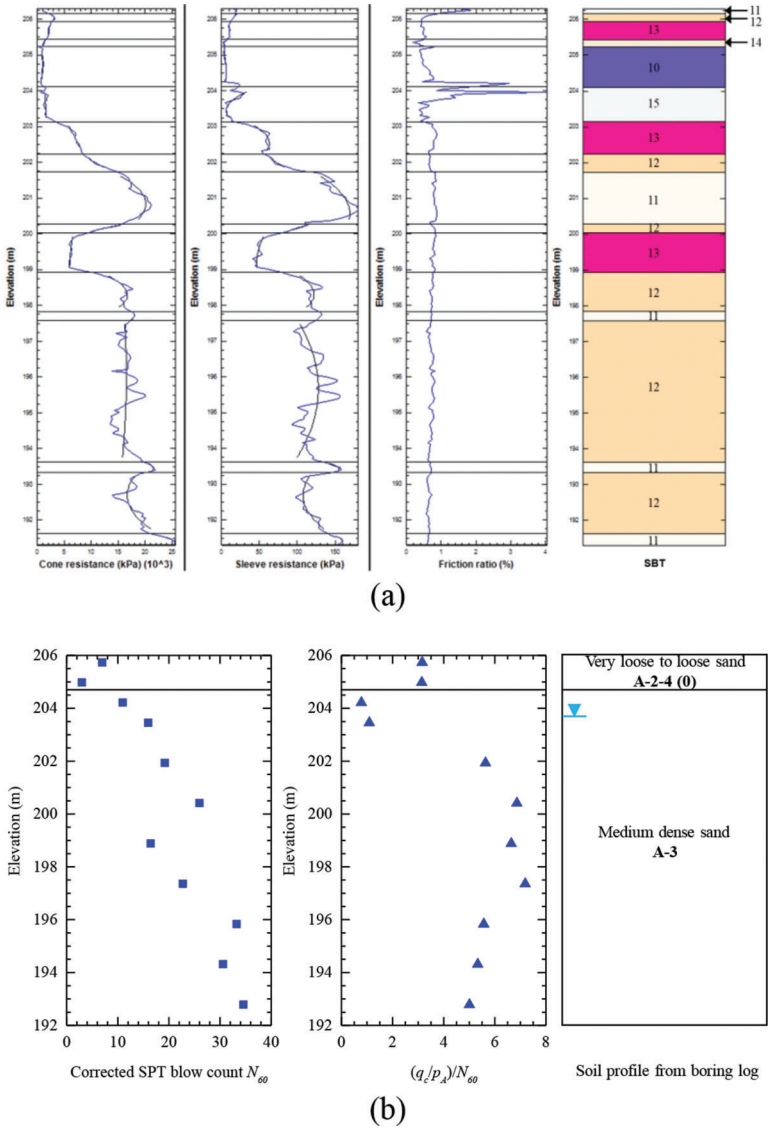

Figure 2.12 *In situ* test profiles for location D in Newton County: (a) CPT-2 profile (q_c, f_s, FR) and SBT interpreted from modified Tumay (1985) chart, and (b) N_{60} profile, $(q_c/p_A)/N_{60}$ profile, and soil profile from SPT boring TB-1 (Data source: A. Tilahun, J. Paauwe, & N. Z. Siddiki, personal communication, December 20, 2017).

2.2.3 Glacial Till

Figures 2.16, 2.17, 2.18, and 2.19 show the CPT profiles (q_c, f_s, FR), the SBT profiles generated using the modified Tumay (1985) chart, the SPT N_{60} and q_c/p_AN_{60} profiles, and the *in situ* layer information (with USCS/AASHTO group numbers) reported in the boring logs for locations B, F, G, and H in Steuben, Clinton, Madison, and Decatur counties, respectively. These locations are characterized by glacial till deposits, as shown in Figure 2.8. Location B is in northeastern Indiana where the till is in a hummocky moraine form, locations F and G are in central Indiana where the till is mostly in the form of flat plains, and location H is in southeastern Indiana where the till is capped by thin wind-blown silt. The stratigraphic profiles at these locations consist of layers of sandy silty clay, silty sand, and loam with different percentages of sand, silt, and clay. The q_c/p_AN_{60} values for locations F, G, and H range from 0.5–2.0, 0.5–1.0, and 1.0–3.5, respectively. These ranges are smaller than those reported for the dune/aeolian sand and outwash regions in Sections 2.2.1 and 2.2.2, respectively, due to the presence of smaller particle sizes associated with the soil types illustrated in Figure 2.16 to Figure 2.19.

2.2.4 Loess with Sand

Figure 2.20 shows the CPT profiles (q_c, f_s, FR), the SBT profile generated using the modified Tumay (1985) chart, the SPT N_{60} and q_c/p_AN_{60} profiles, and the *in situ* layer information (with AASHTO group numbers) obtained from the SPT boring log for location I in Knox County. This location is in southwestern Indiana,

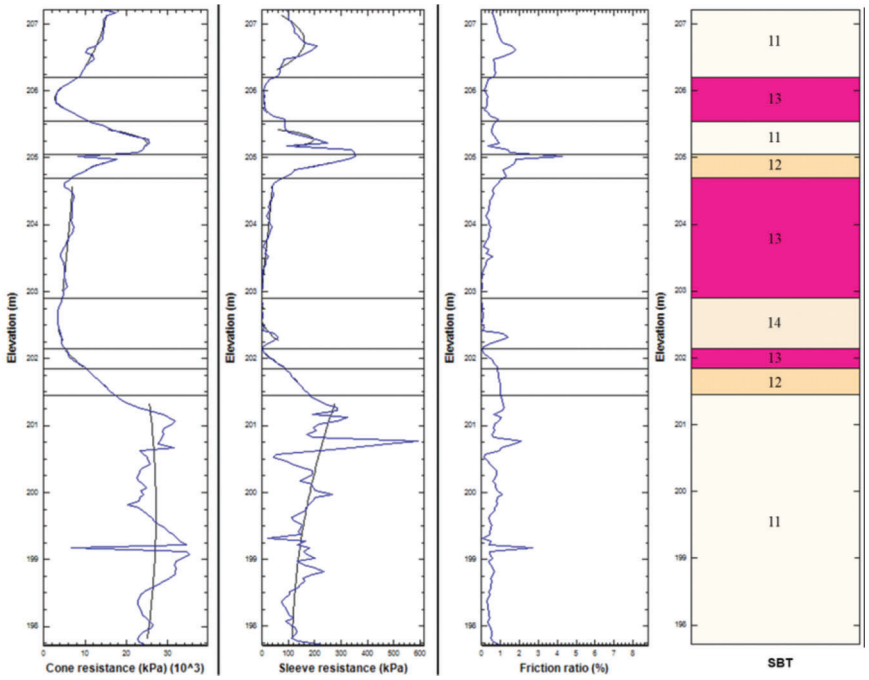

Figure 2.13 CPT-2 profile (q_c, f_s, FR) and SBT interpreted from modified Tumay (1985) chart for location C in LaPorte County (Data source: A. Tilahun, J. Paauwe, & N. Z. Siddiki, personal communication, December 20, 2017).

which is characterized by wind-blown silt deposits. The stratigraphic profile obtained from the SPT boring log consists of 1 m (3 ft) of very loose sand followed by 3 m (10 ft) of very loose-to-loose loam, 2 m (6.5 ft) of very loose-to-medium dense sandy loam, 8 m (26 ft) of soft-to-hard silty loam, and finally unweathered-to-highly-weathered sandstone at a depth of 16.3–21.0 m (53–69 ft) below the ground surface. These layers are also captured by the CPT-based SBT profile via zone numbers 6–10 (Table 2.2). The N_{60} values at the site range from about 5 to as high as 80, while the $q_c/p_A N_{60}$ values range from 1.0 to 4.5.

2.2.5 Lacustrine Soil

Figure 2.21 shows the CPT profiles (q_c, f_s, FR) and the SBT profile generated using the modified Tumay (1985) chart for location J in Vanderburgh County. This location is in southern Indiana, near the border with Kentucky, and is characterized by lacustrine soil. Lacustrine soils form under relatively quiet conditions at the bottom of lakes and typically consist of silt to clay-sized particles. The SBT profile generated using the modified Tumay (1985) chart consists of 4 m (13 ft) of soft-to-very stiff clay and clayey silt underlain by 8 m (26 ft) of medium dense silty sand and 7 m (23 ft) of sandy clay or silty clay.

2.3 Correlation Between CPT Cone Resistance and SPT Blow Count

Figure 2.22 shows the correlation between the CPT cone resistance q_c and the corrected SPT blow count N_{60} as a function of mean particle size D_{50}. The chart includes data reported by Robertson et al. (1983) and data obtained from 15 sites in Indiana (2 sites each in Hamilton, Tippecanoe, Clinton, and Greene counties, and 1 site each in Jasper, Lake, Newton, Knox, Starke, Dubois, and Carroll counties). Starke, Newton, Jasper, and Lake counties are located in northern Indiana; Hamilton, Tippecanoe, Carroll, and Clinton counties are in central Indiana; and Greene, Knox, and Dubois counties are in southern Indiana. The following expression approximates the trend of the 98 data points plotted in Figure 2.22:

$$\frac{q_c}{p_A N_{60}} = 6.95\left(\frac{D_{50}}{D_{\text{ref}}}\right)^{0.25} - 0.18 \text{ for } 0.001 \le \frac{D_{50}}{D_{\text{ref}}} \le 10 \quad \text{(Eq. 2.2)}$$

where p_A = reference stress (= 100 kPa or 14.5 psi), D_{50}= mean particle size, and D_{ref} = reference particle size (= 1 mm or 0.0394 in.). The coefficient of determination R^2 and the standard error (SE) of the regression are 0.89 and 0.77, respectively. Equation 2.2 may be used to obtain an estimate of q_c for use in a CPT-based foundation design method when only SPT blow counts are available for a site. However, as with any correlation involving the SPT blow count, Eq. 2.2 should be used with caution because of the potential error introduced by the transformation from the SPT blow count (a dynamic resistance) to the CPT cone resistance (a quasi-static resistance). The $q_c/p_A N_{60}$ ratio estimated using Eq. 2.2 may be decreased by 20%–40%, if needed, to obtain a conservative value of cone resistance. Equation 2.2 can be further improved as additional SPT blow count, cone resistance and D_{50} data become available in Indiana.

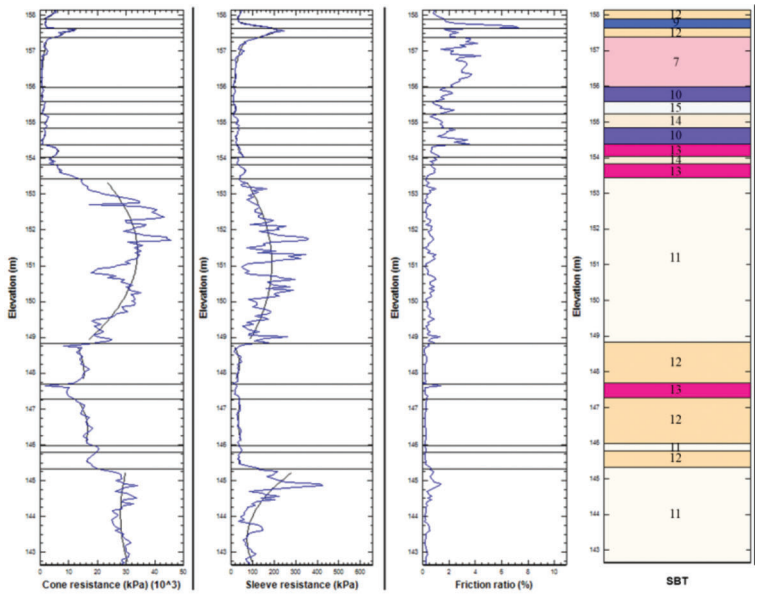

Figure 2.14 *In situ* test profiles for location E in Tippecanoe County: (a) CPT-3 profile (q_c, f_s, FR) and SBT interpreted from modified Tumay (1985) chart, and (b) N_{60} profile, $(q_c/p_A)/N_{60}$ profile and soil profile from SPT boring Pier-7 (Data source: A. Tilahun, J. Paauwe, & N. Z. Siddiki, personal communication, December 20, 2017).

The corrected SPT blow count N_{60} is expressed as (Salgado, 2008):

$$N_{60} = C_h C_r C_s C_d N_{\text{SPT}} \qquad \text{(Eq. 2.3)}$$

where N_{SPT} = measured SPT blow count, C_h = hammer correction, C_r = rod length correction, C_s = sampler correction, and C_d = borehole diameter correction:

$$C_h = \begin{cases} 0.75 \text{ for donut hammer (ER} = 45\%) \\ 1.00 \text{ for safety hammer(ER} = 60\%) \\ 1.20 \text{ for pin weight hammer (ER} = 72\%) \\ 1.33 \text{ for automatic trip hammer (ER} = 80\%) \end{cases} \qquad \text{(Eq. 2.4)}$$

$$C_r = \begin{cases} 0.75 \text{ if rod length} < 4 \text{ m (13 ft)} \\ 0.85 \text{ if 4 m (13 ft)} \le \text{rod length} < 6 \text{ m (20 ft)} \\ 0.95 \text{ if 6 m (20 ft)} \le \text{rod length} < 10 \text{ m (33ft)} \\ 1.00 \text{ if rod length} \ge 10 \text{ m (33 ft)} \end{cases} \qquad \text{(Eq. 2.5)}$$

$$C_s = \begin{cases} 1.0 \text{ for liner sampler with liner in place} \\ 1.2 \text{ for liner sampler without the liner} \end{cases} \qquad \text{(Eq. 2.6)}$$

$$C_d = \begin{cases} 1.00 \text{ for } B = 65 - 115 \text{ mm (2.5} - 4.5 \text{ in.)} \\ 1.05 \text{ for } B = 150 \text{ mm (6.0 in.)} \\ 1.15 \text{ for } B = 200 \text{ mm (8.0 in.)} \end{cases} \qquad \text{(Eq. 2.7)}$$

where ER = energy ratio, and B = borehole diameter.

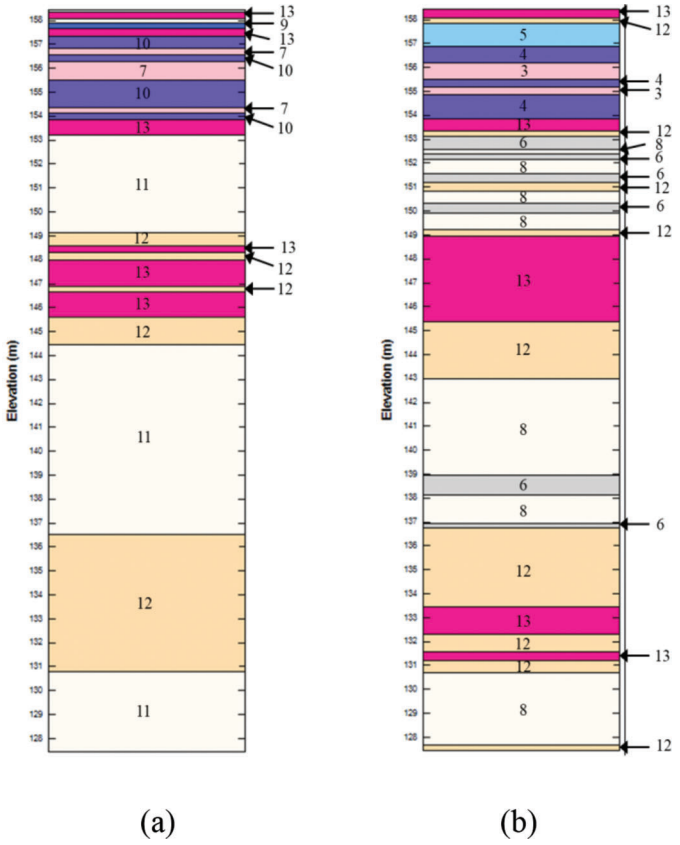

Figure 2.15 Comparison of SBT profiles obtained from sounding CPT-5 at location E in Tippecanoe County using: (a) modified Tumay (1985) chart (zone numbers listed in Table 2.2), and (b) modified Robertson (1990) chart (zone numbers listed in Table 2.3).

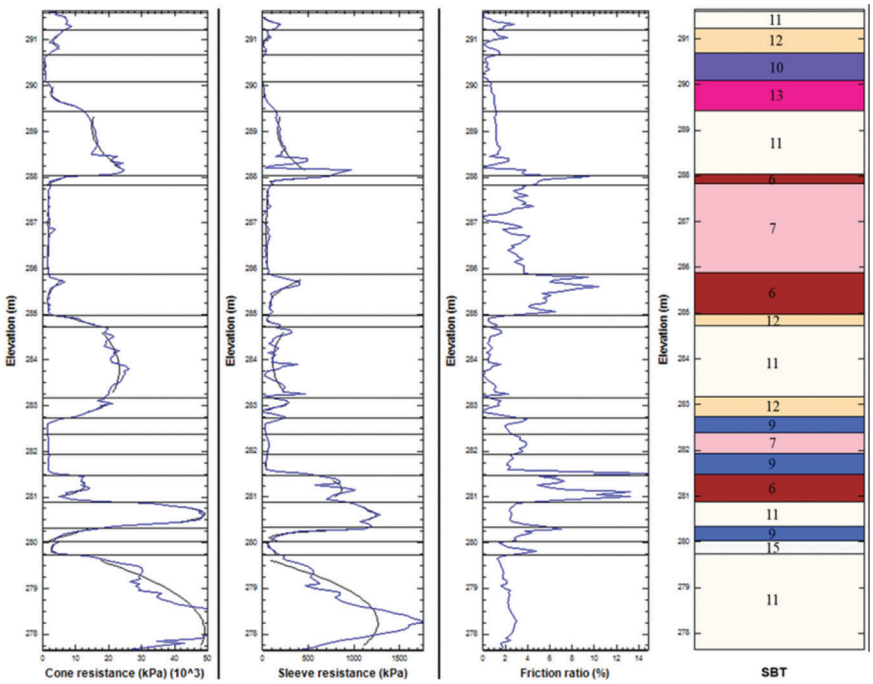

Figure 2.16 CPT-4 profile (q_c, f_s, FR) and SBT interpreted from modified Tumay (1985) chart for location B in Steuben County (Data source: A. Tilahun, J. Paauwe, & N. Z. Siddiki, personal communication, December 20, 2017).

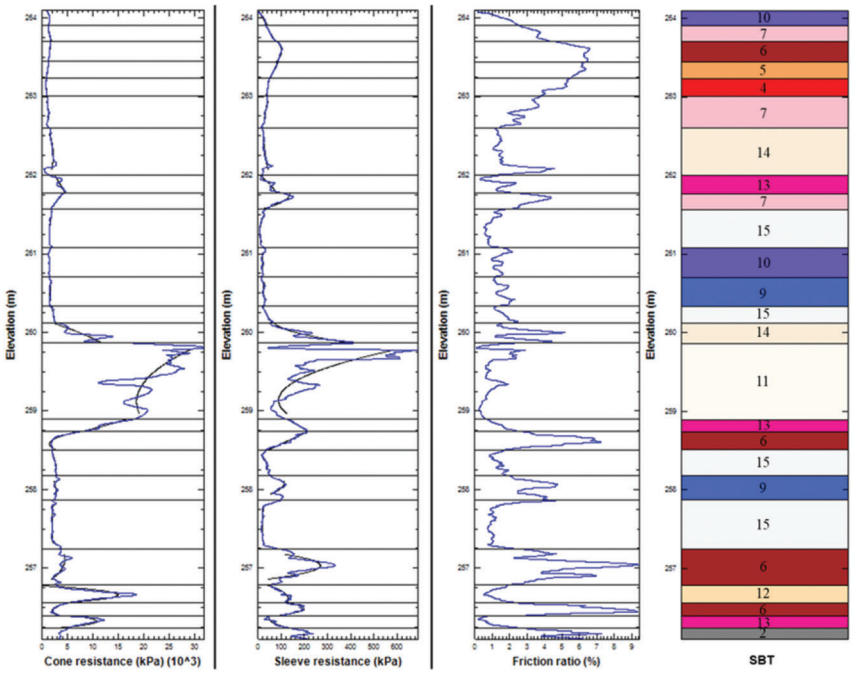

(a)

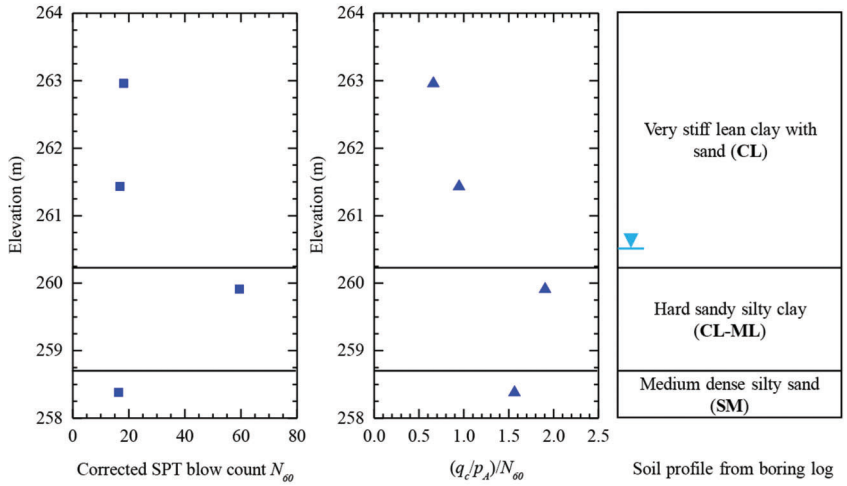

(b)

Figure 2.17 *In situ* test profiles for location F in Clinton County: (a) CPT-7 profile (q_c, f_s, FR) and SBT interpreted from modified Tumay (1985) chart, and (b) N_{60} profile, $(q_c/p_A)/N_{60}$ profile, and soil profile from boring SPT-8.

2.4 CPT-Based Site Variability Assessment

Soil properties used in geotechnical design are often estimated from a limited number of *in situ* or laboratory tests (due to project budget and time constraints) and are thus subject to uncertainty, raising the question as to how accurately the soil properties derived from these tests are representative of the entire site (Phoon & Kulhawy, 1999a,b). Although this uncertainty cannot be eliminated, it can be quantified by analyzing the variability within individual CPT soundings and of the collection of soundings performed at a site (Cao & Wang, 2013; Salgado et al., 2015; Xiao et al., 2018). If reasonably quantified, this uncertainty may be used to select appropriate resistance factors for use in load and resistance factor design (LRFD) of foundations and retaining structures (Foye, 2005; Foye et al., 2006a,b, 2009; Kim & Salgado, 2012a,b; Salgado et al., 2011; Salgado & Kim, 2014). For sites with high variability, lower resistance factors could be used to increase the

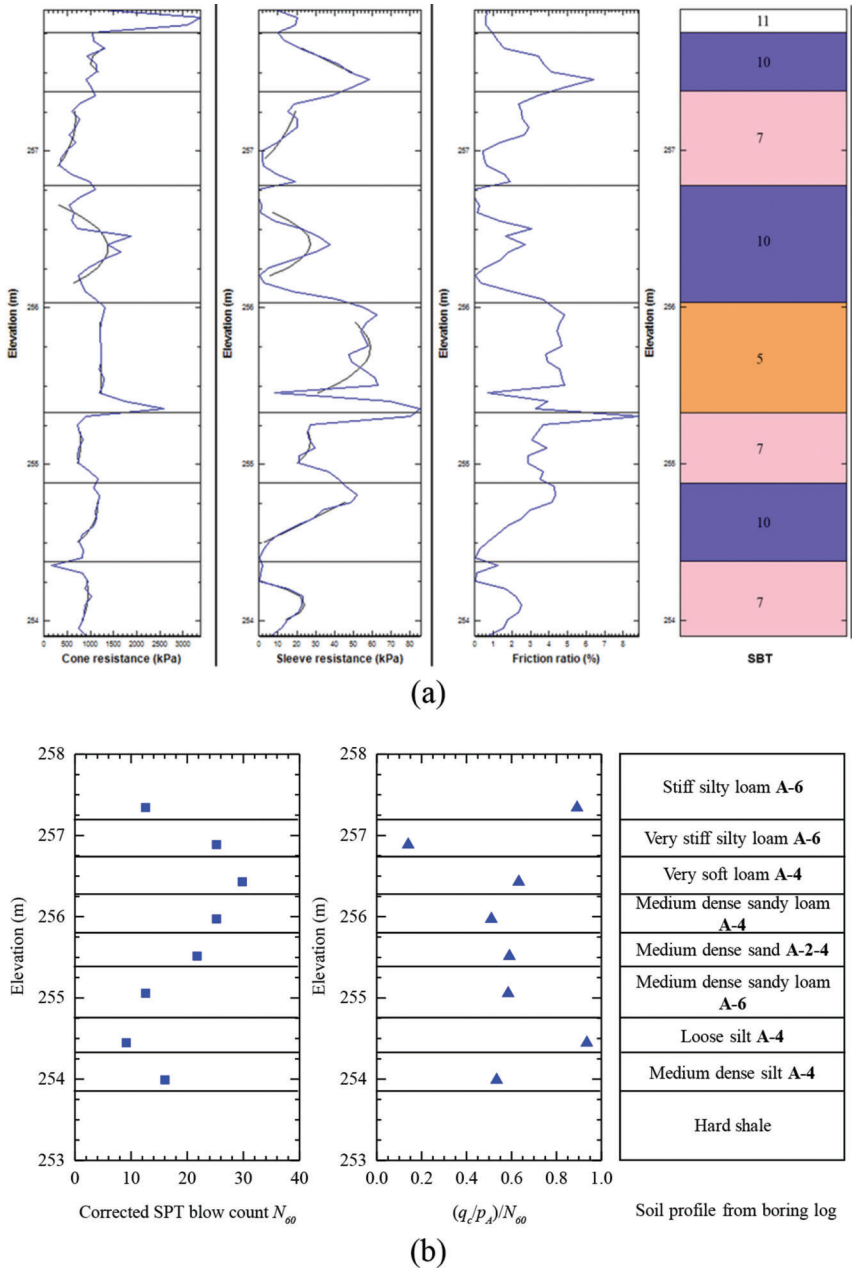

Figure 2.18 *In situ* test profiles for location G in Madison County: (a) CPT RB-2 profile (q_c, f_s, FR) and SBT interpreted from modified Tumay (1985) chart, and (b) N_{60} profile, $(q_c/p_A)/N_{60}$ profile and soil profile from SPT boring TB-2 (Data source: A. Tilahun, J. Paauwe, & N. Z. Siddiki, personal communication, December 20, 2017).

reliability of the foundation design, whereas for sites with low variability, higher resistance factors could be used to optimize the construction cost. Based on the coefficient of variation (COV) of the average strength parameter (e.g., SPT blow count N_{SPT}) of each soil layer at a site, Paikowsky (2004) suggested that site variability can be classified as low (COV $<$ 25%), medium (25% $\leq$ COV $\leq$ 40%), or high (COV $>$ 40%). However, the volume of data available for statistical analysis using the SPT is smaller in comparison to the CPT, and thus it is better to use a CPT dataset for site variability assessment.

Salgado et al. (2019) developed the following four-step procedure for CPT-based site variability assessment.

1. Generate the SBT profile from the CPT data using an SBT chart.
2. Quantify vertical variability via the vertical variability index (VVI), which reflects the variability in q_c, f_s, and soil layering for each CPT sounding.
3. Quantify horizontal variability via the horizontal variability index (HVI), which depends on the cross-correlation between cone resistance logs, cone resistance trend differences, and the spacing between CPT soundings.

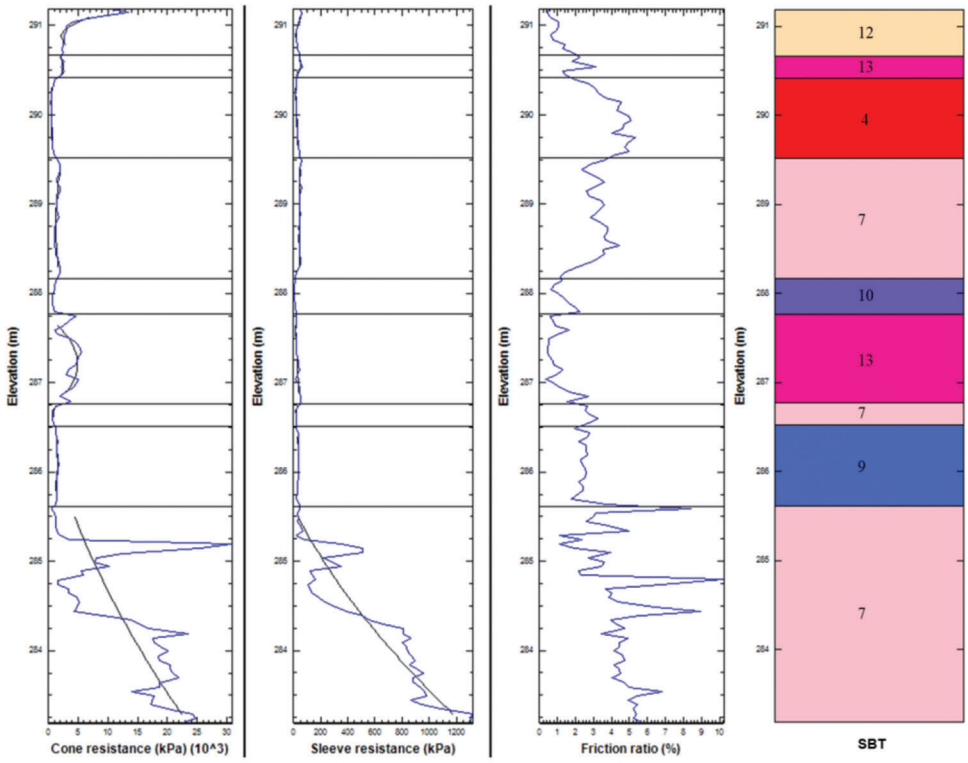

Figure 2.19 *In situ* test profiles for location H in Decatur County: (a) CPT-1 profile (q_c, f_s, FR) and SBT interpreted from modified Tumay (1985) chart, and (b) N_{60} profile, $(q_c/p_A)/N_{60}$ profile and soil profile from SPT boring TB-1 (Data source: A. Tilahun, J. Paauwe, & N. Z. Siddiki, personal communication, December 20, 2017).

4. Combine both vertical and horizontal variability into an overall site variability rating (SVR) system.

Figure 2.23 shows how to categorize a site as being of low (L), medium (M), or high (H) variability in the vertical and horizontal directions based on whether the site VVI and HVI values fall in the 0%–33%, 33%–66%, or 66%–100% range, respectively. Salgado et al. (2015, 2019) established a site variability rating, defined in terms of a string variable with two characters, each of

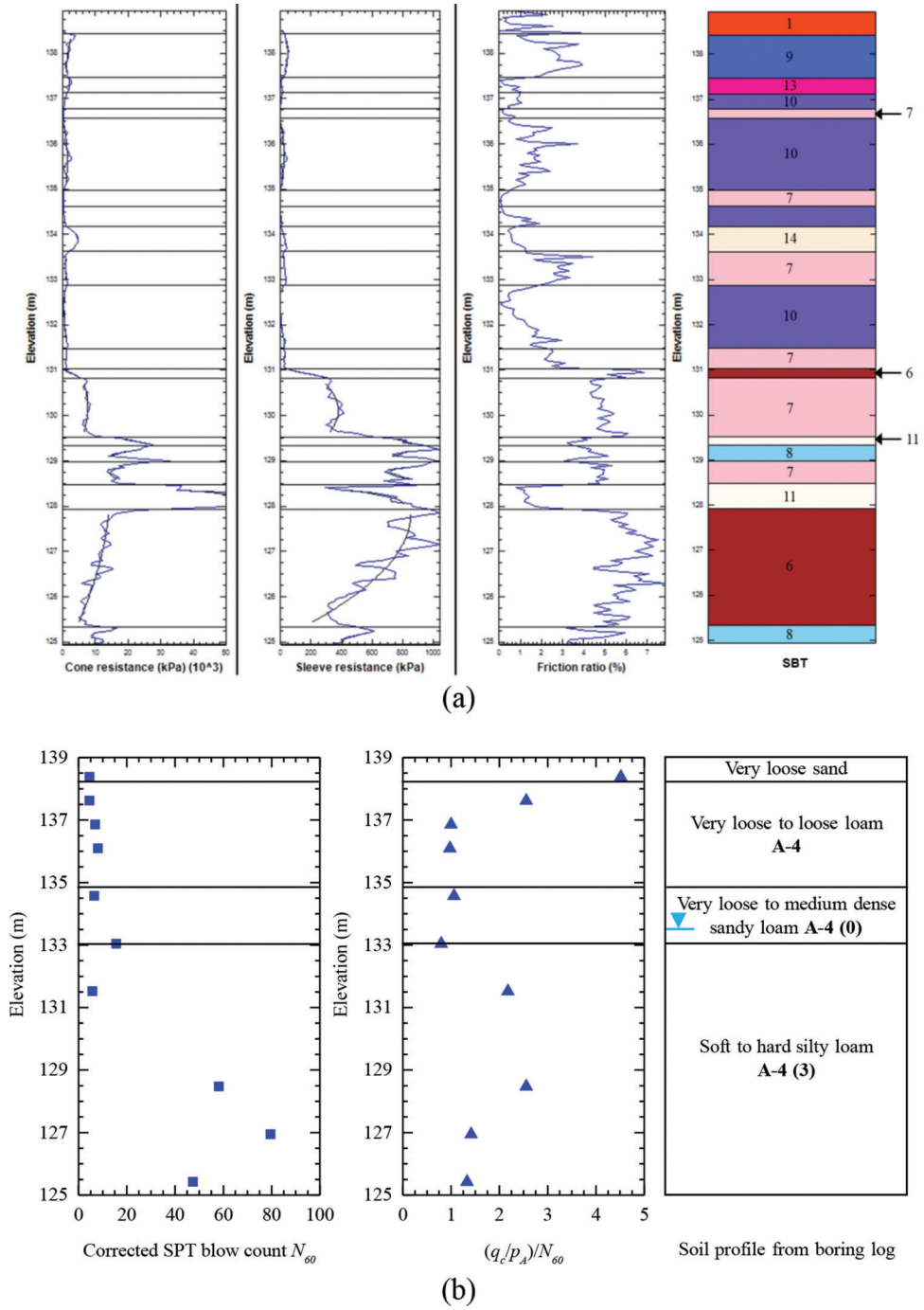

Figure 2.20 *In situ* test profiles for location I in Knox County: (a) CPT-1 profile (q_c, f_s, FR) and SBT interpreted from modified Tumay (1985) chart, and (b) N_{60} profile, $(q_c/p_A)/N_{60}$ profile, and soil profile from SPT boring TB-2 (Data source: A. Tilahun, J. Paauwe, & N. Z. Siddiki, personal communication, December 20, 2017).

which may take the values, L, M, or H, as shown in Figure 2.23. The first letter corresponds to the site VVI, while the second letter corresponds to the site HVI. For instance, if the site VVI and HVI values are 47% and 31%, respectively, the site variability rating is ML, which stands for medium vertical variability and low horizontal variability.

Table 2.4 summarizes the computed vertical and horizontal variability indices for sites in Indiana using the CPT-based site variability assessment algorithm developed by Salgado et al. (2019). The sampling interval for each CPT sounding was at most 5 cm (2 in.), and the sounding depths were in the range of 3–20 m (10–65 ft). Sites A, C, and D have low site VVI values because their SBT profiles consist predominantly of medium dense-to-very dense sands of similar behavior. In contrast, the other sites (B and E–J) have medium-to-high site VVI values because their SBT

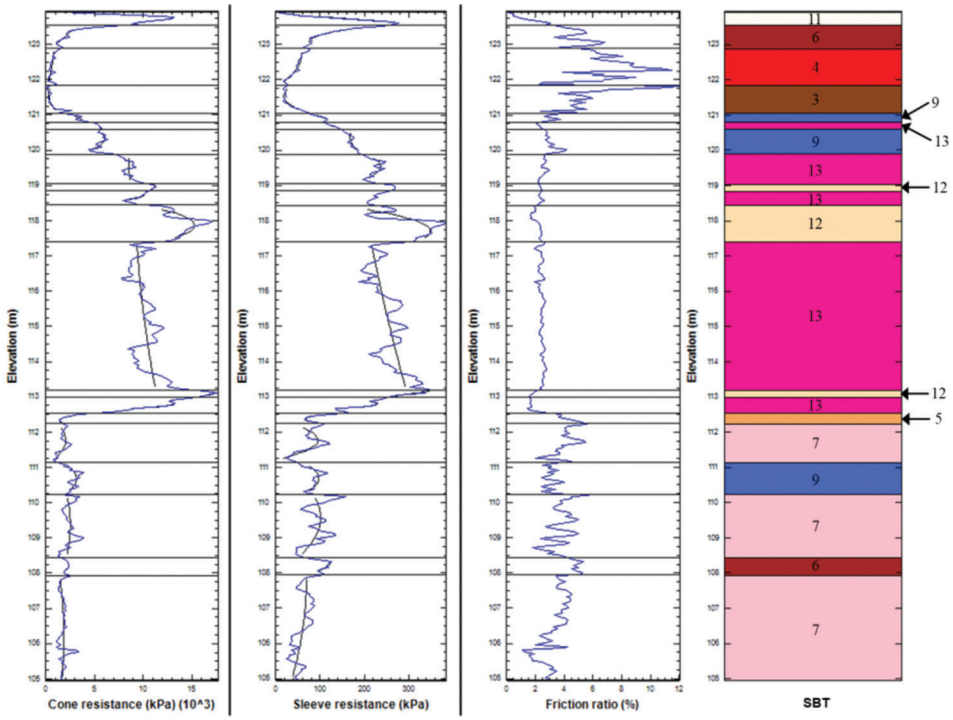

Figure 2.21 CPT-28 profile (q_c, f_s, FR) and SBT interpreted from modified Tumay (1985) chart for location J in Vanderburgh County (Data source: USGS, n.d.).

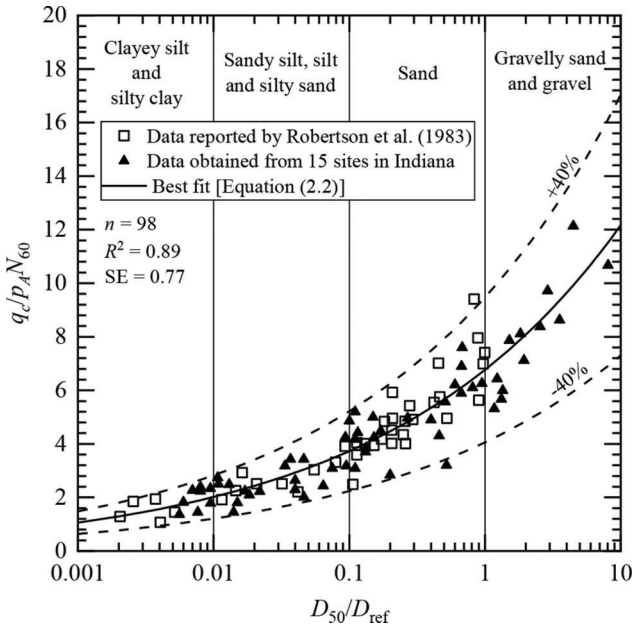

Figure 2.22 Correlation between CPT cone resistance and SPT blow count.

profiles consist of sandy, silty, and clayey soils with relatively equal representation; layers of gravelly sand were also observed for site E in Tippecanoe County. Sites B and G in the glacial till areas of Steuben and Madison counties, respectively, have HVI values of 100% due to the presence of soil layers with highly variable q_c values within the depth of interest between soundings. The CPT soundings at site G in Madison County were performed only up to a depth of 3 m (10 ft) because the project involved the replacement of an existing structure and widening of the pavement. Since the HVI value depends on the sounding depth analyzed, the volume of CPT data obtained from the shallow, closely-spaced soundings at site G in Madison County may have been insufficient to render an HVI value that is representative of the site—this may have been another reason for the very high HVI value of 100% obtained for this site. Based on the procedure outlined previously, each site was assigned a qualitative site variability rating (SVR), such as LH for low vertical and high horizontal variability (e.g., site C) and MH for medium vertical and high horizontal variability (e.g., sites B, E to G, and J), as shown in Figure 2.24.

2.5 Optimal Spacing Between CPT Soundings

The cost of a CPT-based geotechnical site investigation is directly proportional to the number of CPT soundings performed, which in turn depends on site geology and variability. The cost of a CPT-based site investigation could be reduced by optimizing the spacing between CPT soundings based on the site variability determined from the soundings already performed at the site. Figure 2.25 shows two CPT soundings, X and Y, that have already been performed at a site; the center-to-center spacing between them is s_{xy}.

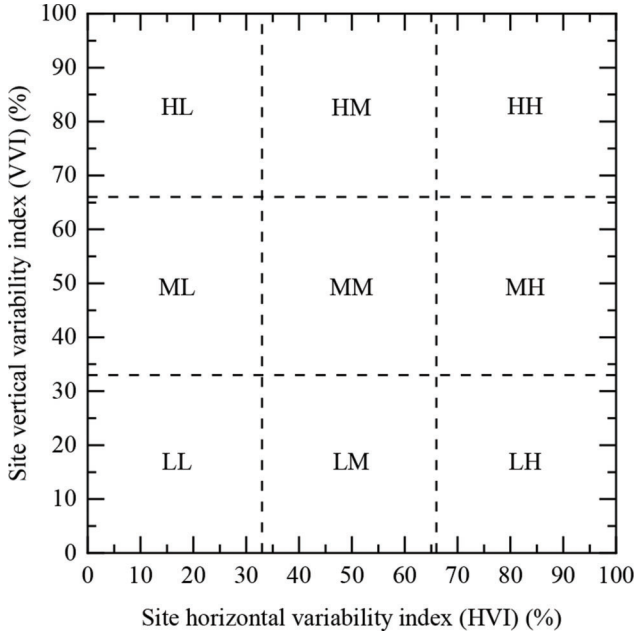

Figure 2.23 Site variability rating chart (modified from Salgado et al., 2015).

The optimal spacing $(s_{yz})_{opt}$ between CPT sounding Y and the next sounding Z can be calculated by following these steps (Ganju et al., 2019; Salgado et al., 2015, 2019):

Step 1: Set the analysis (segment) length L as the minimum of the sounding depths of CPT soundings X and Y.

Step 2: Determine the number N of cone resistance data points contained within the segment length L.

Step 3: Calculate the mean cone resistances $\bar{x}$ and $\bar{y}$ of CPT soundings X and Y, respectively, for the segment length considered.

Step 4: Calculate the standard deviations σ_x and σ_y of the q_c values of CPT soundings X and Y, respectively, using:

$$\sigma_x = \sqrt{\frac{1}{N-1}\sum_{i=1}^{N}(x_i - \bar{x})^2} \qquad \text{(Eq. 2.8)}$$

$$\sigma_y = \sqrt{\frac{1}{N-1}\sum_{i=1}^{N}(y_i - \bar{y})^2} \qquad \text{(Eq. 2.9)}$$

where x_i and y_i = q_c values of the i^{th} data point obtained from CPT soundings X and Y, respectively. The standard deviation of a sample dataset can also be calculated using the STDEV function in Microsoft Excel.

Step 5: Estimate the cross-covariance C_{xy} and the cross-correlation coefficient ρ_{xy} between CPT soundings X and Y using:

$$C_{xy} = \frac{1}{N}\sum_{i=1}^{N}(x_i - \bar{x})(y_i - \bar{y}) \qquad \text{(Eq. 2.10)}$$

$$\rho_{xy} = \frac{C_{xy}}{\sigma_x \sigma_y} \qquad \text{(Eq. 2.11)}$$

The cross-covariance and cross-correlation coefficient of a sample dataset can also be calculated using the functions COVARIANCE.S and CORREL, respectively, in Microsoft Excel. The cross-correlation coefficient ρ_{xy} takes values in the –1 to +1 range. A high cross-correlation coefficient and small q_c trend difference of a CPT pair indicates high correlation and similarity between the two CPTs, and thus low variability in the horizontal direction for the site.

Step 6: Calculate the average q_c difference $|\Delta q_{c,avg}|$ between CPT soundings X and Y using:

$$|\Delta q_{c,avg}| = \frac{\sum_{i=1}^{N}|x_i - y_i|}{N} \qquad \text{(Eq. 2.12)}$$

where x_i and y_i = q_c values of the i^{th} data point obtained from CPT soundings X and Y, respectively, and N = number of q_c data points contained within the segment length L.

Step 7: Estimate the maximum credible difference $|\Delta q_{c,avg}|_{max}$ between q_c trends for the segment length considered using:

$$\frac{|\Delta q_{c,avg}|_{max}}{p_A} = 23.86\left(\frac{L}{L_R}\right)^{0.46} - 4.30 \quad \text{for } 1 \le \frac{L}{L_R} \le 30 \qquad \text{(Eq. 2.13)}$$

where L = analysis (segment) length, L_R = reference length (= 1 m or 3.28 ft), and p_A = reference stress (= 100 kPa or 14.5 psi). The maximum credible difference is determined by considering two idealized soil profiles, one with a very soft clay layer throughout, and the other with sand having 85% relative density throughout (Salgado et al., 2019).

Step 8: Calculate the values of functions f_0, f_1, and f_2 using:

$$f_0 = \min\left[\frac{|\Delta q_{c,avg}|}{|\Delta q_{c,avg}|_{max}}; 1\right] \qquad \text{(Eq. 2.14)}$$

$$f_1 = \frac{\rho_{xy} + 1}{2} \qquad \text{(Eq. 2.15)}$$

$$f_2 = 1 - \exp\left(-0.25\frac{s_{xy}}{L_R}\right) \qquad \text{(Eq. 2.16)}$$

where s_{xy} = spacing between CPT soundings X and Y, and L_R = reference length (= 1 m or 3.28 ft).

Step 9: Estimate the horizontal variability index (HVI) for CPT soundings X and Y using:

TABLE 2.4
Vertical variability index, horizontal variability index, and site variability rating for the sites analyzed

Site	Soil Type	County	Number of Soundings	Sounding Depth Analyzed (m)	Sounding ID	VVI (%)	Site VVI (%)	Site HVI (%)	SVR	Remarks
A	Dune sand	Lake	1	19.50	1006751CPT1	30	30	—	—	Low vertical variability
B	Till in hummocky moraine form	Steuben	4	6.50	0810115RB2	52	53	100	MH	Medium vertical variability and high horizontal variability
					0810115TB1	65				
					0810115RB1	28				
					0810115TB2	67				
C	Outwash	LaPorte	2	10.15	0101453TB1	27	26	79	LH	Low vertical variability and high horizontal variability
					0101453TB2	25				
D	Aeolian sand	Newton	1	15.15	1006752CPT2	23	23	—	—	Low vertical variability
E	Outwash	Tippecanoe	3	15.55	0400774CPT2	39	40	71	MH	Medium vertical variability and high horizontal variability
					0400774CPT3	37				
					0400774CPT5	43				
F	Glacial till	Clinton	4	3.17	Frankfort02	69	63	96	MH	Medium vertical variability and high horizontal variability
					Frankfort05	91				
					Frankfort06	37				
					Frankfort07	54				
G	Glacial till	Madison	3	3.00	0101420CPT1	75	57	100	MH	Medium vertical variability and high horizontal variability
					0101420CPT2	55				
					0101420CPT3	40				
H	Glacial till	Decatur	1	8.10	1006241CPT1	69	69	—	—	High vertical variability
I	Loess with sand	Knox	1	14.40	0800579CPT1	68	68	—	—	High vertical variability
J	Lacustrine soil	Vanderburgh	3	19.95	VHC027	43	44	79	MH	Medium vertical variability and high horizontal variability
					VHC028	45				
					VHC033	43				

Note: The site VVI is the average of the individual VVIs of all CPT soundings performed at the site. The first letter in SVR corresponds to the site VVI, while the second letter corresponds to the site HVI. Site HVI values and SVRs could not be assigned for sites where only one CPT sounding was performed.

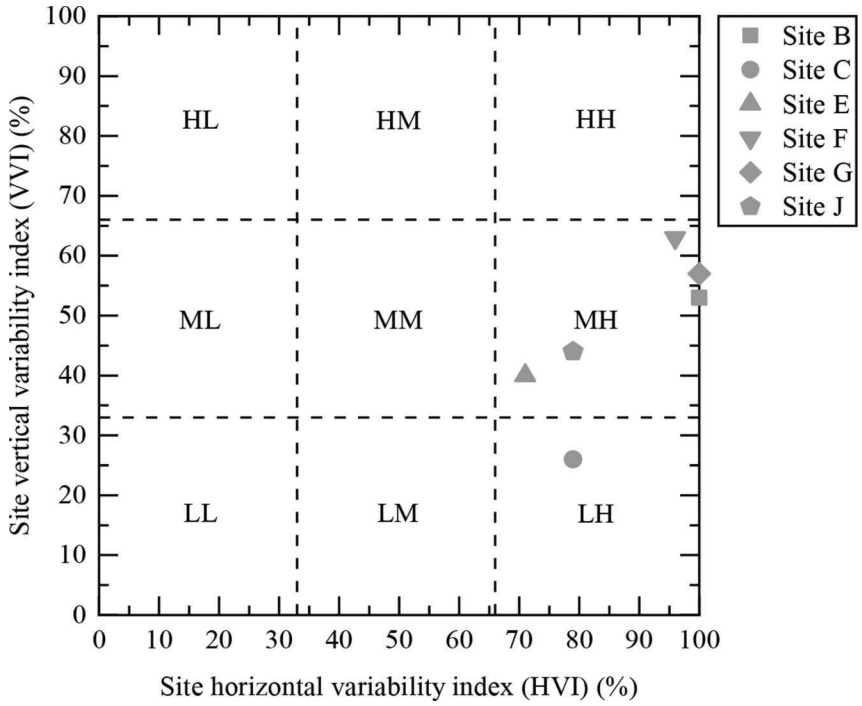

Figure 2.24 Site variability ratings for the sites analyzed.

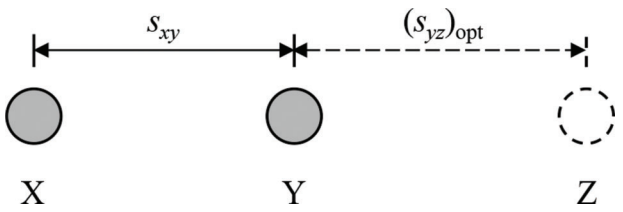

Figure 2.25 Optimal spacing between CPT soundings performed in line (modified from Salgado et al., 2015).

$$\mathrm{HVI} = 1 - f_2[0.8(1 - f_0) + 0.2f_1] \qquad \text{(Eq. 2.17)}$$

The horizontal variability index ranges from 0 for a perfectly uniform site to 1 for a highly variable site.

Step 10: Compute the optimal spacing $(s_{yz})_{opt}$ between CPT sounding Y and the next sounding Z using:

$$(s_{yz})_{opt} = (1.5 - \mathrm{HVI})s_{xy} \qquad \text{(Eq. 2.18)}$$

Equation 2.18 shows that if the value of HVI is greater than 0.5, the spacing for the next CPT sounding is decreased, but if the value of HVI is less than 0.5, the spacing for the next CPT sounding is increased.

Step 11: If the CPT soundings are not performed in line but are distributed in two dimensions, execute the following substeps.

a. Determine the number of pairs of CPT soundings performed at the site using:

$$^{n}C_r = \frac{n!}{(n-r)!r!} \qquad \text{(Eq. 2.19)}$$

where $^{n}C_r$ = number of combinations in which n objects can be selected r at a time, n = number of CPT soundings already performed at the site, and $r = 2$ (for a pair of CPT soundings). The number of pairs of CPT soundings available at a site can also be calculated using the COMBIN function in Microsoft Excel.

b. Repeat steps 1 through 9 for all pairs of CPT soundings performed at the site.
c. Calculate the average of the HVI values for all pairs of CPT soundings performed at the site.
d. Substitute the average HVI value for the site into Eq. 2.18 to obtain the new spacing for the next CPT sounding. The next CPT sounding will be at a distance no greater than $(s_{yz})_{opt}$ from any sounding already performed at the site.

The procedure for estimation of optimal spacing between CPT soundings is presented only to provide some guidance. The spacing between CPT soundings in the field may be adjusted based on the level of importance of the structure, knowledge of the site geology, and soil profile variability.

2.6 Chapter Summary

In this chapter, an overview of the bedrock and surficial geology of Indiana was presented along with the CPT, SPT and soil profiles obtained from ten different locations across Indiana. About two-thirds of Indiana is covered by sediments that were transported and deposited by glaciers during the Ice Age; the

bedrock surface is visible only in the south-central part of the state. The bedrock geology of Indiana mainly consists of five bedrock units: Pennsylvanian, Mississippian, Devonian, Silurian, and Ordovician units, which in turn consist of sedimentary rocks, such as limestone, dolomite, shale, sandstone, and siltstone. Limestone and dolomite dissolve slowly in water to produce karstic landforms (commonly found in southern Indiana) with underground cavities that may collapse, forming sinkholes. The surface geology of Indiana consists of soils transported by wind, water, or ice: (a) dune and aeolian sands in northern Indiana, (b) outwash in northern Indiana and along major river valleys, (c) glacial till in central Indiana, and (d) loess in southwestern Indiana.

CPT and SPT data were obtained from 10 select sites across Indiana. The data was analyzed to obtain depth profiles of cone resistance q_c, sleeve resistance f_s, friction ratio (FR), corrected SPT blow count N_{60}, and $q_c/p_A N_{60}$. The CPT data was post-processed through a soil profile generation algorithm developed by Ganju et al. (2017) to generate SBT profiles for each site using the modified Tumay (1985) SBT chart. According to this chart, a combination of low q_c/p_A (< 10) and high f_s/q_c values ($> 4\%$) suggests a clayey soil, whereas a combination of high q_c/p_A (> 50) and low f_s/q_c values ($< 2\%$) suggests a sandy soil; where p_A = reference stress (= 100 kPa or 14.5 psi). For each site, the CPT-based SBT profiles compared reasonably well with the corresponding soil profiles obtained from the SPT boring logs. The SBT profiles account for the presence of thin layers, which are otherwise not captured by the soil profiles reported in the SPT boring logs. This is because the SBT profiles are based on nearly continuous CPT measurements at depth intervals of 5 cm (2 in.) or less, whereas the soil profiles obtained from the SPT boring logs are based on laboratory testing of soil samples collected typically at depth intervals of 1.5 m (5 ft). The modified Tumay (1985) chart can be used for generating SBT profiles for all soil types in Indiana, except for gravelly materials, for which the modified Robertson (1990) chart is more appropriate.

A correlation between cone resistance q_c, corrected SPT blow count N_{60}, and mean particle size D_{50} was developed based on data reported by Robertson et al. (1983) and data obtained from 15 sites in Indiana. The correlation may be used to obtain an estimate of q_c for use in a CPT-based foundation design method when only SPT blow counts are available for a site because CPT-based methods tend to be more reliable. However, as with any correlation involving the SPT blow count, it should be used with caution because of the potential error introduced by the transformation from the SPT blow count (a dynamic resistance) to the CPT cone resistance (a quasi-static resistance). In such cases when only SPT data is available for the site, it may be preferrable to use SPT-based methods for design (though not in clay) instead of CPT-based methods.

A CPT-based site variability assessment methodology developed by Salgado et al. (2019) was applied to assess the vertical and horizontal variability of the 10 sites in Indiana. The vertical variability of a CPT sounding was quantified via the vertical variability index (VVI), which reflects the intra-layer variability, the log variability and the COV of the cone resistance of the sounding. The site VVI was taken as the average of the individual VVIs of all CPT soundings performed at a site. The horizontal variability of a site was quantified via the site horizontal variability index (site HVI), which depends on the cross-correlation between cone resistance logs, cone resistance trend differences, and the spacing between CPT soundings. The site VVI and HVI values were combined into an overall site variability rating (SVR) system.

A step-by-step procedure for estimation of optimal spacing between CPT soundings was presented (Table 2.5). However, in order to implement the procedure, data from at least two CPT soundings are needed in advance to estimate the optimal spacing of future CPT soundings performed at a site. The procedure may be further refined through future research, and so the use of this procedure in INDOT construction projects is optional based on the level of familiarity of the engineers with the CPT and the specific site investigation goals of the project under consideration. CPT soundings at the desired spacing may be performed based on the level of importance of the structure, knowledge of the site geology, and soil profile variability.

TABLE 2.5
Method for estimation of optimal spacing between CPT soundings (Ganju et al., 2019; Salgado et al., 2015, 2019)

Optimal Spacing Between CPT Soundings $(s_{yz})_{opt}$	Notes
$(s_{yz})_{opt} = (1.5 - \text{HVI}) s_{xy}$ $\text{HVI} = 1 - f_2[0.8(1 - f_0) + 0.2 f_1]$ $f_0 = \min\left[\frac{\lvert\Delta q_{c,avg}\rvert}{\lvert\Delta q_{c,avg}\rvert_{max}}; 1\right]$ $\lvert\Delta q_{c,avg}\rvert = \frac{\sum_{i=1}^{N} \lvert x_i - y_i \rvert}{N}$ $\frac{\lvert\Delta q_{c,avg}\rvert_{max}}{p_A} = 23.86\left(\frac{L}{L_R}\right)^{0.46} - 4.30$ for $1 \le \frac{L}{L_R} \le 30$ $f_1 = \frac{\rho_{xy} + 1}{2}$ and $f_2 = 1 - \exp\left(-0.25 \frac{s_{xy}}{L_R}\right)$ $\rho_{xy} = \frac{C_{xy}}{\sigma_x \sigma_y}$ and $C_{xy} = \frac{1}{N}\sum_{i=1}^{N}(x_i - \bar{x})(y_i - \bar{y})$	The horizontal variability index (HVI) ranges from 0 for a perfectly uniform site to 1 for a highly variable site. If HVI is greater than 0.5, the spacing for the next CPT sounding is decreased, but if HVI is less than 0.5, the spacing for the next CPT sounding is increased. If the CPT soundings are not performed in line but are distributed in two dimensions, calculate the average of the HVI values for all pairs of CPT soundings performed at the site. Substitute the average HVI value into the equation for $(s_{yz})_{opt}$ to obtain the new spacing for the next CPT sounding. The equation for the maximum average q_c difference $\lvert\Delta q_{c,avg}\rvert_{max}$ was obtained by considering two idealized soil profiles, one with a very soft clay layer throughout, and the other with sand having 85% relative density throughout. The cross-correlation coefficient ρ_{xy} takes values in the –1 to +1 range. A high cross-correlation coefficient and small q_c trend difference of a CPT pair indicates high correlation and similarity between the two CPTs, and thus low variability in the horizontal direction for the site.

Note: s_{xy} = spacing between two CPT soundings, X and Y, that have already been performed at a site, $(s_{yz})_{opt}$ = optimal spacing between CPT sounding Y and the next sounding Z that needs to be performed at the site, HVI = horizontal variability index, $\lvert\Delta q_{c,avg}\rvert$ = average q_c difference between CPT soundings X and Y for the segment length considered, N = number of q_c data points contained within the segment length, $\lvert\Delta q_{c,avg}\rvert_{max}$ = maximum credible difference between q_c trends for the segment length considered, L = analysis (segment) length, L_R = reference length (= 1 m or 3.28 ft), p_A = reference stress (= 100 kPa or 14.5 psi), ρ_{xy} = cross-correlation coefficient between CPT soundings X and Y, σ_x and σ_y = standard deviations of the q_c values of CPT soundings X and Y, respectively, C_{xy} = cross-covariance between CPT soundings X and Y, x_i and y_i = q_c values of the i^{th} data point obtained from CPT soundings X and Y, respectively, and $\bar{x}$ and $\bar{y}$ = mean cone resistances of CPT soundings X and Y, respectively, for the segment length considered.

3. CPT-BASED DESIGN OF SHALLOW FOUNDATIONS

Shallow foundations are typically used to support small-to-medium-sized structures on competent soils near the ground surface. The design of a shallow foundation involves two key steps: (a) ultimate limit state check, and (b) serviceability limit state check. Although both bearing capacity and serviceability criteria should be checked properly, only one of the two typically controls the design of shallow foundations depending on the soil type and loading conditions.

3.1 Calculation Procedure for Footing Settlement

The total settlement w of an axially-loaded footing can be calculated from CPT results by following these steps.

Step 1: Obtain the site stratigraphy, the groundwater table depth, and the unit weight of the soil in each layer of the profile.

a. Establish the site stratigraphy either from the boring log or by using a CPT-based soil behavior type (SBT) chart (refer to Section 2.2.3 of Volume I) or both if possible.
b. Obtain the depth z_w of the groundwater table from either the boring log or the depth profile of u_2 or both if possible, where u_2 = pore water pressure measured at the shoulder position behind the cone face (refer to Volume I).
c. Obtain the unit weight of the soil in each layer of the profile whenever soil samples are recovered during the site investigation. In the absence of soil samples, the reader may refer to Section 2.3.3 of Volume I for correlations between the unit weight and CPT data. In general, the saturated unit weight γ_{sat} of soil typically ranges from 18–21 kN/m^3 (115–135 pcf) for sand, 18.5–22.5 kN/m^3 (118–143 pcf) for silty sand, and 15–18 kN/m^3 (95–115 pcf) for clay (Salgado, 2008).

Step 2: Set the footing shape (e.g., strip, square, rectangular, or circular), the preliminary geometry (length L and width B) of the footing, and the embedment depth D of the footing.

Step 3: Classify the soil in each layer of the profile below the footing as either "sand" or "clay." For mixed or intermediate soils (i.e., soils containing mixtures of sand, silt, and clay), execute the following substeps.

a. Sand-silt, sand-clay or sand-silt-clay mixtures: Classify these soils as "clay" if fines content FC ≥ 20% and plasticity index PI ≥ 8%, otherwise classify them as "sand" (Carraro et al., 2009; Salgado et al., 2000).
b. Sands containing gravel: If a site contains sand layers with gravel content greater than 20%, use the lower-

bound profile of q_c, drawn approximately through the valleys of the actual q_c profile, for estimating footing settlement and bearing capacity.

Note: In the absence of soil samples, the reader may refer to Section 2.2 of Volume I for estimation of soil behavior type from CPT results.

Step 4: Correct the raw q_c data for the pore water pressure generated during cone penetration using (ASTM, 2012):

$$q_t = q_c + (1-a)u_2 \qquad \text{(Eq. 3.1)}$$

where q_t = corrected, total cone resistance, q_c = measured cone resistance, a = cone area ratio ($\approx$ 0.8 for typical CPT probes), and u_2 = pore water pressure measured at the shoulder position behind the cone face. The pore water pressure correction to the q_c data may be ignored for coarse-grained soils (e.g., sand and gravel) because q_t is approximately equal to q_c in such soils.

Step 5: Obtain the footing load and maximum tolerable settlement.

a. Obtain the unfactored structural load Q that will be applied on the footing from the structural engineer.
b. Set the maximum tolerable angular distortion α_{max} as 1/500 (Skempton & MacDonald, 1956) or other such value specified by a geotechnical code.
c. Set the maximum tolerable settlement w_{max} of the footing from Table 3.1 or other such value specified by a geotechnical code.

Step 6: Calculate the total settlement of the footing.

a. Total settlement of footings in "sand" (Lee et al., 2008; Lee & Salgado, 2002; Schmertmann, 1970; Schmertmann et al., 1978). Execute the following substeps for footings in "sand," otherwise proceed to step 6(b).

i. Determine the critical-state friction angle ϕ_c of sand through one of the following options.

- Select a ϕ_c value between 28° and 36° for silica sand; sands with rounded, smooth particles with a poorly-graded particle size distribution have values near the low end of this range, while sands with angular, rough particles with a well-graded particle size distribution have values near the high end of this range (refer to Appendix A for additional information if needed).

TABLE 3.1
w_{max}/α_{max} values for shallow foundations in sand and clay (Salgado, 2008; Skempton & MacDonald, 1956)

	w_{max}/α_{max}	
Soil Type	**Isolated Foundations**	**Mat Foundations**
Sand	$15L_R$	$20L_R$
Clay	$25L_R$	$30L_R$

Note: L_R = reference length (= 1 m or 39.4 in.). Strip footings are continuous and behave more like mat foundations than isolated foundations.

- If the mean particle size D_{50}, coefficient of uniformity C_U, and particle roundness R of the sand are known, estimate the critical-state friction angle using:

$$\phi_c(^\circ) = 28.3\left(\frac{D_{50}}{D_{ref}}\right)^{\zeta}(C_U)^{2\zeta}(R)^{-3\zeta} \qquad \text{(Eq. 3.2)}$$

where D_{ref} = reference particle size (= 1 mm or 0.04 in.), and ζ = exponent (= 0.045). Equation 3.2 is applicable for poorly-graded, clean silica sands with D_{50} = 0.15–2.68 mm (0.006–0.105 in.), C_U = 1.2–3.1, and R = 0.3–0.8. The data used in the development of this equation along with example calculations can be found in Appendix A.
- If direct shear or triaxial compression test results are available, it is recommended that the critical-state friction angle be determined from such test results.

ii. Calculate the gross unit load q_b on the footing base (including the loads from the superstructure, the weight of the foundation, and the weight of the backfill when the excavation is backfilled):

$$q_b = \frac{Q + W_{ftg} + W_{fill}}{A} \qquad \text{(Eq. 3.3)}$$

where Q = unfactored column (or wall) load on the footing, W_{ftg} = weight of the footing (= $\gamma_c A t$), γ_c = unit weight of concrete ($\approx$ 24 kN/m^3 or 150 pcf), A = area of the footing base, t = thickness of the footing, W_{fill} = weight of the backfill = max[$\gamma_{fill}A(D - t)$; 0], γ_{fill} = unit weight of the backfill, and D = depth of embedment of the footing. If the footing is not backfilled, W_{fill} = 0. If the thickness of the footing is unknown, an "average" unit weight γ_{avg} may be used for the material above the footing base to calculate the gross unit load q_b:

$$q_b = \frac{Q}{A} + \gamma_{avg}D = \frac{Q}{A} + \left(\frac{\gamma_c + \gamma_{fill}}{2}\right)D \qquad \text{(Eq. 3.4)}$$

iii. Calculate the influence depth z_{f0} measured from the footing base using:

$$\frac{z_{f0}}{B} = 2 + 0.4\left[\min\left(\frac{L}{B}; 6\right) - 1\right] \qquad \text{(Eq. 3.5)}$$

iv. Calculate the depth z_{fp} measured from the footing base at which the strain influence factor peaks using:

$$\frac{z_{fp}}{B} = 0.5 + 0.1\left[\min\left(\frac{L}{B}; 6\right) - 1\right] \qquad \text{(Eq. 3.6)}$$

v. Based on the cone resistance profile, divide the soil layers within the influence depth z_{f0} below the footing base into sublayers such that the q_c values within each sublayer are either approximately constant or linear with depth so that a representative cone resistance can be assigned to each sublayer.

vi. Estimate the strain influence factor I_z for the sublayer using (Figure 3.1):

$$I_z = \begin{cases} I_{z0} + \dfrac{z_f}{z_{fp}}\left(I_{zp} - I_{z0}\right) \text{ for } z_f < z_{fp} \\ \dfrac{z_{f0} - z_f}{z_{f0} - z_{fp}} I_{zp} \text{ for } z_{fp} \le z_f \le z_{f0} \end{cases} \quad \text{(Eq. 3.7)}$$

where z_f = vertical distance from the footing base to the middle of the sublayer, I_{z0} = strain influence factor at the footing base level, and I_{zp} = peak strain influence factor:

$$I_{z0} = \min\left[0.1 + 0.0111\left(\frac{L}{B} - 1\right); 0.2\right] \quad \text{(Eq. 3.8)}$$

$$I_{zp} = 0.5 + 0.1\sqrt{\frac{q_b - \sigma'_{v0}\big|_{z_f=0}}{\sigma'_{v0}\big|_{z_f=z_{fp}}}} \quad \text{(Eq. 3.9)}$$

where $\sigma'_{v0}\big|_{z_f=0}$ = *in situ* vertical effective stress at the footing base level, and $\sigma'_{v0}\big|_{z_f=z_{fp}}$ = *in situ* vertical effective stress at the depth corresponding to z_{fp}.

vii. Determine the coefficient of lateral earth pressure at-rest K_0 of the sublayer (refer to Appendix B for guidance).

viii. Estimate the relative density D_R of the sublayer using (Salgado & Prezzi, 2007):

$$D_R(\%) = \frac{\ln\left(\frac{q_c}{p_A}\right) - 0.4947 - 0.1041\phi_c - 0.841\ln\left(\frac{\sigma'_{h0}}{p_A}\right)}{0.0264 - 0.0002\phi_c - 0.0047\ln\left(\frac{\sigma'_{h0}}{p_A}\right)} \quad \text{(Eq. 3.10)}$$

where q_c = representative cone resistance of the sublayer, p_A = reference stress (= 100 kPa or 14.5 psi), σ'_{h0} = *in situ* horizontal effective stress at the middle of the sublayer (= $K_0\sigma'_{v0}$), and σ'_{v0} = *in situ* vertical effective stress at the middle of the sublayer (Terzaghi, 1943):

$$\sigma'_{v0} = \sigma_{v0} - u_0 \quad \text{(Eq. 3.11)}$$

where σ_{v0} = *in situ* vertical total stress at the middle of the sublayer, u_0 = hydrostatic pore water pressure at the middle of the sublayer {= max[γ_w ($z - z_w$) ; 0]}, γ_w = unit weight of water (= 9.81 kN/m^3 or 62.45 pcf), z = depth measured from the ground surface to the middle of the sublayer, and z_w = depth of the groundwater table.

ix. Estimate the elastic modulus E of the sublayer using:

$$\frac{E}{q_c} = \lambda\left(\frac{w}{L_R}\right)^{-0.285}\left(\frac{B}{L_R}\right)^{0.4}\left(\frac{D_R}{100}\right)^{-0.65} \quad \text{(Eq. 3.12)}$$

$$\lambda = \begin{cases} 0.38 & \text{for young NC silica sand} \\ 0.53 & \text{for aged NC silica sand} \\ 0.91 & \text{for over OC silica sand} \end{cases} \quad \text{(Eq. 3.13)}$$

where w = initial guess value for footing settlement (= w_{max} established in step 5), B = width or diameter of the footing, L_R = reference length (= 1 m or 3.28 ft), D_R = relative density of the sublayer (expressed as a percentage), and λ = parameter that accounts for the effects of aging and overconsolidation of sand.

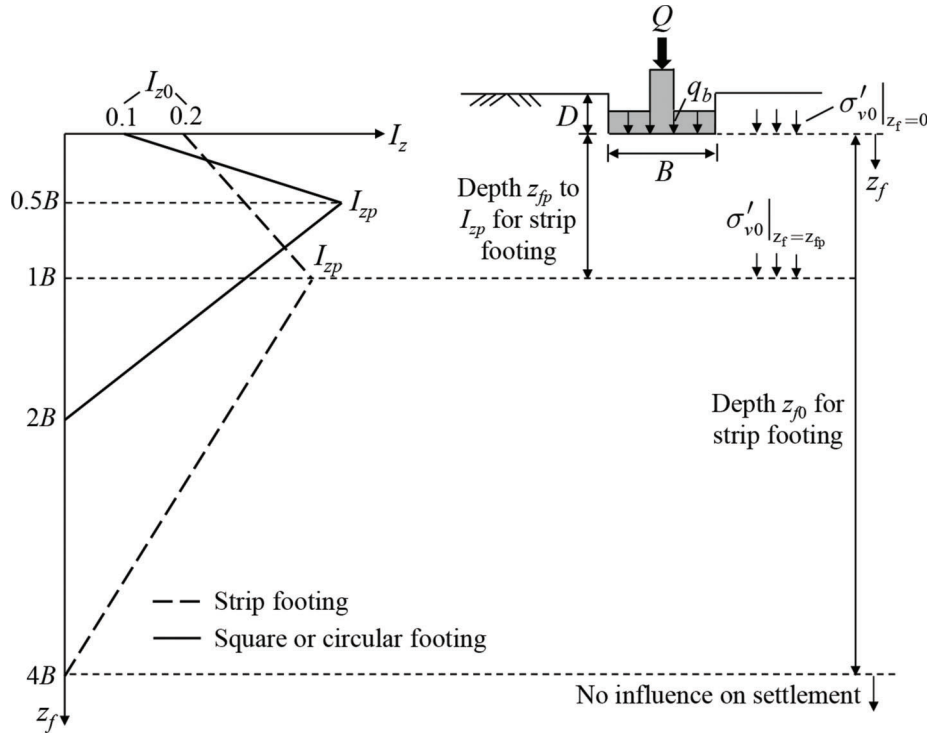

Figure 3.1 Strain influence factor I_z versus depth z_f below the footing base (after Salgado 2008; Schmertmann et al., 1978).

x. Compute the total settlement w of the footing using:

$$w = C_1 C_2 \left(q_b - \sigma'_{v0}\big|_{z_f=0}\right) \sum_{i=1}^{n} \left(\frac{I_{zi}\Delta z_i}{E_i}\right) \quad \text{(Eq. 3.14)}$$

where Δz = thickness of the sublayer, n = number of sublayers within the influence depth z_{f0} below the footing base, and C_1 and C_2 = depth and time factors, respectively:

$$C_1 = 1 - 0.5\left(\frac{\sigma'_{v0}\big|_{z_f=0}}{q_b - \sigma'_{v0}\big|_{z_f=0}}\right) \quad \text{(Eq. 3.15)}$$

$$C_2 = 1 + 0.2\log\left(\frac{t}{0.1t_R}\right) \quad \text{(Eq. 3.16)}$$

where t_R = reference time (= 1 year), and t = service life of the superstructure (in the same unit as t_R).

xi. Compare the value of w calculated using Eq. 3.14 with the initial guess value assumed in substep (ix). If the two values match, then report the value of w calculated using Eq. 3.14 as the settlement of the footing. However, if they do not match, return to substep (ix) and use the new value of w obtained from Eq. 3.14 as the initial guess value for the next iteration (refer to Appendix C for guidance).

b. Total settlement of footings in "clay." Execute the following substeps for footings in "clay," otherwise proceed to step 7.

Immediate settlement of footings in clay (Foye et al., 2008)

i. Obtain the depth profile of undrained shear strength s_u below the footing base using (Salgado, 2008):

$$s_u = \frac{q_t - \sigma_{v0}}{N_k} \quad \text{(Eq. 3.17)}$$

where q_t = corrected, total cone resistance measured under undrained conditions, σ_{v0} = *in situ* vertical total stress at the depth being considered, and N_k = cone factor (≈ 9–15 as long as the CPT is performed at a penetration rate that is sufficiently high to ensure undrained penetration (refer to Appendix D); soft NC clays tend to have N_k values near the low end of this range, while stiff OC clays tend to have N_k values near the high end of this range) (Bisht et al., 2021; Mayne & Peuchen, 2018; Salgado, 2008, 2013, 2014; Salgado et al., 2004).

ii. Average the values of s_u over a vertical distance of B below the footing base to obtain a representative undrained shear strength $\bar{s}_u$.

iii. Calculate the influence depth $z_{\bar{G}_0}$ below the footing base within which most of the strains develop using:

$$\frac{z_{\bar{G}_0}}{B} = \min\left[1 + 0.111\left(\frac{L}{B} - 1\right); 2\right] \quad \text{(Eq. 3.18)}$$

iv. Obtain the small-strain shear modulus G_0 profile within the influence depth $z_{\bar{G}_0}$ below the footing base from the results of seismic cone penetration tests (SCPTs) using (Salgado, 2008):

$$G_0 = \frac{\gamma_m}{g} V_s^2 \quad \text{(Eq. 3.19)}$$

where γ_m = unit weight of soil (= γ_{sat} if the soil is saturated), g = acceleration due to gravity (= 9.81 m/s^2 or 32.17 ft/s^2), and V_s = shear wave velocity (refer to Section 2.3.4 of Volume I).

If SCPT results are unavailable, the small-strain shear modulus may be estimated using the following correlation (Viggiani & Atkinson, 1995):

$$\frac{G_0}{p_A} = C_g \left(\frac{100\sigma'_{m0}}{p_A}\right)^{n_g} R_0^{m_g} \quad \text{(Eq. 3.20)}$$

where C_g, n_g, and m_g = parameters that depend on the plasticity index PI; σ'_{m0} = *in situ* mean effective stress at the depth being considered; p_A = reference stress (= 100 kPa or 14.5 psi); and R_0 = mean stress-based overconsolidation ratio:

$$R_0 = \frac{p'_p}{p'} = \text{OCR}\left(\frac{1 + 2K_{0,\text{NC}}}{1 + 2K_{0,\text{NC}}\sqrt{\text{OCR}}}\right) \quad \text{(Eq. 3.21)}$$

where p'_p = value of p' at the intersection of the recompression line with the normal consolidation line in v–ln p' space, v = specific volume (= 1+e), $K_{0,\text{NC}}$ = coefficient of lateral earth pressure at-rest for normally consolidated soil (≈ 0.50–0.75 for NC clay), and OCR = overconsolidation ratio (refer to Appendix B for guidance).

The parameters C_g, n_g, and m_g can be calculated using (Foye et al., 2008; Viggiani & Atkinson, 1995):

$$C_g = 37.9 \ \exp\left(-0.045 \ \text{PI}\right) \text{ for PI} > 5\% \quad \text{(Eq. 3.22)}$$

$$n_g = 0.109 \ \ln\left(\text{PI}\right) + 0.4374 \text{ for PI} > 5\% \quad \text{(Eq. 3.23)}$$

$$m_g = 0.0015 \ \text{PI} + 0.1863 \text{ for PI} > 5\% \quad \text{(Eq. 3.24)}$$

The *in situ* mean effective stress can be calculated using:

$$\sigma'_{m0} = \frac{1}{k+1}\left(\sigma'_{v0} + k\sigma'_{h0}\right) \quad \text{(Eq. 3.25)}$$

where k = 1 for plane-strain conditions (e.g., strip footings) and 2 for triaxial conditions (e.g., isolated footings), σ'_{v0} = *in situ* vertical effective stress at the depth being considered, σ'_{h0} = *in situ* horizontal effective stress at the depth being considered (= $K_0\sigma'_{v0}$), and K_0 = coefficient of lateral earth pressure at-rest (refer to Appendix B for guidance). The plasticity index PI is the difference between the liquid limit LL and the plastic limit PL of the soil (PI = LL – PL).

v. Calculate a representative small-strain shear modulus $\bar{G}_0$ by taking the weighted average of the G_0 values

within the influence depth $z_{\bar{G}_0}$ below the footing base:

$$\bar{G}_0 = \frac{\sum_{i=1}^{n} G_{0,i}^{\text{avg}} H_i}{\sum_{i=1}^{n} H_i} \quad \text{(Eq. 3.26)}$$

where $G_{0,i}^{\text{avg}}$ = average small-strain shear modulus of layer i, H_i = thickness of layer i, and n = number of clay layers within the influence depth $z_{\bar{G}_0}$ below the footing base.

vi. Using trial footing dimensions, estimate the net unit load $q_{b,\text{net}}$ on the footing base:

$$q_{b,\text{net}} = q_b - \gamma_m D \quad \text{(Eq. 3.27)}$$

where q_b = gross unit load on the footing base (including the loads from the superstructure, the weight of the foundation, and the weight of the backfill when the excavation is backfilled; refer to Eqs. 3.3 and 3.4), and $\gamma_m D$ = total overburden stress at the footing base level.

vii. Obtain the influence factor I_q from Figure 3.2; H = thickness of the clay layer below the footing base, and B = footing width. For circular footings, an equivalent footing width may be obtained by equating the cross-sectional area of the footing with that of an equivalent square.

viii. Estimate the representative small-strain Young's modulus $\bar{E}_0$ of clay below the footing base using:

$$\bar{E}_0 = 2(1+\nu)\bar{G}_0 \quad \text{(Eq. 3.28)}$$

where ν = Poisson's ratio (= 0.5 for undrained conditions).

ix. Compute the immediate settlement w_i of the footing using:

$$w_i = I_q \frac{q_{b,\text{net}} B}{\bar{E}_0} \quad \text{(Eq. 3.29)}$$

Primary consolidation settlement of footings in clay (Skempton & Bjerrum, 1957)

i. Divide the clay layer below the footing base into n sublayers of thickness Δz.

ii. Calculate the vertical stress increment $\Delta\sigma_v$ at the middle of each sublayer caused by the applied load Q using the 2-to-1 stress distribution rule:

$$\Delta\sigma_v = \begin{cases} \dfrac{Q}{B+z_f} & \text{for strip footings} \\ \dfrac{4Q}{\pi(B+z_f)^2} & \text{for circular footings} \\ \dfrac{Q}{(B+z_f)(L+z_f)} & \text{for rectangular footings} \end{cases} \quad \text{(Eq. 3.30)}$$

where z_f = vertical distance from the footing base to the middle of the sublayer. Q takes units of load per unit length for strip footings and units of load for all other footings.

iii. Obtain the initial void ratio e_0 of the sublayer using the relationship $e_0 = \text{wc}G_s/S$; where wc = water content, G_s = specific gravity of solids (= 2.60–2.80 for clay), and S = degree of saturation (= 1 for saturated clay). In the absence of soil samples, the reader may refer to Section 2.3.1 of Volume I for additional information on e_0.

iv. Estimate the vertical compressive strain $\Delta\varepsilon_z$ of the sublayer using:

$$\Delta\varepsilon_z = \begin{cases} \frac{C_c}{1+e_0}\log\left(\frac{\sigma'_v}{\sigma'_{v0}}\right) \text{ if } \sigma'_{v0} = \sigma'_{vp} \text{ and } \sigma'_v \geq \sigma'_{vp} (\text{NC clay}) \\ \frac{1}{1+e_0}\left[C_s \log\left(\frac{\sigma'_{vp}}{\sigma'_{v0}}\right) + C_c \log\left(\frac{\sigma'_v}{\sigma'_{vp}}\right)\right] \\ \text{if } \sigma'_{v0} < \sigma'_{vp} \leq \sigma'_v (\text{OC then NC clay}) \\ \frac{C_s}{1+e_0}\log\left(\frac{\sigma'_v}{\sigma'_{v0}}\right) \text{ if } \sigma'_{v0} \leq \sigma'_{vp} \text{ and } \sigma'_v \leq \sigma'_{vp} (\text{OC clay}) \end{cases} \quad \text{(Eq. 3.31)}$$

where σ'_{v0} = initial (or *in situ*) vertical effective stress at the middle of the sublayer before the stress increment is applied, σ'_v = current vertical effective stress at the middle of the sublayer after the stress increment is applied and full primary consolidation has taken place (= $\sigma'_{v0} + \Delta\sigma_v$), σ'_{vp} = preconsolidation stress, C_c = compression index, and C_s = swelling index.

In the absence of laboratory consolidation test results, the compression index C_c may be estimated using the following approximate correlation (Wroth & Wood, 1978):

$$C_c \approx \frac{1}{200} G_s \text{PI}(\%) \quad \text{(Eq. 3.32)}$$

where PI = plasticity index (expressed as a percentage). The swelling index C_s typically ranges from $0.1C_c$ to $0.2C_c$.

v. Compute the 1D consolidation settlement $w_{c1\text{D}}$ of the clay layer below the footing base using:

$$w_{c1\text{D}} = \sum_{i=1}^{n} \Delta\varepsilon_{z,i} \Delta z_i \quad \text{(Eq. 3.33)}$$

where Δz_i = thickness of sublayer i, and n = number of sublayers.

vi. Compute the primary consolidation settlement w_c of the footing using:

$$w_c = [A + \alpha(1-A)] w_{c1\text{D}} \quad \text{(Eq. 3.34)}$$

$$\alpha = \frac{\int_0^H \Delta\sigma_3 dz}{\int_0^H \Delta\sigma_1 dz} \quad \text{(Eq. 3.35)}$$

where A = Skempton's pore pressure parameter (≈ 0.5–0.75 for NC clay and 0.3–0.5 for OC clay), $\Delta\sigma_1$ = major principal stress increment, $\Delta\sigma_3$ = minor principal stress increment, and H = thickness of the clay layer below the footing base.

Table 3.2 summarizes the values of α for circular and strip footings as a function of H/B. For square

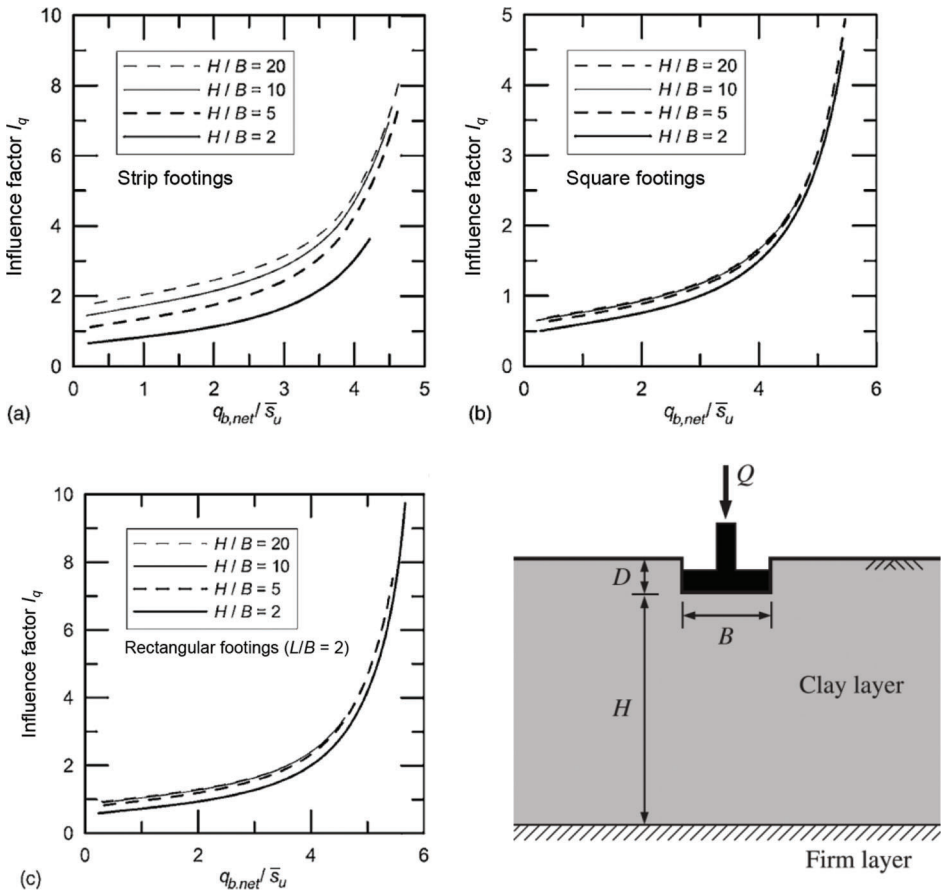

Figure 3.2 Influence factor I_q as a function of $q_{b,net}/\bar{s}_u$ and H/B for (a) strip footings, (b) square footings, and (c) rectangular ($L/B = 2$) footings (Foye et al., 2008; Salgado, 2008).

TABLE 3.2
Values of α for estimation of primary consolidation settlement of footings in clay (Skempton & Bjerrum, 1957)

	Coefficient α	
Normalized Thickness of Clay Layer H/B	**Circular Footing ($B/L = 1$)**	**Strip Footing ($B/L = 0$)**
0	1.00	1.00
0.25	0.67	0.74
0.5	0.50	0.53
1	0.38	0.37
2	0.30	0.26
4	0.28	0.20
10	0.26	0.14
∞	0.25	0

footings, the value of α for a circular footing with the same cross-sectional area as that of a square footing may be used. For rectangular footings with $0 < B/L < 1$, obtain the value of α by interpolation.

vii. Sum the values of w_i and w_c to obtain the total settlement w of the footing. Note that if significant secondary consolidation is expected at the site, it should be considered together with primary consolidation.

Step 7: Total settlement check.

Compare the estimated total settlement w of the footing with the maximum tolerable settlement w_{max} selected in step 5. If $w \leq w_{max}$, the footing design is satisfactory with respect to the serviceability limit state (i.e., excessive settlement). Repeat step 6 to optimize the design if needed. However, if $w > w_{max}$, return to step 6 and revise the footing geometry.

Step 8: Angular distortion check.

Execute the following substeps for each pair of adjacent footings at the site.

a. Compute the angular distortion α for the selected footing pair using:

$$\alpha = \frac{\Delta w}{L_{cc}} \qquad \text{(Eq. 3.36)}$$

where Δw = differential settlement, and L_{cc} = span or center-to-center distance between the two footings.

b. Compare the estimated angular distortion α for the given footing pair with the maximum tolerable angular distortion α_{max} selected in step 5. If $\alpha \leq \alpha_{max}$, the footing design is satisfactory with respect to the ultimate/serviceability limit state (i.e., excessive differential settlement). If $\alpha > \alpha_{max}$, redo the footing design until the maximum tolerable angular distortion criterion is satisfied. If the criterion cannot be satisfied, consider alternative design solutions, such as the use of grade beams; combined footings; replacement of foundation soil with compacted, coarse-grained material; geosynthetic-reinforced foundation bed; mat (or raft) foundations; pile foundations; and piled rafts.

3.2 Calculation Procedure for Limit Bearing Capacity of Footings

The limit unit bearing capacity q_{bL} of an axially-loaded footing can be calculated from CPT results by following these steps.

Step 1: Determine the nominal or characteristic cone resistance $q_{c,\mathrm{CAM}}$.

a. Combine the cone resistance profiles obtained from all CPT soundings performed at the site. Note that, for fine-grained soils (e.g., silts and clays), the cone resistance should be corrected for pore water pressure u_2 using Eq. 3.1.
b. Perform a linear regression on the cone resistance data points to obtain the mean trend of the data with depth (Figure 3.3). When performing the regression, consider only those data points that follow the general trend of the q_c profile and ignore any outliers or regions that contain significant scatter in the data.
c. Draw lines (parallel to the mean trendline) bounding the cone resistance data points, as shown in Figure 3.3.
d. Determine the relationship of cone resistance with depth that is exceeded by 80% of the measurements using (Foye et al., 2006b):

$$q_{c,\mathrm{CAM}}(z) = E_{q_c}(z) - 0.84\sigma_{q_c} \qquad \text{(Eq. 3.37)}$$

where $q_{c,\mathrm{CAM}}(z)$ = conservatively assessed mean (CAM) cone resistance determined using the 80% exceedance criterion (Becker, 1996) (as a function of depth z), $E_{qc}(z)$ = equation of the mean trendline obtained from the regression analysis, and σ_{qc} = standard deviation of cone resistance (Foye et al., 2006a):

$$\sigma_{qc} = \frac{(q_{c,\max} - q_{c,\min})_{\mathrm{sample}}}{N_\sigma} \qquad \text{(Eq. 3.38)}$$

where $q_{c,\max}$ = value of cone resistance at any depth z on the upper bound line, $q_{c,\min}$ = value of cone resistance on the lower bound line at the same depth z at which $q_{c,\max}$ was computed (see Figure 3.3), and N_σ = number of standard deviations of q_c (obtained from Table 3.3).

Step 2: Calculate the limit unit bearing capacity of the footing.

a. Limit unit bearing capacity of footings in "sand." Execute the following substeps for footings in "sand," otherwise proceed to step 2(b).
i. Using the values of z_w, B and D determined from Section 3.1, calculate the value of the unit weight γ to use in the bearing capacity equation:

$$\gamma = \begin{cases} \gamma_b \text{ if } z_w < D \\ \gamma_b + \left(\dfrac{z_w - D}{B}\right)(\gamma_m - \gamma_b) \text{ if } D \leq z_w \leq D + B \\ \gamma_m \text{ if } z_w > D + B \end{cases} \qquad \text{(Eq. 3.39)}$$

where z_w = depth of the groundwater table, B = footing width or diameter, D = depth of embedment of the footing, γ_m = moist unit weight of sand, γ_b = buoyant unit weight of sand (= $\gamma_{sat} - \gamma_w$), γ_{sat} = saturated unit weight of sand, and γ_w = unit weight of water (= 9.81 kN/m^3 or 62.45 lb/ft^3).
ii. Estimate the relative density D_R of sand at a depth of $B/2$ below the footing base using:

$$D_R(\%) = \frac{\ln\left(\dfrac{q_{c,\mathrm{CAM}}}{p_A}\right) - 0.4947 - 0.1041\phi_c - 0.841\ln\left(\dfrac{\sigma'_{h0}}{p_A}\right)}{0.0264 - 0.0002\phi_c - 0.0047\ln\left(\dfrac{\sigma'_{h0}}{p_A}\right)} \qquad \text{(Eq. 3.40)}$$

where $q_{c,\mathrm{CAM}}$ = conservatively assessed mean (CAM) cone resistance at a depth of $B/2$ below the footing base (obtained from Eq. 3.37), σ'_{v0} = *in situ* vertical effective stress at a depth of $B/2$ below the footing base, σ'_{h0} = *in situ* horizontal effective stress at a depth of $B/2$ below the footing base (= $K_0\sigma'_{v0}$), p_A = reference stress (= 100 kPa or 14.5 psi), ϕ_c = critical-state friction angle (refer to step 6(a)(i) of Section 3.1), and K_0 = coefficient of lateral earth pressure at-rest (refer to Appendix B for guidance).
iii. Calculate the peak friction angle ϕ_p of sand using (Bolton, 1986):

$$\phi_p = \phi_c + A_\psi\left\{\frac{D_R}{100}\left[Q - \ln\left(\frac{100\sigma'_{mp}}{p_A}\right)\right] - R_Q\right\} \qquad \text{(Eq. 3.41)}$$

$$A_\psi = \min\left[\frac{1}{3}\left(\frac{L}{B} + 8\right); 5\right] \qquad \text{(Eq. 3.42)}$$

where p_A = reference stress (= 100 kPa or 14.5 psi), Q and R_Q = fitting parameters that depend on the intrinsic characteristics of sand (Q = 10 and R_Q = 1 for clean silica sand), and σ'_{mp} = representative mean effective stress (Loukidis, 2006; Salgado, 2008):

$$\sigma'_{mp} = 20p_A\left(\frac{\gamma B}{p_A}\right)^{0.7}\left(1 - 0.32\frac{B}{L}\right) \qquad \text{(Eq. 3.43)}$$

iv. Calculate the shape factors s_q and s_γ using (Lyamin et al., 2007):

$$s_q = 1 + (0.098\phi_p - 1.64)\left(\frac{D}{B}\right)^{0.7 - 0.01\phi_p}\left(\frac{B}{L}\right)^{1 - 0.16\left(\frac{D}{B}\right)} \qquad \text{(Eq. 3.44)}$$

$$s_\gamma = 1 + (0.0336\phi_p - 1)\frac{B}{L} \qquad \text{(Eq. 3.45)}$$

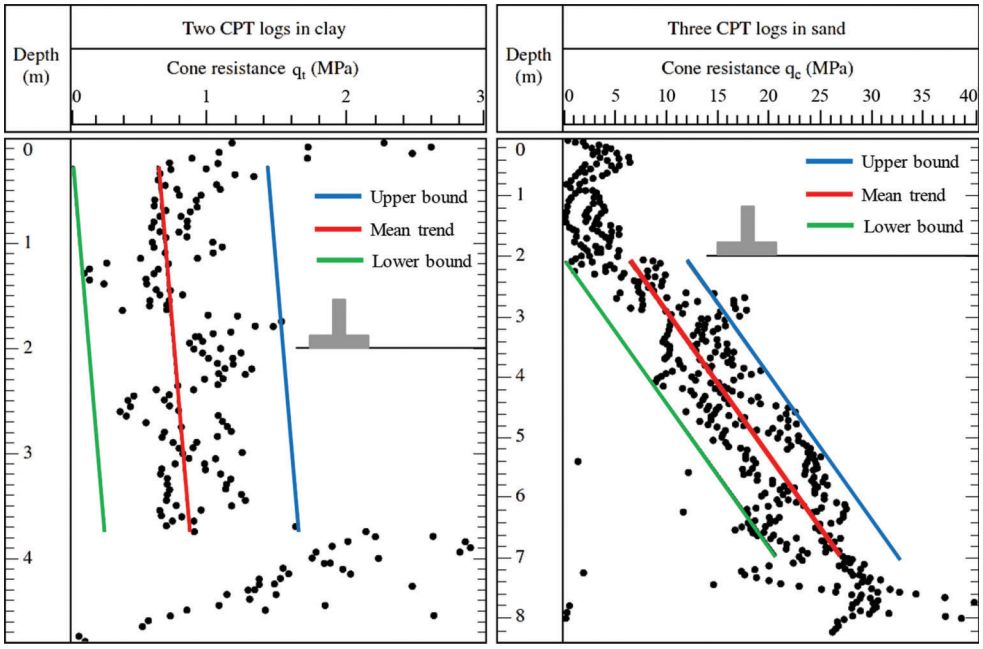

Figure 3.3 Examples of two CPT logs in clay and three CPT logs in sand with mean trendlines and range lines (after Foye et al., 2006a).

TABLE 3.3
Values of N_σ as a function of sample size n (after Tippett, 1925)

n	N_σ	n	N_σ	n	N_σ
2	1.128379	12	3.258457	100	5.0152
3	1.692569	13	3.335982	200	5.492108
4	2.058751	14	3.406765	300	5.755566
5	2.325929	15	3.471828	400	5.936396
6	2.534413	16	3.531984	500	6.073445
7	2.704357	17	3.587886	600	6.183457
8	2.847201	18	3.640066	700	6.275154
9	2.970027	19	3.688965	800	6.353645
10	3.077506	20	3.734952	900	6.422179
11	3.172874	50	4.498153	1,000	6.482942

Note: n = number of cone resistance data points contained within the upper and lower bound lines (see Figure 3.3). For intermediate values of n, the value of N_σ may be obtained by linear interpolation.

For circular footings, the s_q and s_γ equations should be multiplied by an additional term equal to 1 + $0.0025\phi_p$ and 1 + $0.002\phi_p$, respectively.

v. Estimate the depth factor d_q using (Lyamin et al., 2007):

$$d_q = 1 + \left(0.0036\phi_p + 0.393\right)\left(\frac{D}{B}\right)^{-0.27} \qquad \text{(Eq. 3.46)}$$

vi. Calculate the bearing capacity factors N_q and N_γ using (Loukidis & Salgado, 2011; Reissner, 1924):

$$N_q = \frac{1+\sin\phi_p}{1-\sin\phi_p} e^{\pi\tan\phi_p} \qquad \text{(Eq. 3.47)}$$

$$N_\gamma = \left(N_q - 0.6\right)\tan\left(1.33\phi_p\right) \qquad \text{(Eq. 3.48)}$$

vii. Compute the limit unit bearing capacity q_{bL} of the footing using (Lyamin et al., 2007):

$$q_{bL} = \left(s_q d_q\right) q_0 N_q + 0.5\left(s_\gamma d_\gamma\right)\gamma B N_\gamma \qquad \text{(Eq. 3.49)}$$

where q_0 = surcharge (vertical effective stress) at the footing base level, and d_γ = depth factor (= 1). For strip footings, the shape factors s_q and s_γ are equal to 1. Note that additional factors would have to be added to the bearing capacity equation (Eq. 3.49) to account for load inclination, footing base inclination, and ground inclination, as needed.

b. Limit unit bearing capacity of footings in "clay." Execute the following substeps for footings in "clay," otherwise proceed to step 3.

   i. Determine the undrained shear strength s_u profile below the footing base from CPT results using (Foye et al., 2006a,b; Salgado, 2008):

$$s_u(z) = \frac{q_{c,\mathrm{CAM}}(z) - \sigma_{v0}(z)}{N_k} \qquad \text{(Eq. 3.50)}$$

   where $q_{c,\mathrm{CAM}}(z)$ = conservatively assessed mean (CAM) cone resistance (as a function of depth z) corrected for pore water pressure u_2, $\sigma_{v0}(z)$ = *in situ* vertical total stress (as a function of depth z), and N_k = cone factor ($\approx$ 9–15 as long as the CPT is performed at a penetration rate that is sufficiently high to ensure undrained penetration (refer to Appendix D); soft NC clays tend to have N_k values near the low end of this range, while stiff OC clays tend to have N_k values near the high end of this range).

   ii. Using Eq. 3.50, determine the strength gradient ρ with depth and the undrained shear strength s_{u0} at the footing base level.

   iii. Determine the correction factor F from Figure 3.4 based on whether the s_u profile below the footing base resembles profile 1 or profile 2. Profile 1 represents an NC clay deposit with s_u increasing linearly with depth from a nonzero value s_{u0} at the footing base level. Profile 2 represents an NC clay deposit below a certain depth, with the footing base resting on an OC crust for which s_u is constant with depth; z_f = depth measured from the footing base.

   iv. Estimate the shape factor s_{su} and depth factor d_{su} using (Salgado, 2008; Salgado et al., 2004):

$$s_{su} = 1 + C_1 \frac{B}{L}\left\{\frac{2.3}{\exp\left[0.353\left(\frac{\rho B}{s_{u0}}\right)^{0.509}\right]} - 1.3\right\} + C_2\sqrt{\frac{D}{B}} \qquad \text{(Eq. 3.51)}$$

$$d_{su} = 1 + 0.27\sqrt{\frac{D}{B}} \qquad \text{(Eq. 3.52)}$$

   where B = footing width, L = footing length, and C_1 and C_2 = coefficients that depend on the aspect ratio B/L of the footing (Table 3.4).

   v. Compute the limit unit bearing capacity q_{bL} of the footing using (Salgado, 2008):

$$q_{bL} = F s_{su} d_{su}\left[1 + \frac{\rho B}{4 s_{u0} N_c}\right] s_{u0} N_c + q_0 \qquad \text{(Eq. 3.53)}$$

   where N_c = bearing capacity factor (= $2 + \pi \approx 5.14$) (Prandtl, 1920, 1921), and q_0 = surcharge (vertical total stress) at the footing base level.

3.3 Load and Resistance Factor Design Procedure for Footings

Load and resistance factor design (LRFD) of axially-loaded footings can be done from CPT results by following these steps.

Step 1: Obtain the nominal dead load DL_n and the nominal live load LL_n on the footing from the superstructure design.

Step 2: Set the load factors for dead load and live load, LF_{DL} and LF_{LL}, as 1.25 and 1.75, respectively (AASHTO, 2020). These load factors correspond to the Strength I limit state (basic load combination relating to the normal vehicular use of the bridge without wind), as defined by AASHTO (2020). The discussion of other limit states, such as Strength II–V, Extreme Event I and II, Service I–IV, and Fatigue I and II are beyond the scope of the manual—information about these limit states can be found in AASHTO (2020).

Step 3: Calculate the nominal resistance R_n of the footing using:

$$R_n = q_{bL,\mathrm{net}} A \qquad \text{(Eq. 3.54)}$$

where $q_{bL,\mathrm{net}}$ = net limit unit bearing capacity of the footing (= $q_{bL} - q_0$), q_{bL} = limit unit bearing capacity of the footing (obtained from Section 3.2), q_0 = surcharge at the footing base level, and A = area of the footing base.

Step 4: Obtain the resistance factor.

Table 3.5 summarizes the resistance factors for load and resistance factor design of footings using the bearing capacity equations (Eqs. 3.49 and 3.53) presented in this chapter, while Table 3.6 summarizes the resistance factors and footing design methods advocated by AASHTO (2020).

Step 5: Verify that the following LRFD inequality is satisfied (Foye et al., 2006b; Salgado, 2008):

$$(RF) R_n \geq LF_{DL} DL_n + LF_{LL} LL_n \qquad \text{(Eq. 3.55)}$$

If Eq. 3.55 is satisfied, the footing design is satisfactory with respect to the ultimate limit state (i.e., classical bearing capacity failure). Repeat steps 3 to 5 to optimize the design if needed. However, if Eq. 3.55 is not satisfied, return to step 3 and revise the footing geometry.

Note: The following equation may be used, if needed, to obtain an equivalent factor of safety (FS) for the footing design produced using LRFD (Salgado, 2008):

$$\mathrm{FS} = b_R \frac{LF_{DL} + LF_{LL}\left(\frac{LL_n}{DL_n}\right)}{\left(\frac{LL_n}{DL_n} + 1\right) RF} \qquad \text{(Eq. 3.56)}$$

where b_R = bias factor (= R/R_n), R = mean resistance of the footing (calculated from q_{bL} using the mean cone resistance profile (Figure 3.3)), and R_n = nominal resistance of the footing (calculated from q_{bL} using the conservatively assessed mean cone resistance $q_{c,\mathrm{CAM}}$ obtained from Eq. 3.37). To obtain a quick estimate of the equivalent factor of safety, the value of the bias factor b_R may be taken as 1.

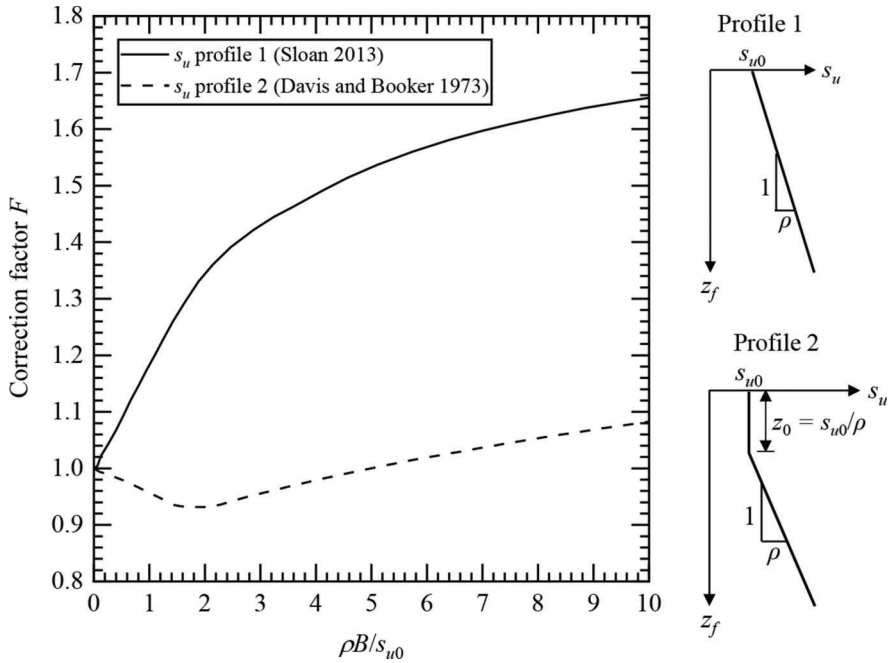

Figure 3.4 F versus $\rho B/s_{u0}$ for a rough footing base in clay.

TABLE 3.4
Values of C_1 and C_2 to use in Eq. 3.51 as a function of B/L (Salgado, 2008; Salgado et al., 2004)

B/L	C_1	C_2
1 (circle)	0.163	0.210
1 (square)	0.125	0.219
0.50	0.156	0.173
0.33	0.159	0.137
0.25	0.172	0.110
0.20	0.190	0.090

3.4 Chapter Summary

In this chapter, detailed, step-by-step procedures for computing the total settlement w and limit unit bearing capacity q_{bL} of axially-loaded footings from CPT results in sand (silica sand) and clay were presented. Guidelines for footings installed in mixed or intermediate soils, such as sand-silt or sand-clay mixtures, were provided based on the concept of floating versus nonfloating soil fabric.

Methods for estimation of immediate settlement of footings in sand and clay require a representative value of the elastic modulus of the soil below the footing under drained and undrained conditions, respectively. For sands, the ratio of the elastic modulus to the cone resistance is a function of footing settlement level, footing size, and relative density. For clays, the elastic modulus is obtained through the small-strain shear modulus, which can be estimated either from the shear wave velocity (if SCPT results are available) or from the mean effective stress, plasticity index, and OCR.

The method for estimation of primary consolidation settlement of a footing in clay is basically a modification of that used to estimate the one-dimensional consolidation settlement caused by the application of an instantaneous uniform load extending to infinity horizontally; the modification accounts for the three-dimensional effects that arise due to the finite size of the footing. In this method, the main soil variables are initial void ratio, compression index, swelling index, and preconsolidation stress. If significant secondary consolidation is expected at the site, it should be considered together with primary consolidation.

The limit unit bearing capacity of a footing in clay is calculated assuming that the loads are applied rapidly compared to the drainage rate of clay and that the short term is the critical loading condition; therefore, loading takes place under undrained conditions. In contrast, the limit unit bearing capacity of a footing in sand is calculated assuming drained conditions. The main soil variable in the bearing capacity equation is the peak friction angle in the case of sand and the undrained shear strength in the case of clay. The undrained shear strength s_u can be estimated from CPT results through the cone factor N_k, which typically ranges from 9–15 depending on soil type, stress state and history, and stress path (e.g., triaxial compression versus direct simple shear).

Load and resistance factor design (LRFD) procedures for footings in sand and clay were presented. The nominal resistance of the footing is calculated through a nominal value of cone resistance, which is defined as a conservatively assessed mean (CAM) value that is

TABLE 3.5
Resistance factors for footings ($D/B \leq 1$) in sand and clay (modified from Foye et al., 2006b)

	RF [$\beta_T = 3.0$ ($p_{f,T} \approx 10^{-3}$)]	
Footing Type	**Sand**	**Clay**
Strip footing	0.25	0.70
Rectangular footing	0.35	0.75

Note: β_T = target reliability index and $p_{f,T}$ = target probability of failure (a value of 10^{-3} means that one in every 1,000 footings would fail). The resistance factors were developed by Foye et al. (2006b) using reliability analysis and they correspond to the CPT-based footing design methods covered in this chapter. The RF values for rectangular footings may also be used for square and circular footings.

exceeded by 80% of the measured q_c data points. The value of $q_{c,\mathrm{CAM}}$ depends on the standard deviation of q_c, which is estimated from the range of q_c values (i.e., the difference between the maximum and minimum values of q_c) contained within the sample dataset. This difference is related to the number of standard deviations of q_c, which is a function of the sample size. When using LRFD, it is important to note that the resistance factors are always tied to the specific design methods and equations for which they were developed.

Finally, summary tables for the CPT-based footing design methods covered in this chapter have been prepared so that the methods can be easily referred to when needed. The design methods covered in this chapter are not mandatory for design in INDOT contracts, and other CPT-based methods, some of which are summarized in Table 3.7 to Table 3.10, may be used as deemed appropriate for the site and loading conditions under consideration.

TABLE 3.6
Resistance factors for footings in sand and clay (AASHTO, 2020)

Method/Soil/Condition	***RF***
Theoretical method (Munfakh et al., 2001) for footings in clay	0.50
Theoretical method (Munfakh et al., 2001) for footings in sand using CPT	0.50
Semi-empirical methods (Meyerhof, 1956) for footings in sand and clay	0.45
Plate load test	0.55

Note: The resistance factors were developed using both reliability theory and calibration by fitting to working stress design (WSD) (Allen, 2005). In general, WSD safety factors for footing bearing capacity range from 2.5 to 3.0, corresponding to a resistance factor of about 0.55 to 0.45, respectively (AASHTO, 2020). According to AASHTO (2020), calibration by fitting to WSD controlled the selection of the resistance factor when limited statistical data were available.

TABLE 3.7
Methods for estimation of footing settlement in sand

Reference	Total Settlement w	Notes
Lee & Salgado (2002) Lee et al. (2008) Schmertmann (1970) Schmertmann et al. (1978)	$w = C_1 C_2 \left(q_b - \sigma'_{v0}\big\vert_{z_f=0}\right) \sum_{i=1}^{n} \left(\frac{I_{zi}\Delta z_i}{E_i}\right)$ $C_1 = 1 - 0.5\left(\frac{\sigma'_{v0}\vert_{z_f=0}}{q_b - \sigma'_{v0}\vert_{z_f=0}}\right)$; $C_2 = 1 + 0.2\log\left(\frac{t}{0.1 t_R}\right)$ $I_z = \begin{cases} I_{z0} + \frac{z_f}{z_{fp}}\left(I_{zp} - I_{z0}\right) \text{ for } z_f < z_{fp} \\ \frac{z_{f0} - z_f}{z_{f0} - z_{fp}} I_{zp} \text{ for } z_{fp} \le z_f \le z_{f0} \end{cases}$ $\frac{z_{f0}}{B} = 2 + 0.4\left[\min\left(\frac{L}{B}; 6\right) - 1\right]$; $\frac{z_{fp}}{B} = 0.5 + 0.1\left[\min\left(\frac{L}{B}; 6\right) - 1\right]$ $I_{z0} = \min\left[0.1 + 0.0111\left(\frac{L}{B} - 1\right); 0.2\right]$; $I_{zp} = 0.5 + 0.1\sqrt{\frac{q_b - \sigma'_{v0}\vert_{z_f=0}}{\sigma'_{v0}\vert_{z_f=z_{fp}}}}$ $\frac{E}{q_c} = \lambda\left(\frac{w}{L_R}\right)^{-0.285}\left(\frac{B}{L_R}\right)^{0.4}\left(\frac{D_R}{100}\right)^{-0.65}$	Schmertmann's method was modified by Lee and Salgado (2002) and Lee et al. (2008) based on results obtained from nonlinear finite element analyses and cavity expansion analyses (using the program CONPOINT) for isolated and strip footings (B = 1–3 m) on silica sand (D_R = 30%–90%). It accounts for the effects of aging and overconsolidation of sand on the estimation of a representative elastic modulus (from cone resistance) within the zone of influence of the footing. The method captures the nonlinearity of the footing load-settlement curve caused by the degradation of the elastic modulus of sand with increasing footing settlement level. It can be used to calculate from the cone resistance either the load on a given footing or the area of the footing for a given load corresponding to a user-defined tolerable settlement. The value of λ is equal to 0.38 for young NC silica sand, 0.53 for aged NC silica sand, and 0.91 for OC silica sand.
AASHTO (2020) Schmertmann et al. (1978)	$w = C_1 C_2 \left(q_b - \sigma'_{v0}\vert_{z_f=0}\right) \sum_{i=1}^{n} \left(\frac{I_{zi}\Delta z_i}{144 X E_i}\right)$ $E = 0.028 q_c$ X=1.25 for L/B = 1, 1.75 for $L/B \ge 10$, and a linearly-interpolated value for L/B between 1 and 10. The equations for C_1, C_2, and I_{zp} are the same as in the method above.	The equation, originally proposed by Schmertmann et al. (1978), has been rewritten by AASHTO (2020) in a way that requires specific units for certain variables: z in ft; q_c in ksi; and q_b and σ'_{v0} in ksf. The parameters z_{f0}, I_{z0}, z_{fp}, and I_z can be determined from the strain influence diagrams provided in either Schmertmann et al. (1978), Salgado (2008), or AASHTO (2020).
Mayne et al. (2012) Mayne & Dasenbrock (2018) MnDOT (Dagger et al., 2018)	$w = B\left[\frac{1}{h_s}\frac{q_b}{q_{t,net}}\left(\frac{L}{B}\right)^{0.345}\right]^2$ h_s=0.58 for clean sand and $q_{t,\text{net}} = q_t - \sigma_{v0}$; where $q_t = q_c + (1 - a)u_2$ $q_{t,\text{net}}$ is an average net cone resistance measured over a vertical distance of 1.5B below the footing base. For clean sand, the correction of q_c to q_t is negligible and since overburden stresses are small, particularly for shallow foundations, $q_{t,\text{net}} \approx q_t \approx q_c$. For silts that experience drained loading with no excess pore water pressures being developed, h_s = 1.12. For mixed or intermediate soils, h_s can be determined from the soil behavior type index I_c, as illustrated in Dagger et al. (2018).	The method was developed by fitting an equation to a database of footing load test results (122 footings on noncalcareous sands) after normalizing the unit load and settlement of the footing with respect to cone resistance and footing size, respectively. The equation is applicable for L/B = 1–23, D/B = 0–2.2, and q_c = 0.9–21.6 MPa. $(L/B)^{0.345}$ is an influence factor for rectangular footings based on the elasticity theory solution by Giroud (1968).

(Continued)

TABLE 3.7
(Continued)

Reference	Total Settlement w	Notes
Gavin et al. (2009)	$w = w_i + w_c$; where $w_i = \frac{q_b B}{k}$ for the linear stage ($0 \le w_i/B \le w_y/B$), and $w_i = B\left[\frac{q_b}{k\left(\frac{w_y}{B}\right)^{1-n}}\right]^{\frac{1}{n}}$ for the nonlinear stage ($w_y/B < w_i/B < 10\%$ and $w_y/B \ge 0.03\%$) $n = \frac{1.61 - \ln\left[\frac{q_{cb}}{\left(k\frac{w_y}{B}\right)}\right]}{2.30 + \ln\left(\frac{w_y}{B}\right)}$ and $k = \frac{4E_0}{\pi(1-v_0^2)}$ q_{cb} is the average cone resistance over the depth of influence z_{f0} below the footing base, which is given by: $\frac{z_{f0}}{L_R} = \left(\frac{B}{L_R}\right)^{0.75}$	The method approximates the shape of the footing load-settlement curve by an initial linear component (with no modulus degradation) followed by a nonlinear (parabolic) component up to $w_i/B = 10\%$. The value of the exponent n was determined by equating the value of q_b obtained from the equation for the nonlinear stage (at $w_i/B = 10\%$) with a value of $0.2q_{cb}$. The effect of creep is modeled using: $\frac{w_c}{B} = m\ln\left(\frac{t}{t_R}\right)$; where $m = 0.02\left(\frac{q_b}{q_{b,ult}}\right)^2$ w_c = creep component of settlement m = creep coefficient t = time elapsed since the application of the load increment t_R = reference time corresponding to the onset of creep settlement (in the same unit as t) $q_{b,ult}$ = value of q_b at $w_i/B = 10\%$ ($\approx 0.2q_{cb}$)
Lehane (2019) Liu & Lehane (2021)	$q_b = 0.05q_{cb}$ for a short-term relative settlement w/B of 1% $q_b = 0.04q_{cb}$ for a long-term relative settlement w/B of 1% q_{cb} is the average cone resistance over the depth of influence z_{f0} below the footing base, which is given by: $z_{f0}/L_R = (B/L_R)^{0.7}$	The equations are based on centrifuge and field load test results of footings in sand. Short-term and long-term (creep) settlement refer to the settlement observed about 1 day and 30 years, respectively, after the application of the load to the footing.

Note: C_1 and C_2 = depth and time factors, respectively; q_b = unit load on the footing base; $\sigma'_{v0}|_{z_f=0}$ = *in situ* vertical effective stress at the footing base level; I_z = strain influence factor; Δz = thickness of sublayer; E = elastic modulus; n = number of sublayers; t_R = reference time; t = service life of the superstructure (in the same unit as t_R); z_{f0} = influence depth measured from the footing base; z_f = vertical distance from the footing base to the middle of the sublayer; I_{z0} = strain influence factor at the footing base level; I_{zp} = peak strain influence factor; z_{fp} = depth measured from the footing base at which the strain influence factor peaks; $\sigma'_{v0}|_{z_f=z_fp}$ = *in situ* vertical effective stress at the depth corresponding to z_{fp}; q_c = cone resistance; a = cone area ratio (≈ 0.8 for typical CPT probes); u_2 = pore water pressure measured at the shoulder position behind the cone face; L_R = reference length (= 1 m or 3.28 ft); L = footing length; B = width or diameter of the footing; D_R = relative density (expressed as a percentage); E_0 = small-strain Young's modulus [$= 2G_0(1+v_0)$]; G_0 = small-strain shear modulus; v_0 = small-strain Poisson's ratio (= 0.1–0.2); and w_y/B = normalized yield settlement level ($\approx 0.03\%$).

TABLE 3.8
Methods for estimation of bearing capacity of footings in sand

Reference	Bearing Capacity	Notes
Bolton (1986) Lyamin et al. (2007) Loukidis & Salgado (2011) Salgado (2008)	$q_{bL} = (s_q d_q) q_0 N_q + 0.5 (s_\gamma d_\gamma) \gamma B N_\gamma$ $\gamma = \begin{cases} \gamma_b \text{ if } z_w < D \\ \gamma_b + \left(\frac{z_w - D}{B}\right)(\gamma_m - \gamma_b) \text{ if } D \le z_w \le D + B \\ \gamma_m \text{ if } z_w > D + B \end{cases}$ $s_q = 1 + (0.098\phi_p - 1.64)\left(\frac{D}{B}\right)^{0.7 - 0.01\phi_p}\left(\frac{B}{L}\right)^{1 - 0.16\left(\frac{D}{B}\right)}$ $s_\gamma = 1 + (0.0336\phi_p - 1)\frac{B}{L}$ $d_q = 1 + (0.0036\phi_p + 0.393)\left(\frac{D}{B}\right)^{-0.27}$ and $d_\gamma = 1$ $N_q = \frac{1 + \sin\phi_p}{1 - \sin\phi_p} e^{\pi \tan\phi_p}$ and $N_\gamma = (N_q - 0.6)\tan(1.33\phi_p)$ $\phi_p = \phi_c + A_\psi \left\{ \frac{D_R}{100}\left[Q - \ln\left(\frac{100\sigma'_{mp}}{p_A}\right)\right] - R_Q \right\}$ $\sigma'_{mp} = 20 p_A \left(\frac{\gamma B}{p_A}\right)^{0.7}\left(1 - 0.32\frac{B}{L}\right)$ $D_R(\%) = \frac{\ln\left(\frac{q_{c,\mathrm{CAM}}}{p_A}\right) - 0.4947 - 0.1041\phi_c - 0.841\ln\left(\frac{\sigma'_{h0}}{p_A}\right)}{0.0264 - 0.0002\phi_c - 0.0047\ln\left(\frac{\sigma'_{h0}}{p_A}\right)}$	The equations for the shape factors s_q and s_γ and depth factor d_q are based on the results of rigorous lower- and upper-bound limit analyses of circular, rectangular, and strip footings in sand. For a strip footing ($B/L = 0$) placed on the surface ($D/B = 0$) of a sand deposit, the shape and depth factors reduce to a value of 1. For circular footings, the s_q and s_γ equations should be multiplied by an additional term equal to $1 + 0.0025\phi_p$ and $1 + 0.002\phi_p$, respectively. The equation for the bearing capacity factor N_γ fits almost perfectly the exact values of N_γ obtained by Martin (2005) using the method of characteristics or slip-line method, even for very low values of friction angle. The parameter A_ψ is equal to 3 for triaxial conditions (e.g., square and circular footings with $L/B = 1$) and 5 for plane-strain conditions (e.g., elongated rectangular footings with $L/B \ge 7$ and strip footings). For rectangular footings with $1 < L/B < 7$, A_ψ is interpolated between 3 and 5 using $A_\psi = \frac{1}{3}\left(\frac{L}{B} + 8\right)$. The representative mean effective stress σ'_{mp} obtained from the equation is not a mean stress around the footing but rather a value of mean stress that will lead to the value of limit unit resistance q_{bL}. The equation for σ'_{mp} accounts for soil anisotropy, for the difference between the friction and dilatancy angles, and for the evolution of soil properties during loading toward limit bearing capacity failure.
Meyerhof (1956) AASHTO (2020)	$q_{bL}(ksf) = \frac{q_{cb} B}{40}\left(C_{wq}\frac{D}{B} + C_{w\gamma}\right)$ q_{cb} is an average cone resistance measured over a vertical distance of B below the footing base.	This is an empirical method with B and D in the units of ft and q_{cb} in ksf. AASHTO (2020) provides the values of the water table correction factors C_{wq} and $C_{w\gamma}$ in the form of a table. Using those values, we derived the following easy-to-use equations for C_{wq} and $C_{w\gamma}$: $C_{wq} = \min\left[0.5 + 0.5\left(\frac{z_w}{D}\right); 1\right]$ and $C_{w\gamma} = \begin{cases} 0.5 \text{ for } z_w < D \\ \min\left[0.5 + \frac{1}{3}\left(\frac{z_w - D}{B}\right); 1\right] \text{for } z_w \ge D \end{cases}$
Mayne & Woeller (2014) Mayne & Dasenbrock (2018) MnDOT (Dagger et al., 2018)	$q_{b,ult} = h_s q_{t,\mathrm{net}}\left(\frac{w}{B}\right)^{0.5}_{\max}\left(\frac{L}{B}\right)^{-0.345}$ $h_s = 0.58$ and $(w/B)_{\max} = 12\%$ for clean sand $q_{t,\mathrm{net}} = q_t - \sigma_{v0}$; where $q_t = q_c + (1 - a)u_2$ $q_{t,\mathrm{net}}$ is an average net cone resistance measured over a vertical distance of $1.5B$ below the footing base. For clean sand, the correction of q_c to q_t is negligible and since overburden stresses are small, particularly for shallow foundations, $q_{t,\mathrm{net}} \approx q_t \approx q_c$.	The method was developed by fitting an equation to a database of footing load test results (31 footings in 13 silica sands and 11 footings in 4 silt deposits) after normalizing the unit load and settlement of the footing with respect to cone resistance and footing size, respectively. The footing geometries consisted of 29 square, 7 rectangular (nearly square), and 6 circular footings with $B = 0.5$–6.1 m and $D = 0$–2.35 m. The sands were of different age (recent, Holocene, Pleistocene) and geologic origin (alluvial, marine, glaciofluvial, deltaic, aeolian, and residual) with $D_{50} = 0.1$–0.4 mm and $q_c = 0.9$–10.7 MPa. For silts that experience drained loading with no excess pore water pressures being developed, $h_s = 1.12$ and $(w/B)_{\max} = 10\%$. For mixed or intermediate soils, h_s can be determined from the soil behavior type index I_c, and $(w/B)_{\max}$ can be interpolated based on the value of h_s.

(Continued)

TABLE 3.8
(Continued)

Reference	Bearing Capacity	Notes
Lehane (2019)	$q_{b,ult} = \alpha q_{cb}$ α = 0.16 for 10% relative settlement q_{cb} is the average cone resistance over the depth of influence z_{f0} below the footing base, which is given by: $z_{f0}/L_R = (B/L_R)^{0.7}$	Lehane (2013) compiled a database of load test results for 47 footings in sand with B = 0.25–3 m, D = 0.1–1.6 m, and q_{cb} = 3.5–14.5 MPa. The equation for $q_{b,ult}$ predicts 80% of the footing load test results to within 25% of the measured $q_{b,ult}$ values at 10% relative settlement. Liu and Lehane (2021) proposed the following equation to obtain lower-bound estimates of $q_{b,ult}$ corresponding to a long-term (creep) w/B ratio of 10%: $q_{b,ult}$ (long term) = $0.1q_{cb}$
Gavin et al. (2009)	$q_{b,ult} = \alpha q_{cb}$ $\alpha \approx 0.2$ for 10% relative settlement q_{cb} is the average cone resistance over the depth of influence z_{f0} below the footing base, which is given by: $z_{f0}/L_R = (B/L_R)^{0.75}$	The value of α was determined based on the observed load-settlement response (q_b/q_{cb} versus w/B) of model and full-scale, square footings in sand.
Lee & Salgado (2005)	$q_{b,ult} = \alpha q_{cb}$ q_{cb} is an average cone resistance measured over a vertical distance of B below the footing base. The value of α for 20% relative settlement can be obtained from the table provided by Lee and Salgado (2005) as a function of D_R, K_0, and B.	The method was developed based on results obtained from nonlinear finite element analyses and cavity expansion analyses (using the program CONPOINT) for circular footings (B = 1–3 m) on Ottawa sand (D_R = 30%–90%). The equation is also applicable for square footings so long as an equivalent area is considered. However, for footing shapes other than circular or square, introduction of shape factors would be required.

Note: q_{bL} = limit unit bearing capacity (i.e., the unit load at which the footing plunges into the ground), q_0 = surcharge (vertical effective stress) at the footing base level, γ = unit weight of soil below the footing base, B = footing width, s_q and s_γ = shape factors, d_q and d_γ = depth factors, N_q and N_γ = bearing capacity factors, z_w = depth of the groundwater table, γ_m = moist unit weight of soil, γ_b = buoyant unit weight of soil, ϕ_p = peak friction angle, L = footing length, D = depth of embedment of the footing, ϕ_c = critical-state friction angle, D_R = relative density, Q and R_Q = fitting parameters that depend on the intrinsic characteristics of sand (Q = 10 and R_Q = 1 for clean silica sand), $q_{c,\mathrm{CAM}}$ = conservatively assessed mean (CAM) cone resistance at a depth of $B/2$ below the footing base (Eq. 3.37), σ'_{v0} = *in situ* vertical effective stress at a depth of $B/2$ below the footing base, σ'_{h0} = *in situ* horizontal effective stress at a depth of $B/2$ below the footing base (= $K_0\sigma'_{v0}$), K_0 = coefficient of lateral earth pressure at-rest, p_A = reference stress (= 100 kPa or 14.5 psi), $q_{b,ult}$ = ultimate unit bearing capacity (mobilized at a given relative settlement w/B), w = footing settlement, a = cone area ratio ($\approx$ 0.8 for typical CPT probes), u_2 = pore water pressure measured at the shoulder position behind the cone face, and L_R = reference length (= 1 m or 3.28 ft).

TABLE 3.9
Methods for estimation of footing settlement in clay (Foye et al., 2008; Salgado, 2008; Skempton & Bjerrum, 1957)

Immediate Settlement w_i	**Notes**
$w_i = I_q \frac{q_{b,\text{net}} B}{\bar{E}_0}$ $\bar{E}_0 = 2(1+\nu)\bar{G}_0$ $\frac{z_{\bar{G}_0}}{B} = \min\left[1 + 0.111\left(\frac{L}{B} - 1\right); 2\right]$ $\bar{G}_0 = \frac{\sum_{i=1}^{n} G_{0,i}^{\text{avg}} H_i}{\sum_{i=1}^{n} H_i}$ $G_0 = \frac{\gamma_m}{g} V_s^2$ (from seismic cone penetration test data), or $\frac{G_0}{p_A} = C_g \left(\frac{100\sigma'_{m0}}{p_A}\right)^{n_g} R_0^{m_g}$ $\sigma'_{m0} = \frac{1}{k+1}\left(\sigma'_{v0} + k\sigma'_{h0}\right)$ $R_0 = \frac{p'_p}{p'} = \text{OCR}\left(\frac{1 + 2K_{0,\text{NC}}}{1 + 2K_{0,\text{NC}}\sqrt{\text{OCR}}}\right)$	The method was developed based on results obtained from nonlinear finite element analyses of strip, square, and rectangular footings on clay. The influence factor I_q is determined from Figure 3.2 as a function of H/B, $\frac{q_{b,\text{net}}}{\bar{s}_u}$, and footing geometry; where $q_{b,\text{net}} = q_b - \gamma_m D$ and $\bar{s}_u$ = average undrained shear strength over a vertical distance of B below the footing base. The undrained shear strength profile can be obtained from CPT results using $s_u = [(q_t - \sigma_{v0})/N_k]$; where $q_t = q_c + (1-a)u_2$ and N_k = cone factor (≈ 9–15; soft NC clays tend to have N_k values near the low end of this range, while stiff OC clays tend to have N_k values near the high end of this range). The small-strain shear modulus G_0 is averaged over the influence depth $z_{\bar{G}_0}$ below the footing base to obtain $\bar{G}_0$; where $G_{0,i}^{\text{avg}}$ = average small-strain shear modulus of layer i, H_i = thickness of layer i, and n = number of clay layers within the influence depth $z_{\bar{G}_0}$ below the footing base. Parameters C_g, n_g, and m_g depend on the plasticity index PI (Viggiani & Atkinson, 1995): $C_g = 37.9\exp(-0.045\text{PI})$ for PI > 5% $n_g = 0.109\ln(\text{PI}) + 0.4374$ for PI > 5% $m_g = 0.0015\text{PI} + 0.1863$ for PI > 5%
Consolidation Settlement w_c	**Notes**
$w_c = [A + \alpha(1-A)]w_{c1\text{D}}$; where $w_{c1\text{D}} = \sum_{i=1}^{n} \Delta\varepsilon_{z,i}\Delta z_i$ $\Delta\varepsilon_z = \begin{cases} \frac{C_c}{1+e_0}\log\left(\frac{\sigma'_v}{\sigma'_{v0}}\right) \text{ for NC clay} \\ \frac{1}{1+e_0}\left[C_s\log\left(\frac{\sigma'_{vp}}{\sigma'_{v0}}\right) + C_c\log\left(\frac{\sigma'_v}{\sigma'_{vp}}\right)\right] \text{ for OC then NC clay} \\ \frac{C_s}{1+e_0}\log\left(\frac{\sigma'_v}{\sigma'_{v0}}\right) \text{ for OC clay} \end{cases}$ $\sigma'_v = \sigma'_{v0} + \Delta\sigma_v$	The coefficient α is determined from Table 3.2 as a function of H/B and footing geometry. The initial void ratio can be obtained using the relation $e_0 = \text{wc}G_s/S$; where wc = water content, G_s = specific gravity of solids (= 2.60–2.80 for clay), and S = degree of saturation. In the absence of soil samples, the reader may refer to Section 2.3.1 of Volume I for additional information on e_0. In the absence of laboratory consolidation test results, the compression index may be estimated using the correlation of Wroth and Wood (1978): $C_c = G_s\text{PI}(\%)/200$. The swelling index C_s typically ranges from $0.1C_c$ to $0.2C_c$. The vertical stress increment $\Delta\sigma_v$ caused by the footing load can be calculated using the 2-to-1 stress distribution rule.

Note: I_q = influence factor; $q_{b,\text{net}}$ = net unit load on the footing base; q_b = gross unit load on the footing base; H = thickness of the clay layer below the footing base; B = footing width; L = footing length; D = depth of embedment of the footing; q_t = corrected, total cone resistance measured under undrained conditions; q_c = cone resistance; a = cone area ratio (≈ 0.8 for typical CPT probes); u_2 = pore water pressure measured at the shoulder position behind the cone face; σ_{v0} = *in situ* vertical total stress at the depth being considered; $\bar{E}_0$ = representative small-strain Young's modulus; ν = Poisson's ratio (= 0.5 for undrained conditions); γ_m = unit weight of soil; g = acceleration due to gravity (9.81 m/s^2 or 32.17 ft/s^2); V_s = shear wave velocity (refer to Section 2.3.4 of Volume I); p_A = reference stress (= 100 kPa or 14.5 psi); σ'_{m0} = *in situ* mean effective stress at the depth being considered; σ'_{h0} = *in situ* horizontal effective stress at the depth being considered (= $K_0\sigma'_{v0}$); K_0 = coefficient of lateral earth pressure at-rest; k = 1 for plane-strain conditions (e.g., strip footings) and 2 for triaxial conditions (e.g., isolated footings); R_0 = mean stress-based overconsolidation ratio; $K_{0,\text{NC}}$ = coefficient of lateral earth pressure at-rest for normally consolidated soil (≈ 0.5–0.75 for NC clay); OCR = overconsolidation ratio; $w_{c1\text{D}}$ = one-dimensional consolidation settlement; A = Skempton's pore pressure parameter (≈ 0.5–0.75 for NC clay and 0.3–0.5 for OC clay); σ'_{v0} and σ'_v = initial (*in situ*) and current vertical effective stresses, respectively, at the depth being considered; $\Delta\sigma_v$ = vertical stress increment; σ'_{vp} = preconsolidation stress; e_0 = initial void ratio; Δz = thickness of the sublayer; n = number of sublayers; and $\Delta\varepsilon_z$ = vertical compressive strain.

TABLE 3.10
Methods for estimation of bearing capacity of footings in clay

Reference	Bearing Capacity	Notes
Davis & Booker (1973) Salgado et al. (2004) Salgado (2008)	$q_{bL} = F s_{su} d_{su} \left[1 + \frac{\rho B}{4 s_{u0} N_c}\right] s_{u0} N_c + q_0$ $s_{su} = 1 + C_1 \frac{B}{L} \left\{ \frac{2.3}{\exp\left[0.353 \left(\frac{\rho B}{s_{u0}}\right)^{0.509}\right]} - 1.3 \right\} + C_2 \sqrt{\frac{D}{B}}$ $d_{su} = 1 + 0.27 \sqrt{\frac{D}{B}}$	The equation for the shape factor s_{su} is based on a least-squares fit to the values of s_{su} obtained from the computer program ABC (Martin, 2004), which is based on the method of characteristics. The equation for the depth factor d_{su} is based on the results of rigorous lower- and upper-bound limit analyses of footings embedded in clay. The undrained shear strength profile can be obtained from CPT results using $s_u = [(q_{c,\mathrm{CAM}} - \sigma_{v0})/N_k]$; where N_k = cone factor (≈ 9–15; soft NC clays tend to have N_k values near the low end of this range, while stiff OC clays tend to have N_k values near the high end of this range).
Mayne & Woeller (2014) MnDOT (Dagger et al., 2018)	$q_{b,ult} = h_s q_{t,\mathrm{net}} \left(\frac{w}{B}\right)^{0.5}_{\max} \left(\frac{L}{B}\right)^{-0.345}$ h_s = 1.47 and $(w/B)_{\max}$ = 7% for fissured clay h_s = 2.70 and $(w/B)_{\max}$ = 4% for intact clay $q_{t,\mathrm{net}} = q_t - \sigma_{v0}$; where $q_t = q_c + (1 - a)u_2$ $q_{t,\mathrm{net}}$ is an average net cone resistance measured over a vertical distance of 1.5B below the footing base	The method was developed by fitting an equation to a database of footing load test results (12 footings in 6 intact clays and 11 footings in 5 fissured clays) after normalizing the unit load and settlement of the footing with respect to cone resistance and footing size, respectively. The footing geometries consisted of 13 square, 1 rectangular, and 9 circular footings with B = 0.4–5.0 m. For mixed or intermediate soils, h_s can be determined from the soil behavior type index I_c, and $(w/B)_{\max}$ can be interpolated based on the value of h_s.
Lehane (2019)	$q_{bL} \approx 0.45 q_{cb}$ $q_{b,all} \approx 0.25 q_{cb}$ for 1% relative settlement	The method is based on load-settlement data (q_b/q_{cb} versus w/B) compiled from undrained footing load tests in 5 clays. q_{cb} is the average cone resistance (corrected for pore water pressure u_2) over a vertical distance of B below the footing base.

Note: q_{bL} = limit unit bearing capacity (i.e., the unit load at which the footing plunges into the ground), F = correction factor (Figure 3.4), s_{su} = shape factor, d_{su} = depth factor, $q_{c,\mathrm{CAM}}$ = conservatively assessed mean (CAM) cone resistance (corrected for pore water pressure u_2), ρ = rate of increase of undrained shear strength s_u with depth, s_{u0} = undrained shear strength at the footing base level, N_c = bearing capacity factor (= $2 + \pi \approx 5.14$), q_0 = surcharge (vertical total stress) at the footing base level, B = footing width, L = footing length, C_1 and C_2 = coefficients that depend on the aspect ratio B/L of the footing (Table 3.4), $q_{b,ult}$ = ultimate unit bearing capacity (mobilized at a given relative settlement w/B), $q_{b,all}$ = allowable bearing pressure, q_t = corrected, total cone resistance measured under undrained conditions, q_c = cone resistance, a = cone area ratio (≈ 0.8 for typical CPT probes), u_2 = pore water pressure measured at the shoulder position behind the cone face, σ_{v0} = *in situ* vertical total stress at the depth being considered, and L_R = reference length (= 1 m or 3.28 ft).

4. CPT-BASED DESIGN OF PILE FOUNDATIONS

Piles can be classified into three categories based on the changes caused to the state of *in situ* soil during their installation: (1) nondisplacement piles (e.g., drilled shafts), (2) partial-displacement piles (e.g., H-piles and open-ended pipe (OEP) piles), and (3) full-displacement piles (e.g., closed-ended pipe (CEP) piles). A pile derives its load-carrying capacity by two mechanisms: (a) shaft resistance, which is the friction or adhesion along the pile shaft with the surrounding soil, and (b) base resistance, which is the compressive resistance at the contact of the pile base with the underlying soil. Shaft resistance is fully mobilized for small pile head settlements (on the order of 0.25%–1% of the pile diameter), whereas complete mobilization of pile base resistance requires large pile head settlements (on the order of 15%–25% of the pile diameter) (Salgado, 2008).

4.1 Calculation Procedure for Limit Shaft Capacity of Single Piles

The limit shaft capacity Q_{sL} of a single, isolated, axially-loaded pile can be calculated from CPT results by following these steps.

Step 1: Obtain the site stratigraphy, the groundwater table depth, and the unit weight of the soil in each layer of the profile.

a. Establish the site stratigraphy either from the boring log or by using a CPT-based soil behavior type (SBT) chart (refer to Section 2.2.3 of Volume I) or both if possible.
b. Obtain the depth z_w of the groundwater table from either the boring log or the depth profile of u_2 or both if possible, where u_2 = pore water pressure measured at the shoulder position behind the cone face (refer to Volume I).
c. Obtain the unit weight of the soil in each layer of the profile whenever soil samples are recovered during the site investigation. In the absence of soil samples, the reader may refer to Section 2.3.3 of Volume I for correlations between the unit weight and CPT data. In general, the saturated unit weight γ_{sat} of soil typically ranges from 18–21 kN/m^3 (115–135 pcf) for sand, 18.5–22.5 kN/m^3 (118–143 pcf) for silty sand, and 15–18 kN/m^3 (95–115 pcf) for clay (Salgado, 2008).

Step 2: Select the pile type and decide the pile length.

a. Set the pile type and the embedment length L of the pile based on the soil profile at the site.
b. If a competent bearing layer, such as dense sand, stiff clay, or rock, exists at a reasonable depth from the ground surface, embed the pile base in the bearing layer to ensure that the contribution of that layer toward the base resistance can be realized.

Step 3: Classify the soil in each layer that is in contact with the pile as either "sand" or "clay." For mixed or intermediate soils (i.e., soils containing mixtures of sand, silt, and clay), execute the following substeps.

a. Sand-silt, sand-clay or sand-silt-clay mixtures: Classify these soils as "clay" if fines content FC $\geq$ 20% and plasticity index PI $\geq$ 8%, otherwise classify them as "sand" (Carraro et al., 2009; Salgado et al., 2000).
b. Sands containing gravel: If a site contains sand layers with gravel content greater than 20%, use the lower-bound profile of q_c, drawn approximately through the valleys of the actual q_c profile, for estimating the pile capacity (Ganju et al., 2020; Han et al., 2019b, 2020).

Note: In the absence of soil samples, the reader may refer to Section 2.2 of Volume I for estimation of soil behavior type from CPT results.

Step 4: Correct the raw q_c data for the pore water pressure generated during cone penetration using (ASTM, 2012):

$$q_t = q_c + (1-a)u_2 \qquad \text{(Eq. 4.1)}$$

where q_t = corrected, total cone resistance, q_c = measured cone resistance, a = cone area ratio ($\approx$ 0.8 for typical CPT probes), and u_2 = pore water pressure measured at the shoulder position behind the cone face. The pore water pressure correction to the q_c data may be ignored for coarse-grained soils (e.g., sand and gravel) because q_t is approximately equal to q_c in such soils.

Step 5: Using the cone resistance values obtained from step 4, divide the soil layers in contact with the pile shaft into sublayers, as shown in Figure 4.1. The sublayers should satisfy the following criteria.

a. The cone resistance values within each sublayer should be either approximately constant or linear with depth so that a representative cone resistance, indicated by the grey vertical bars in Figure 4.1, can be assigned to each sublayer.
b. The sublayer should consist of the same soil type, i.e., either "sand" or "clay."

Step 6: Calculate the *in situ* vertical effective stress σ'_{v0} at the middle of each sublayer using (Terzaghi, 1943):

$$\sigma'_{v0} = \sigma_{v0} - u_0 \qquad \text{(Eq. 4.2)}$$

where σ_{v0} = *in situ* vertical total stress at the middle of the sublayer, u_0 = hydrostatic pore water pressure at the middle of the sublayer {= max[$\gamma_w(z - z_w)$; 0]}, γ_w = unit weight of water (= 9.81 kN/m^3 or 62.45 pcf), z = depth measured from the ground surface to the middle of the sublayer, and z_w = depth of the groundwater table.

Step 7: Calculate the limit unit shaft resistance of pile segments in contact with "sand" sublayers. Execute the following substeps if the sublayer is "sand," otherwise proceed to step 8.

a. Calculate the *in situ* horizontal effective stress σ'_{h0} (= $K_0\sigma'_{v0}$) at the middle of the sublayer, where K_0 = coefficient of lateral earth pressure at-rest (refer to Appendix B for guidance).
b. Determine the critical-state friction angle ϕ_c of the sublayer through one of the following options.

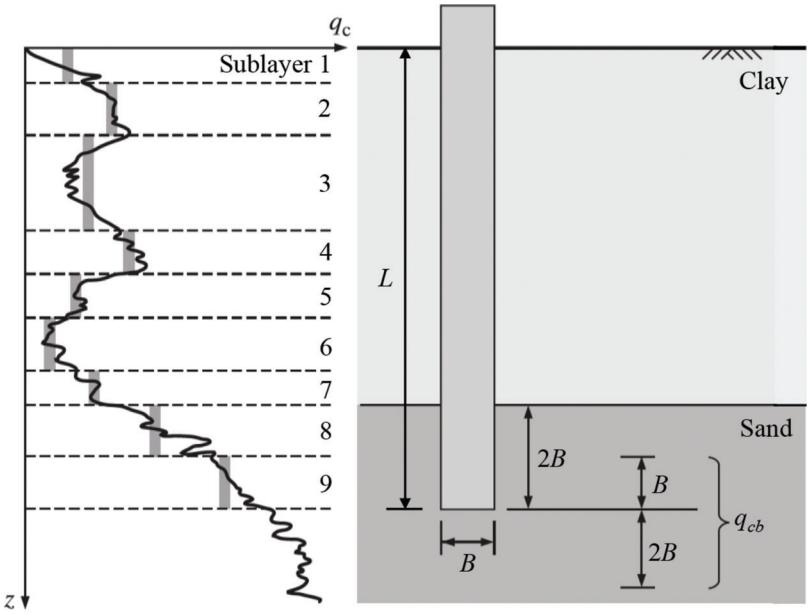

Figure 4.1 CPT-based discretization of soil profile for shaft resistance calculation and averaging of cone resistance for base resistance calculation (after Salgado, 2008).

i. Select a ϕ_c value between 28° and 36° for silica sand; sands with rounded, smooth particles with a poorly-graded particle size distribution have values near the low end of this range, while sands with angular, rough particles with a well-graded particle size distribution have values near the high end of this range (refer to Appendix A for additional information if needed).

ii. If the mean particle size D_{50}, coefficient of uniformity C_U, and particle roundness R of the sublayer are known, estimate the critical-state friction angle using:

$$\phi_c(^\circ) = 28.3\left(\frac{D_{50}}{D_{\text{ref}}}\right)^{\zeta}(C_U)^{2\zeta}(R)^{-3\zeta} \qquad \text{(Eq. 4.3)}$$

where D_{ref} = reference particle size (= 1 mm or 0.04 in.), and ζ = exponent (= 0.045). Equation 4.3 is applicable for poorly-graded, clean silica sands with D_{50} = 0.15–2.68 mm (0.006–0.105 in.), C_U = 1.2–3.1, and R = 0.3–0.8. The data used in the development of this equation along with example calculations can be found in Appendix A.

iii. If direct shear or triaxial compression test results are available, it is recommended that the critical-state friction angle be determined from such test results.

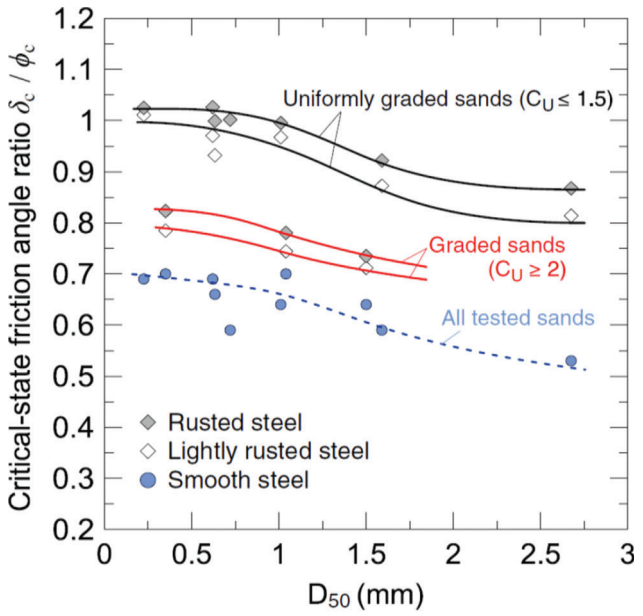

Figure 4.2 Critical-state friction angle ratio δ_c/ϕ_c versus mean particle size D_{50} for silica sands tested against smooth, lightly rusted, and rusted steel surfaces (Han et al., 2018, 2019a). Interpolation can be used for $1.5 < C_U < 2$.

c. Set the critical-state interface friction angle δ_c of the sublayer.

i. For precast concrete piles, set δ_c/ϕ_c = 0.95.
ii. For cast-in-place concrete piles, set δ_c/ϕ_c = 1.00.
iii. For steel piles, set δ_c/ϕ_c = 0.80–0.85. If the D_{50} and C_U values of the sand are known, obtain the value of δ_c/ϕ_c from Figure 4.2.

d. H-piles in "sand": Following the Imperial College pile design method (ICPDM) (Jardine et al., 2005), compute the limit unit shaft resistance q_{sL} of the pile segment in contact with a sand sublayer using:

$$q_{sL} = \left(F_{\text{load}}\sigma'_{rc} + \Delta\sigma'_{rd}\right)\tan\delta_c \qquad \text{(Eq. 4.4)}$$

where F_{load} = factor that accounts for loading direction (= 0.8 for tension and 1.0 for compression), σ'_{rc} = local radial effective stress acting on the pile segment after installation, and $\Delta\sigma'_{rd}$ = increase in local radial effective stress associated with constrained dilation during pile loading:

$$\sigma'_{rc} = 0.029 q_c \left(\frac{\sigma'_{v0}}{p_A}\right)^{0.13} \left(\max\left[\frac{h}{\sqrt{\frac{A_b}{\pi}}}; 8\right]\right)^{-0.38} \quad \text{(Eq. 4.5)}$$

$$\Delta\sigma'_{rd} = 2q_c[0.0203 + 0.00125\eta - 1.216 \times 10^{-6}\eta^2]^{-1} \left(\frac{\Delta r}{\sqrt{\frac{A_b}{\pi}}}\right) \quad \text{(Eq. 4.6)}$$

$$\eta = \frac{\frac{q_c}{p_A}}{\sqrt{\frac{\sigma'_{v0}}{p_A}}} \quad \text{(Eq. 4.7)}$$

where p_A = reference stress (= 100 kPa or 14.5 psi), h = vertical distance from the middle of the sublayer to the pile base, Δr = radial displacement of soil during pile loading (≈ 0.02 mm (0.8 mil) for lightly rusted steel piles), and A_b = area of the pile base (refer to Table 4.2).

e. Drilled shafts, CEP and OEP piles in "sand": Following the Purdue pile design method (PPDM) (Han et al., 2017, 2019b), compute the limit unit shaft resistance q_{sL} of the pile segment in contact with a sand sublayer using:

$$q_{sL} = \begin{cases} F_{\text{load}} K \sigma'_{v0} \tan\delta_c \text{ for CEP piles} \\ K \sigma'_{v0} \tan\delta_c \text{ for drilled shafts} \\ K(1 - 0.66\ \text{PLR})\ \sigma'_{v0} \tan\delta_c \text{ for OEP piles} \end{cases} \quad \text{(Eq. 4.8)}$$

where F_{load} = factor that accounts for loading direction (≈ 0.5–0.6 for tension (Galvis-Castro et al., 2019) and 1.0 for compression), PLR = plug length ratio, and K = lateral earth pressure coefficient:

$$K = \begin{cases} 0.2 + \left[\frac{0.01\left(\frac{q_c}{p_A}\right)}{\sqrt{\frac{\sigma'_{h0}}{p_A}}} - 0.2\right] \exp\left(\frac{-0.14h}{L_R}\right) \\ \text{for CEP and OEP piles} \\ \frac{0.67K_0}{\exp\left[0.3\sqrt{K_0 - 0.4}\right]} \exp\left\{\frac{D_R}{100}\left[1.5 - 0.35\ln\left(\frac{\sigma'_{v0}}{p_A}\right)\right]\right\} \\ \text{for drilled shafts} \end{cases} \quad \text{(Eq. 4.9)}$$

where p_A = reference stress (= 100 kPa or 14.5 psi), h = vertical distance from the middle of the sublayer to the pile base, L_R = reference length (= 1 m or 3.28 ft), and D_R = relative density (expressed as a percentage):

$$D_R(\%) = \frac{\ln\left(\frac{q_c}{p_A}\right) - 0.4947 - 0.1041\phi_c - 0.841\ln\left(\frac{\sigma'_{h0}}{p_A}\right)}{0.0264 - 0.0002\phi_c - 0.0047\ln\left(\frac{\sigma'_{h0}}{p_A}\right)} \quad \text{(Eq. 4.10)}$$

For OEP piles, the plug length ratio (PLR) used in the equation for q_{sL} is that measured at the specific depth where q_{sL} is calculated. If the PLR is not measured, it can be approximated using the same equation (Eq. 4.29) provided for the incremental filling ratio (IFR).

Step 8: Calculate the limit unit shaft resistance of pile segments in contact with "clay" sublayers. Execute the following substeps if the sublayer is "clay," otherwise proceed to step 9.

a. Select a ϕ_c value between 15° and 30° for clay; high-plasticity clays with high smectite and clay contents tend to have values near the low end of this range, while low-plasticity clays with low smectite and clay contents tend to have values near the high end of this range (refer to Table E.1 of Appendix E). If laboratory shear test results (e.g., triaxial compression) are available, it is recommended that the critical-state friction angle be determined from such test results.

b. Select a $\phi_{r,\min}$ value between 5° and 15° for clay (refer to Appendix E for guidance). If ring shear test results are available, it is recommended that the minimum residual-state friction angle be determined from such test results.

c. CEP piles and drilled shafts in "clay" (PPDM).

   i. Determine the undrained shear strength s_u of the sublayer from CPT results using (Salgado, 2008):

$$s_u = \frac{q_t - \sigma_{v0}}{N_k} \quad \text{(Eq. 4.11)}$$

   where q_t = corrected, total cone resistance measured under undrained conditions, σ_{v0} = *in situ* vertical total stress at the middle of the sublayer, and N_k = cone factor (≈ 9–15 as long as the CPT is performed at a penetration rate that is sufficiently high to ensure undrained penetration (refer to Appendix D); soft NC clays tend to have N_k values near the low end of this range, while stiff OC clays tend to have N_k values near the high end of this range) (Bisht et al., 2021; Mayne & Peuchen, 2018; Salgado, 2008, 2013, 2014; Salgado et al., 2004).

   ii. Following the Purdue pile design method (PPDM) (Basu et al., 2009, 2014; Chakraborty et al., 2013), compute the limit unit shaft resistance q_{sL} of the pile segment in contact with a clay sublayer using:

$$q_{sL} = \alpha s_u \quad \text{(Eq. 4.12)}$$

$$\alpha = \begin{cases} A_1 + (1 - A_1)\exp\left[-\left(\frac{\sigma'_{v0}}{p_A}\right)(\phi_c - \phi_{r,\min})^{A_2}\right] \text{ for CEP piles} \\ \left(\frac{s_u}{\sigma'_{v0}}\right)^{-0.05}\left\{A_1 + (1 - A_1)\exp\left[-\left(\frac{\sigma'_{v0}}{p_A}\right)(\phi_c - \phi_{r,\min})^{A_2}\right]\right\} \\ \text{for drilled shafts} \end{cases} \quad \text{(Eq. 4.13)}$$

$$A_1 = \begin{cases} 0.75 \text{ for } \phi_c - \phi_{r,\min} \le 5^\circ \\ 0.43 \text{ for } \phi_c - \phi_{r,\min} \ge 12^\circ \\ \text{for CEP piles} \end{cases} \text{ and } A_1 = \begin{cases} 0.75 \text{ for } \phi_c - \phi_{r,\min} \le 5^\circ \\ 0.40 \text{ for } \phi_c - \phi_{r,\min} \ge 12^\circ \\ \text{for drilled shafts} \end{cases} \quad \text{(Eq. 4.14)}$$

$$A_2 = \begin{cases} 0.55 + 0.43\ln\left(\frac{s_u}{\sigma'_{v0}}\right) \text{ for CEP piles} \\ 0.40 + 0.30\ln\left(\frac{s_u}{\sigma'_{v0}}\right) \text{ for drilled shafts} \end{cases} \quad \text{(Eq. 4.15)}$$

   where p_A = reference stress (= 100 kPa or 14.5 psi). For $5^\circ < \phi_c - \phi_{r,\min} < 12^\circ$, obtain the value of A_1 by interpolation.

d. OEP piles and H-piles in "clay" (ICPDM).

i. Obtain the overconsolidation ratio (OCR) of the sublayer (refer to Appendix B and Section 2.3.7 of Volume I for guidance). If laboratory consolidation test results (e.g., oedometer test or constant rate of strain (CRS) test) are available, it is recommended that the OCR be determined from such test results.

ii. Estimate the sensitivity S_t of the sublayer using:

$$S_t = \frac{s_u}{s_{ur}} \quad \text{(Eq. 4.16)}$$

where s_u = "undisturbed" or *in situ* undrained shear strength of the sublayer (refer to step 8(c)(i)). The remolded undrained shear strength s_{ur} of the sublayer may be estimated using the following approximate correlation (Wroth, 1979):

$$\frac{s_{ur}}{p_A} \approx 0.017 \times 10^{2(1-\mathrm{LI})} \quad \text{(Eq. 4.17)}$$

where p_A = reference stress (= 100 kPa or 14.5 psi), LI = liquidity index (= (wc – PL)/PI), wc = water content, PI = plasticity index (= LL – PL), LL = liquid limit, and PL = plastic limit. In the absence of soil samples, the reader may refer to Sections 2.3.10.5 and 2.3.10.6 of Volume I for additional information on s_{ur} and S_t, respectively.

iii. Estimate the lateral earth pressure coefficient K of the sublayer using (Jardine et al., 2005):

$$K = [2.2 + 0.016\mathrm{OCR} - 0.87 \log S_t]$$
$$\mathrm{OCR}^{0.42}\left(\max\left[\frac{h}{R}; 8\right]\right)^{-0.20} \quad \text{(Eq. 4.18)}$$

$$R = \begin{cases} \sqrt{\dfrac{A_b}{\pi}} & \text{for H-piles} \\ \sqrt{R_o^2 - R_i^2} & \text{for OEP piles} \end{cases} \quad \text{(Eq. 4.19)}$$

where h = vertical distance from the middle of the sublayer to the pile base, R_o = outer radius of OEP pile, R_i = inner radius of OEP pile, and A_b = area of the pile base (Table 4.2).

iv. Determine the residual interface friction angle δ_r of the sublayer through one of the following options.

- Using the values of ϕ_c and $\phi_{r,\min}$ obtained from steps 8(a) and 8(b), respectively, estimate the residual interface friction angle using (Maksimović, 1989; Salgado, 2008):

$$\delta_r \approx \phi_r = \phi_{r,\min} + \frac{\phi_c - \phi_{r,\min}}{1 + \dfrac{\sigma'}{\sigma'_{\mathrm{median}}}} \quad \text{(Eq. 4.20)}$$

where $\sigma'_{\mathrm{median}}$ is the value of σ' at which the friction angle is equal to the average of $\phi_{r,\min}$ and ϕ_c (refer to Figure E.1 in Appendix E), and σ', in the context of pile shaft resistance calculation, is the horizontal effective stress σ'_h on the pile operative at the time of shearing:

$$\sigma'_h = F_{\mathrm{load}} K \sigma'_{v0} \quad \text{(Eq. 4.21)}$$

where F_{load} = 0.8 regardless of the loading direction, and σ'_{v0} = initial (*in situ*) vertical effective stress at the middle of the sublayer. According to the data compiled by Maksimović (1989), the value of $\sigma'_{\mathrm{median}}$ is in the range of 20–150 kPa (3–22 psi) depending on the clay type and mineralogy.

- If results from ring shear interface tests performed for the applicable value of normal effective stress (Ramsey et al., 1998) are available, it is recommended that the residual interface friction angle be determined from such test results.

v. Following the Imperial College pile design method (ICPDM) (Jardine et al., 2005), compute the limit unit shaft resistance q_{sL} of the pile segment in contact with a clay sublayer using:

$$q_{sL} = F_{\mathrm{load}} K \sigma'_{v0} \tan \delta_r \quad \text{(Eq. 4.22)}$$

Step 9: Repeat steps 7 and 8 to obtain the limit unit shaft resistance q_{sL} for each "sand" and "clay" sublayer in contact with the pile shaft.

Step 10: Compute the limit shaft capacity Q_{sL} of the pile using:

$$Q_{sL} = \sum_{i=1}^{n} q_{sLi} A_{si} \quad \text{(Eq. 4.23)}$$

where A_{si} = pile shaft area interfacing with sublayer i (Table 4.1), and n = number of sublayers in contact with the pile shaft.

TABLE 4.1
Expressions for A_{si} for different pile cross-sections

Pile Cross-Section	Pile Shaft Area A_{si}
Circle	$\pi B \Delta z_i$
Square	$4B\Delta z_i$
Rectangle	$2(B_w + B_l)\Delta z_i$
H-section	$2(b_f + d)\Delta z_i$

Note: B = pile diameter (or width in the case of a square pile); B_w and B_l = width and length, respectively, of the cross-section of a rectangular pile (in plan); b_f = width of flange; d = depth of H-section; and Δz_i = thickness of sublayer i.

TABLE 4.2
Expressions for A_b for different pile cross-sections

Pile Cross-Section	Pile Base Area A_b
Circle (CEP)	$\pi B^2/4$
Square	B^2
Rectangle	$B_w B_l$
H-section[1]	$2b_f t_f + (2X_p + t_w)(d - 2t_f)$

Note: B = pile diameter (or width in the case of a square pile); B_w and B_l = width and length, respectively, of the cross-section of a rectangular pile (in plan); b_f = width of flange; d = depth of H-section; t_f = thickness of flange; and t_w = thickness of web.

[1]For H-piles, $X_p = b_f/8$ if $b_f/2 < (\mathrm{d} - 2t_f) < b_f$ and $X_p = b_f^2/[16(\mathrm{d} - 2t_f)]$ if $(d - 2t_f) \geq b_f$ (De Beer et al., 1980; Jardine et al., 2005).

4.2 Calculation Procedure for Ultimate Base Capacity of Single Piles

The ultimate base capacity $Q_{b,ult}$ of a single, isolated, axially-loaded pile can be calculated from CPT results by following these steps.

Step 1: Estimate the average cone resistance q_{cb} at the pile base.

a. Execute the following substeps, depending on the pile design method, to estimate the average cone resistance q_{cb} at the pile base.
   i. For the Purdue pile design method (PPDM), calculate the value of q_{cb} by averaging the cone resistance over a vertical distance within $1B$ above and $2B$ below the pile base.
   ii. For the Imperial College pile design method (ICPDM), calculate the value of q_{cb} by averaging the cone resistance over a vertical distance within $1.5B$ above and $1.5B$ below the pile base.
   Note: If the soil within the averaging zone is clay, use the corrected, total cone resistance q_t (Eq. 4.1), instead of q_c.

b. If the pile base is embedded in a competent (strong) but thin layer (e.g., dense sand or stiff clay) below which there happens to be a weak layer (e.g., loose sand or soft clay), then execute the following substeps to estimate the average cone resistance q_{cb} at the pile base.
   i. From the cone resistance profile, determine the representative cone resistances, $q_{c,w}$ and $q_{c,s}$, of the weak and strong layers, respectively.
   ii. Estimate the sensing distance H_s using (Xu, 2007; Xu & Lehane, 2008):

$$\frac{H_s}{B} = 1.41 - 2.52\ln\left(\frac{q_{c,w}}{q_{c,s}}\right) \qquad \text{(Eq. 4.24)}$$

   The sensing distance is the vertical distance from the layer interface at which the cone resistance first starts changing as the cone moves toward it (Salgado, 2014; Tehrani et al., 2018).
   iii. Determine the vertical distance H from the pile base to the interface between the strong and weak layers.
   iv. If $H \leq H_s$, calculate the value of q_{cb} using the following equations (Xu & Lehane, 2008):

$$\frac{q_{cb}}{q_{c,s}} = \frac{q_{c,w}}{q_{c,s}} + \left(1 - \frac{q_{c,w}}{q_{c,s}}\right) \exp\left\{-\exp\left[A_1 + A_2\left(\frac{H}{B}\right)\right]\right\} \qquad \text{(Eq. 4.25)}$$

$$A_1 = \min\left[-0.22\ln\left(\frac{q_{c,w}}{q_{c,s}}\right) + 0.11; 1.5\right] \qquad \text{(Eq. 4.26)}$$

$$A_2 = \min\left[-0.11\ln\left(\frac{q_{c,w}}{q_{c,s}}\right) - 0.79; -0.2\right] \qquad \text{(Eq. 4.27)}$$

   However, if $H > H_s$, the base resistance of the pile will not be affected much by the presence of the underlying weak layer (Xu, 2007); therefore, we can calculate the value of q_{cb} from step 1(a). Note that piles should be sufficiently embedded in a strong, competent layer, whenever possible, to avoid serviceability issues.

Step 2: Calculate the ultimate unit base resistance $q_{b,ult}$ of the pile.

a. For piles bearing in "sand," calculate the ultimate unit base resistance $q_{b,ult}$ of the pile using (Han et al., 2017, 2019b; Jardine et al., 2005; Lehane et al., 2005):

$$q_{b,ult} = \begin{cases} q_{cb} \text{ for H-piles (ICPDM)} \\ (1 - 0.0058D_R)q_{cb} \text{ for CEP piles (PPDM)} \\ 62p_A\left(\frac{D_R}{100}\right)^{1.83}\left(\frac{\sigma'_{h0}}{p_A}\right)^{0.4} \text{ for drilled shafts (PPDM)} \\ \min\left[0.21(\text{IFR})^{-1.2}q_{cb}; 0.6q_{cb}\right] \text{ for OEP piles (PPDM)} \end{cases} \qquad \text{(Eq. 4.28)}$$

$$\text{IFR} \approx \min\left[1; \left(\frac{B_i}{1.5L_R}\right)^{0.2}\right] \qquad \text{(Eq. 4.29)}$$

   where IFR = incremental filling ratio, B_i = inner diameter of OEP pile, and L_R = reference length (= 1 m or 39.4 in.). Equation 4.29 can be used to estimate the IFR if plug length measurements are unavailable, but if they are available, then average the IFR over the last $3B$ of pile driving. The relative density D_R of the bearing layer can be estimated from CPT results using (Salgado & Prezzi, 2007):

$$D_R(\%) = \frac{\ln\left(\frac{q_{cb}}{p_A}\right) - 0.4947 - 0.1041\phi_c - 0.841\ln\left(\frac{\sigma'_{h0}}{p_A}\right)}{0.0264 - 0.0002\phi_c - 0.0047\ln\left(\frac{\sigma'_{h0}}{p_A}\right)} \qquad \text{(Eq. 4.30)}$$

   where σ'_{h0} = *in situ* horizontal effective stress (= $K_0\sigma'_{v0}$) at a depth of $L + (B/2)$, σ'_{v0} = *in situ* vertical effective stress at a depth of $L + (B/2)$, p_A = reference stress (= 100 kPa or 14.5 psi), ϕ_c = critical-state friction angle (refer to step 7(b) of Section 4.1), and K_0 = coefficient of lateral earth pressure at-rest (refer to Appendix B for guidance).

b. For piles bearing in "clay," calculate the ultimate unit base resistance $q_{b,ult}$ of the pile using (Jardine et al., 2005; Salgado, 2006, 2008):

$$q_{b,ult} = \begin{cases} q_{cb} \text{ for H-piles (ICPDM)} \\ 10s_u \text{ for CEP piles (PPDM)} \\ c_b q_{cb} \text{ for OEP piles (ICPDM)} \\ 9.6s_u \text{ for drilled shafts (PPDM)} \end{cases} \qquad \text{(Eq. 4.31)}$$

   where s_u = undrained shear strength of the bearing layer, estimated from CPT results using (Salgado, 2008):

$$s_u = \frac{q_{cb} - \sigma_{v0}}{N_k} \qquad \text{(Eq. 4.32)}$$

   where σ_{v0} = *in situ* vertical total stress at a depth of $L + (B/2)$, N_k = cone factor [≈ 9–15 as long as the CPT is performed at a penetration rate that is sufficiently high to ensure undrained penetration (refer to Appendix D); soft

NC clays tend to have N_k values near the low end of this range, while stiff OC clays tend to have N_k values near the high end of this range], and c_b = coefficient (= 0.4 if Eq. 4.33 is satisfied and 1.0 otherwise):

$$\frac{B_i}{d_c} + 0.45\frac{q_{cb}}{p_A} < 36 \qquad \text{(Eq. 4.33)}$$

where B_i = inner diameter of OEP pile, d_c = cone diameter, and p_A = reference stress (= 100 kPa or 14.5 psi).

Step 3: Multiply the ultimate unit base resistance $q_{b,ult}$ obtained from step 2 with the pile base area A_b to obtain the ultimate base capacity $Q_{b,ult}$ of the pile:

$$Q_{b,ult} = q_{b,ult} A_b \qquad \text{(Eq. 4.34)}$$

Table 4.2 summarizes the expressions for A_b for different pile cross-sections. For OEP piles bearing in sand (PPDM), calculate the value of A_b using the gross cross-sectional area ($\pi B^2/4$) of the pile base. For OEP piles bearing in clay (ICPDM), calculate the value of A_b using the gross cross-sectional area ($\pi B^2/4$) of the pile base if Eq. 4.33 is satisfied, otherwise use the annulus area of steel.

Step 4: Compute the ultimate load capacity Q_{ult} of the pile using:

$$Q_{ult} = Q_{sL} + Q_{b,ult} \qquad \text{(Eq. 4.35)}$$

where Q_{sL} = limit shaft capacity of the pile, and $Q_{b,ult}$ = ultimate base capacity of the pile. The ultimate pile load capacity Q_{ult} obtained from Eq. 4.35 corresponds to a pile head settlement w equal to 10% of the pile diameter B. For piles of noncircular cross-section (e.g., H-piles), an equivalent pile diameter may be obtained by equating the cross-sectional area of the pile with that of an equivalent circle.

4.3 Load and Resistance Factor Design Procedure for Single Piles

Load and resistance factor design (LRFD) of a single, isolated, axially-loaded pile can be done from CPT results by following these steps.

Step 1: Obtain the nominal dead load DL^n and the nominal live load LL^n on the foundation from the superstructure design.

Step 2: Set the load factors for dead load and live load, LF_{DL} and LF_{LL}, as 1.25 and 1.75, respectively (AASHTO, 2020). These load factors correspond to the Strength I limit state (basic load combination relating to the normal vehicular use of the bridge without wind), as defined by AASHTO (2020). The discussion of other limit states, such as Strength II–V, Extreme Event I and II, Service I–IV, and Fatigue I and II are beyond the scope of the manual—information about these limit states can be found in AASHTO (2020).

Step 3: Obtain the nominal limit shaft capacity Q^n_{sL} and the nominal ultimate base capacity $Q^n_{b,ult}$ of the pile by following the steps outlined in Sections 4.1 and 4.2, respectively.

Step 4: Obtain the resistance factors.

a. *Purdue pile design method (PPDM):* Table 4.3 summarizes the PPDM resistance factors, RF_s and RF_b, for the pile shaft and base resistances, respectively, based on the selected pile type and the predominant soil type at the site. The resistance factors may be adjusted as deemed necessary for sites with high soil variability in the vertical and horizontal directions. Further research is needed to develop PPDM resistance factors for OEP piles in sand.
b. *Imperial College pile design method (ICPDM):* Table 4.4 summarizes the ICPDM resistance factors for driven piles in sand and clay. The resistance factors may be adjusted as deemed necessary for sites with high soil variability in the vertical and horizontal directions.
c. *AASHTO*: Table 4.5 and Table 4.6 summarize the resistance factors advocated by AASHTO (2020) for drilled shafts and driven piles, respectively, in sand and clay.

Step 5: Verify that the following LRFD inequality is satisfied (Basu & Salgado, 2012; Foye et al., 2009):

$$RF_s Q^n_{sL} + RF_b Q^n_{b,ult} \geq LF_{DL} DL^n + LF_{LL} LL^n \qquad \text{(Eq. 4.36)}$$

If Eq. 4.36 is satisfied, the pile design is satisfactory for the selected target probability of failure. Repeat steps 3 to 5 to optimize the design if needed. However, if Eq. 4.36 is not satisfied, return to step 3 and revise the pile geometry.

Note: The following equation may be used, if needed, to obtain a factor of safety (FS) based on the Working Stress Design (WSD) method (Han et al., 2015):

TABLE 4.3
PPDM resistance factors for drilled shafts and CEP piles in sand and clay (modified from Han et al., 2015)

Pile Type	Predominant Soil Type at the Site	$p_{f,T} = 10^{-4}$	
		RF_b	RF_s
Drilled shaft	Sand	0.70	0.65
Drilled shaft	Clay	0.65	0.70
CEP pile	Sand	0.30	0.60
CEP pile	Clay	0.65	0.65

Note: The resistance factors were developed by Han et al. (2015) based on results obtained from Monte Carlo simulations. For layered clay deposits (soft over stiff layers), the values of RF_b and RF_s should be decreased by 25% and 20%, respectively.

Notation: $p_{f,T}$ = target probability of failure (a value of 10^{-4} means that one in every 10,000 piles would fail).

TABLE 4.4
ICPDM resistance factors for driven piles in sand and clay (modified from Kim et al., 2011; Kim & Lee, 2012)

		β_T = 3.5 ($p_{f,T} \approx 2\times10^{-4}$)	
Pile Type	**Predominant Soil Type at the Site**	RF_b	RF_s
CEP and OEP pile	Sand	0.56	0.45
CEP and OEP pile	Clay	0.58	0.58

Note: The resistance factors were developed by Kim et al. (2011) and Kim and Lee (2012) based on results obtained from reliability analyses performed using the first-order reliability method (FORM). The RF values listed in Table 4.4 are the lowest among the values reported by Kim et al. (2011) and Kim and Lee (2012) for different combinations of $\frac{DL^n}{LL^n}$ and $\frac{Q^n_{b,ult}}{Q^n_{sL}}$. These values may also be used for H-piles as the design equations are similar to those for CEP and OEP piles.

Notation: β_T = target reliability index and $p_{f,T}$ = target probability of failure (a value of 2×10^{-4} means that one in every 5,000 piles would fail).

TABLE 4.5
Resistance factors for drilled shafts in sand and clay (AASHTO, 2020)

		Resistance Factor	
Method/Condition	**Predominant Soil Type at the Site**	RF_b	RF_s
α-method (Brown et al., 2010)	Clay	0.40	0.45
β-method (Brown et al., 2010)	Sand	0.50	0.55
Static load test (compression)	Sand/Clay	0.70	0.70

Note: The resistance factors were developed based on statistical analysis of load test data combined with reliability theory (Paikowsky et al., 2004), fitting to allowable stress design (ASD), or both (Allen, 2005). For piles subjected to uplift (tension), the resistance factor RF is equal to 0.35 for the α-method, 0.45 for the β-method, and 0.60 for pile design based on static load test results.

TABLE 4.6
Resistance factors for driven piles in sand and clay (AASHTO, 2020)

Method/Condition	**Predominant Soil Type at the Site**	**Resistance Factor RF**
CPT method (Nottingham & Schmertmann, 1975)	Sand/Clay	0.50
Static load test (compression)	Sand/Clay	0.75–0.80[1]

Note: The resistance factors were developed based on statistical analysis of load test results combined with reliability theory (Paikowsky et al., 2004), fitting to allowable stress design (ASD), or both (Allen, 2005). For piles subjected to uplift (tension), the resistance factor RF is equal to 0.40 for the CPT method and 0.60 for pile design based on static load test results. Since a single value for the resistance factor was provided by AASHTO (2020), this value may be used for both the shaft and base components (i.e., $RF = RF_s = RF_b$).

[1]Additional information can be found in AASHTO (2020), including resistance factors for conditions when dynamic tests are performed on the piles.

$$FS = \frac{C^n}{D^n} = \frac{Q^n_{sL} + Q^n_{b,ult}}{DL^n + LL^n} \qquad \text{(Eq. 4.37)}$$

where C^n = nominal capacity, and D^n = nominal demand.

4.4 Load and Resistance Factor Design Procedure for Pile Groups

When the axial load from the superstructure exceeds the resistance offered by a single pile, as is the case for foundations of skyscrapers, bridge piers and abutments, power plants, and offshore oil platforms, it becomes necessary to install multiple piles as a group to support the load. Load and resistance factor design (LRFD) of axially-loaded pile groups can be done from CPT results by following these steps.

Step 1: Obtain the nominal dead load DL^n and the nominal live load LL^n on the foundation from the superstructure design.

Step 2: Set the load factors for dead load and live load, LF_{DL} and LF_{LL}, as 1.25 and 1.75, respectively (AASHTO, 2020). These load factors correspond to the Strength I limit state (basic load combination relating to the normal vehicular use of the bridge without wind), as defined by AASHTO (2020). The discussion of other

limit states, such as Strength II–V, Extreme Event I and II, Service I–IV, and Fatigue I and II are beyond the scope of the manual—information about these limit states can be found in AASHTO (2020).

Step 3: Obtain the nominal limit shaft capacity $Q^n_{sL,i}$ and the nominal ultimate base capacity $Q^n_{b,ult,i}$ of a single pile in the group by following the steps outlined in Sections 4.1 and 4.2, respectively.

Step 4: Set the pile center-to-center spacing s_{cc} and the configuration (or layout) of the pile group.

Step 5: LRFD of pile groups in "sand."

Execute the following substeps if the pile group is installed in a soil profile that consists predominantly of "sand," otherwise proceed to step 6.

a. Determine the average (representative) relative density of the sand layer(s) crossed by the pile group (using Eq. 4.10) and the relative density of the bearing layer in which the pile group is embedded (using Eq. 4.30).
b. For small drilled shaft groups (e.g., 1×2, 1×3, and 2×2 groups) (Figure 4.3a), the efficiencies $\eta_{s,i}$ and $\eta_{b,i}$ for the shaft and base resistances, respectively, are equal to 1.0 for a pile head settlement of 30 mm (1.2 in.). For a large, drilled shaft group (e.g., 4×4 group) (Figure 4.3b), refer to Table 4.7 for the values of $\eta_{s,i}$ and $\eta_{b,i}$. Further research is needed to develop rigorous values of $\eta_{s,i}$ and $\eta_{b,i}$ for driven pile groups in sand; in the meantime, the same values for drilled shaft groups may also be used for driven pile groups if deemed appropriate. Alternatively, Table 4.8 and Table 4.9 summarize the efficiencies advocated by AASHTO (2020) for drilled shaft groups and driven pile groups, respectively, in sand.
c. Obtain the resistance factors, RF_s and RF_b, for the pile shaft and base resistances, respectively, from step 4 of Section 4.3.
d. Verify that the following LRFD inequality is satisfied (Han et al., 2015):

$$RF_s\left[\sum_{i=1}^{n_p}\eta_{s,i}Q^n_{sL,i}\right]+RF_b\left[\sum_{i=1}^{n_p}\eta_{b,i}Q^n_{b,ult,i}\right] \geq LF_{DL}DL^n+LF_{LL}LL^n \qquad \text{(Eq. 4.38)}$$

where n_p = number of piles in the group. If Eq. 4.38 is satisfied, the pile group design is satisfactory for the selected target probability of failure. Repeat steps 3 to 5 to optimize the design if needed. However, if Eq. 4.38 is not satisfied, return to step 3 and revise the design.

Note: The following equation may be used, if needed, to obtain a factor of safety (FS) based on the Working Stress Design (WSD) method:

$$FS=\frac{C^n}{D^n}=\frac{\sum_{i=1}^{n_p}\eta_{s,i}Q^n_{sL,i}+\sum_{i=1}^{n_p}\eta_{b,i}Q^n_{b,ult,i}}{DL^n+LL^n} \qquad \text{(Eq. 4.39)}$$

where C^n = nominal capacity, and D^n = nominal demand.

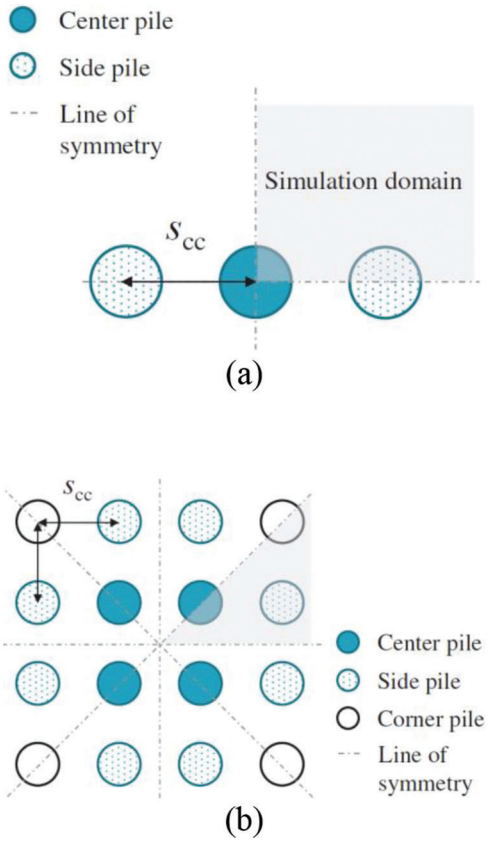

Figure 4.3 Layout of (a) small (1×3) pile group and (b) large (4×4) pile group (Han et al., 2015, 2019c).

Step 6: LRFD of pile groups in "clay."

Execute the following substeps if the pile group is installed in a soil profile that consists predominantly of "clay."

a. Individual pile failure ultimate limit state.
   i. For small drilled shaft groups (e.g., 1×2, 1×3, and 2×2 groups) (Figure 4.3a), the efficiencies $\eta_{s,i}$ and $\eta_{b,i}$ for the shaft and base resistances, respectively, are equal to 1.0 for a pile head settlement of 30 mm (1.2 in.). For a large drilled shaft group (e.g., 4×4 group) (Figure 4.3b), refer to Table 4.10 for the values of $\eta_{s,i}$ and $\eta_{b,i}$. Further research is needed to develop rigorous values of $\eta_{s,i}$ and $\eta_{b,i}$ for driven pile groups in clay; in the meantime, the same values for drilled shaft groups may also be used for driven pile groups if deemed appropriate. Alternatively, Table 4.11 summarizes the efficiencies advocated by AASHTO (2020) for drilled shaft groups and driven pile groups in clay.
   ii. Obtain the resistance factors, RF_s and RF_b, for the pile shaft and base resistances, respectively, from step 4 of Section 4.3.
   iii. Verify that the following LRFD inequality is satisfied (Han et al., 2015):

TABLE 4.7
Shaft and base efficiencies for a large (4 × 4) drilled shaft group in sand for $s_{cc} = 2B$ (Han et al., 2015; Han, Salgado, 2019)

		Relative Density D_R = 50%			Relative Density D_R = 80%		
Pile Head Settlement w	**Efficiency**	**Center Pile**	**Side Pile**	**Corner Pile**	**Center Pile**	**Side Pile**	**Corner Pile**
30 mm (1.2 in.)	$\eta_{b,i}$	1.14	0.90	0.80	0.93	0.78	0.74
	$\eta_{s,i}$	0.63	1.01	1.06	0.94	1.25	1.01
50 mm (2.0 in.)	$\eta_{b,i}$	1.28	0.96	0.81	1.16	0.86	0.77
	$\eta_{s,i}$	0.80	1.19	1.16	1.23	1.51	1.04

Note: The value of 50 mm (2 in.) for the pile head settlement is based on the tolerable settlement criteria for frame structures and bridges. Settlements beyond 50 mm (2 in.) would lead to serviceability issues, while those approaching 100 mm (4 in.) would lead to structural damage (Bozozuk, 1978). For intermediate values of w and D_R, the values of $\eta_{s,i}$ and $\eta_{b,i}$ can be obtained by linear interpolation.

Notation: B = pile diameter, s_{cc} = pile center-to-center spacing, $\eta_{s,i}$ = efficiency for shaft resistance of the i^{th} pile in the group, and $\eta_{b,i}$ = efficiency for base resistance of the i^{th} pile in the group.

TABLE 4.8
Efficiencies for small and large drilled shaft groups in sand (AASHTO, 2020)

Group Configuration	s_{cc}	**Special Conditions**	η_i
Single row (e.g., 1 × 2 and 1 × 3 groups)	$2B$	—	0.90
	$\geq 3B$	—	1.00
Multiple row (e.g., 2 × 2 and 4 × 4 groups)	$2.5B$	—	0.67
	$3B$	—	0.80
	$\geq 4B$	—	1.00
Single and multiple rows	$\geq 2B$	Pile cap is in firm contact with medium dense or denser soil, and no scour is expected below the cap	1.00
Single and multiple rows	$\geq 2B$	Pressure grouting is used along the sides of the pile to restore lateral stress losses caused by pile installation, and the pile base is pressure grouted	1.00

Note: For intermediate values of s_{cc}, the value of η_i can be obtained by linear interpolation. For pile groups bearing on a strong soil layer of limited thickness overlying a weak deposit, the nominal resistance of the pile group is taken as the lesser of (a) the sum of the individual nominal resistances of each pile in the group, and (b) the nominal resistance of the pile group against block failure, with consideration to the punching of the pile group into the underlying weak layer (AASHTO, 2020).

Notation: B = pile diameter, s_{cc} = pile center-to-center spacing, and η_i = efficiency of the i^{th} pile in the group (= $\eta_{s,i} = \eta_{b,i}$).

TABLE 4.9
Efficiencies for small and large driven pile groups in sand (AASHTO, 2020)

Group configuration	s_{cc}	**Condition**	η_i
Single and multiple rows	$\geq 2.5B$	No weak layer is present below the pile base	1.00

Note: The value of η_i is equal to 1 regardless of whether the pile cap is or is not in contact with the ground. For pile groups bearing on a strong soil layer of limited thickness overlying a weak deposit, the nominal resistance of the pile group is taken as the lesser of (a) the sum of the individual nominal resistances of each pile in the group, and (b) the nominal resistance of the pile group against block failure, with consideration to the punching of the pile group into the underlying weak layer (AASHTO, 2020).

Notation: B = pile diameter, s_{cc} = pile center-to-center spacing, and η_i = efficiency of the i^{th} pile in the group (= $\eta_{s,i} = \eta_{b,i}$).

$$RF_s\left[\sum_{i=1}^{n_p}\eta_{s,i}Q_{sL,i}\right]+RF_b\left[\sum_{i=1}^{n_p}\eta_{b,i}Q_{b,ult,i}\right] \geq LF_{DL}DL^n+LF_{LL}LL^n \quad \text{(Eq. 4.40)}$$

where n_p = number of piles in the group.
Note: Equation 4.39 may be used, if needed, to obtain a factor of safety (FS) based on the Working Stress Design (WSD) method.

b. Block failure ultimate limit state.

i. Determine the length L_g and width B_g of the pile group, as shown in Figure 4.4.
ii. Set the limit unit shaft resistance q_{sL} of the pile group is equal to $\bar{s}_u$, the average (representative) undrained shear strength along the pile length. The undrained shear strength profile along the pile shaft can be obtained from CPT data using Eq. 4.11.

iii. Estimate the limit unit base resistance q_{bL} of the pile group using (Salgado, 2008; Skempton, 1951):

$$q_{bL} = 5s_u\left(1+0.2\frac{B_g}{L_g}\right)\left(1+\frac{L}{12B_g}\right) \qquad \text{(Eq. 4.41)}$$

where s_u = undrained shear strength at a depth of $L + (B_g/3)$, and L = pile embedment length.

iv. Set both the shaft and base resistance factors, RF_s and RF_b, as equal to 0.60 for driven pile groups and 0.55 for drilled shaft groups (AASHTO, 2020).

v. Verify that the following LRFD inequality is satisfied:

$$RF_s\left[2\left(B_g+L_g\right)Lq_{sL}\right]+RF_b\left[B_gL_gq_{bL}\right] \geq LF_{DL}DL^n+LF_{LL}LL^n \qquad \text{(Eq. 4.42)}$$

Note: The following equation may be used, if needed, to obtain a factor of safety (FS) based on the Working Stress Design (WSD) method.

$$FS=\frac{C^n}{D^n}=\frac{2\left(B_g+L_g\right)Lq_{sL}+B_gL_gq_{bL}}{DL^n+LL^n} \qquad \text{(Eq. 4.43)}$$

where C^n = nominal capacity, and D^n = nominal demand.

TABLE 4.10
Shaft and base efficiencies for a large (4 × 4) drilled shaft group in NC clay for s_{cc} = 2B (Han et al., 2015)

Pile Head Settlement w	Efficiency	Center Pile	Side Pile	Corner Pile
30 mm (1.2 in.)	$\eta_{b,i}$	0.96	1.01	1.00
	$\eta_{s,i}$	0.38	0.77	0.98
50 mm (2.0 in.)	$\eta_{b,i}$	1.02	1.06	1.03
	$\eta_{s,i}$	0.46	0.85	1.03

Note: The value of 50 mm (2 in.) for the pile head settlement is based on the tolerable settlement criteria for frame structures and bridges. Settlements beyond 50 mm (2 in.) would lead to serviceability issues, while those approaching 100 mm (4 in.) would lead to structural damage (Bozozuk, 1978). For intermediate values of w, the values of $\eta_{s,i}$ and $\eta_{b,i}$ can be obtained by linear interpolation. Further research is needed to develop rigorous values of $\eta_{s,i}$ and $\eta_{b,i}$ for pile groups in OC clay, but until then, the same values for NC clay may also be used for OC clay.

Notation: B = pile diameter, s_{cc} = pile center-to-center spacing, $\eta_{s,i}$ = efficiency for shaft resistance of the i^{th} pile in the group, and $\eta_{b,i}$ = efficiency for base resistance of the i^{th} pile in the group.

TABLE 4.11
Efficiencies for small and large drilled shaft and driven pile groups in clay (AASHTO, 2020)

Group Configuration	s_{cc}	Condition	η_i
Single and multiple rows	2.5B	Pile cap is not in firm contact with the ground and the soil at the ground surface is soft	0.65
Single and multiple rows	≥ 6B	Same as above	1.00

Note: For intermediate values of s_{cc}, the value of η_i can be obtained by linear interpolation. If the pile cap is not in firm contact with the ground but the soil is stiff, η_i = 1.0. If the pile cap is in firm contact with the ground, η_i = 1.0.

Notation: B = pile diameter, s_{cc} = pile center-to-center spacing, and η_i = efficiency of the i^{th} pile in the group (= $\eta_{s,i}$ = $\eta_{b,i}$).

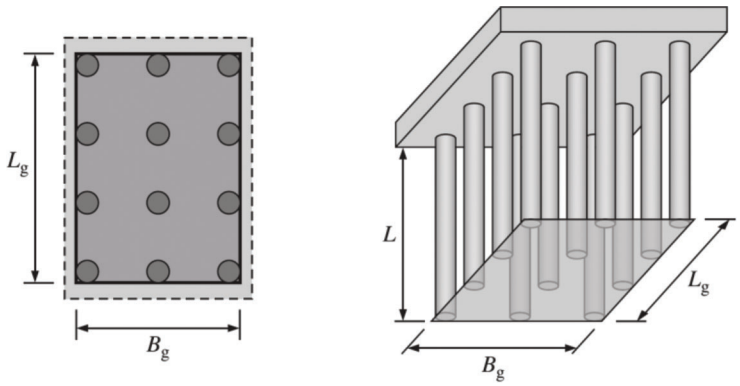

Figure 4.4 Schematic of a 3 × 4 pile group with parameters L_g, B_g, and L in (a) plan view and (b) 3D view (Salgado, 2008).

c. If Eqs. 4.40 and 4.42 are satisfied, the pile group design is satisfactory with respect to the ultimate limit states of individual pile failure and block failure, respectively. Repeat steps 3, 4 and 6 to optimize the design if needed. However, if either Eq. 4.40 or Eq. 4.42 is not satisfied, return to step 3 and revise the design.

4.5 Chapter Summary

In this chapter, detailed, step-by-step procedures for computing the limit shaft capacity Q_{sL} and the ultimate base capacity $Q_{b,ult}$ of a single, isolated, axially-loaded pile from CPT results in sand (silica sand) and clay were presented. The limit unit shaft resistance q_{sL} and the ultimate unit base resistance $q_{b,ult}$ of a pile designed using the PPDM depend on the critical-state friction angle ϕ_c and relative density D_R in the case of sands, and the undrained shear strength s_u and friction angles, ϕ_c and $\phi_{r,\min}$, in the case of clays; $\phi_{r,\min}$ = minimum residual-state friction angle. The undrained shear strength s_u can be estimated from CPT results through the cone factor N_k, which typically ranges from 9–15 depending on soil type, stress state and history, and stress path (e.g., triaxial compression versus direct simple shear). In addition to some of these variables, the ICPDM relies on other key parameters, such as residual interface friction angle δ_r, sensitivity S_t, and overconsolidation ratio OCR in the case of clays. For base resistance calculations, both the PPDM and the ICPDM average the cone resistance q_c around the pile base according to some formula and relate the ultimate unit base resistance $q_{b,ult}$ of the pile to the representative (average) cone resistance q_{cb}, which serves as a proxy for the limit unit base resistance q_{bL} of the pile.

Guidelines for piles installed in mixed or intermediate soils, such as sand-silt-clay mixtures and gravelly sand, were provided. In addition, load and resistance factor design (LRFD) procedures for single piles and pile groups were presented, and potential areas for future research have been indicated. When using LRFD, it is important to note that the resistance factors are always tied to the specific design methods and equations for which they were developed.

Summary tables for the CPT-based pile design methods covered in this chapter have been prepared so that the methods can be easily referred to when needed. The design methods covered in this chapter are not mandatory for design in INDOT contracts, and other CPT-based methods, some of which are summarized in Table 4.12 to Table 4.25, may be used as deemed appropriate for the site and loading conditions under consideration. Pile design methods that rely solely on the measured values of cone resistance to the exclusion of other information that may be available at design time will not be as accurate as methods that consider all the available information. In this sense, they are, in fact, less conservative. The inclusion of key intrinsic and state variables known to control the mechanical response of soil during shearing, such as relative density and stress state in the case of sands, and undrained shear strength, critical-state friction angle, and minimum residual-state friction angle in the case of clays, improves the capability of a CPT-based design method to predict the ultimate load capacity of a pile. These variables can be determined using the guidance and relationships provided in the manual. Also, pile design methods that consider the effect of soil plugging during the installation of open-ended pipe piles are expected to provide more realistic estimates of pile capacity than methods that do not consider this effect. The capacities mobilized by a closed-ended pipe pile and an open-ended pipe pile are different (Han et al., 2019b; Paik et al., 2003), and pile design methods that do not differentiate between these pile types do not consider installation effects on pile capacity.

Shaft degradation is a process by which the unit shaft resistance at a given depth along the pile decreases as the pile is driven down further from that depth (Lehane et al., 1993; Randolph, 2003; Randolph et al., 1994; White & Lehane, 2004). This degradation, however, is not properly accounted for in the purely direct CPT-based pile design methods (i.e., methods that rely only on CPT data to the exclusion of other variables). Furthermore, because of greater variability in sleeve resistance measurements (among other issues), f_s is not a reliable parameter for use in foundation design (Schneider et al., 2008), which is why the modern pile design methods (e.g., PPDM, ICPDM, UWAPDM, and UPDM) rely instead on the cone resistance q_c, among other variables, and contain a shaft resistance degradation term in the design equations. The PPDM, ICPDM, UWAPDM, and UPDM are based on the 10% relative settlement criterion, i.e., the methods predict the ultimate load capacity of the pile corresponding to a pile displacement equal to 10% of the pile diameter (except for certain cases, such as floating piles in soft clay, where the limit load is achieved after relatively small settlements (Basu & Salgado, 2014)).

A final note is in order regarding the use of the cone resistance to obtain other soil parameters of interest. The cone resistance is a single measurement, but it depends on more than one variable. For example, in simple terms, the cone resistance q_c in sand depends on two state variables—relative density D_R and *in situ* horizontal effective stress σ'_{h0} [$= f(K_0, \text{OCR})$]—and one intrinsic variable—critical-state friction angle ϕ_c. The cone resistance can be used to estimate D_R if the other two variables (σ'_{h0} and ϕ_c) are known, but it cannot be used to determine all three variables. This needs to be kept in mind as engineers may be tempted to obtain the values of more than one variable from q_c, which is a single measurement. Interpreting CPT results can be likened to solving a system of equations: the number of equations must be equal to the number of unknowns to be determined. If only one measurement is available, we cannot determine multiple independent variables from that one measurement.

TABLE 4.12
PPDM equations for the unit shaft and base resistances for nondisplacement piles (drilled shafts) in sand and clay

Soil Type and References	Limit Unit Shaft Resistance q_{sL}	Ultimate Unit Base Resistance $q_{b,ult}$
Sand (Han et al., 2017)	$q_{sL} = K\sigma'_{v0}\tan\delta_c$ $\frac{K}{K_0} = \frac{0.67}{\exp\left[0.3\sqrt{K_0 - 0.4}\right]}\exp\left\{\frac{D_R}{100}\left[1.5 - 0.35\ln\left(\frac{\sigma'_{v0}}{p_A}\right)\right]\right\}$	$q_{b,ult} = 62p_A\left(\frac{D_R}{100}\right)^{1.83}\left(\frac{\sigma'_{h0}}{p_A}\right)^{0.4}$
Clay (Chakraborty et al., 2013; Salgado, 2006)	$q_{sL} = \alpha s_u$ $\alpha = \left(\frac{s_u}{\sigma'_{v0}}\right)^{-0.05}\left\{A_1 + (1 - A_1)\exp\left[-\left(\frac{\sigma'_{v0}}{p_A}\right)(\phi_c - \phi_{r,\min})^{A_2}\right]\right\}$ A_1 = 0.75 for $\phi_c - \phi_{r,\min} \le 5^\circ$, 0.40 for $\phi_c - \phi_{r,\min} \ge 12^\circ$ and a linearly interpolated value for $5^\circ < \phi_c - \phi_{r,\min} < 12^\circ$ $A_2 = 0.4 + 0.3\ln\left(\frac{s_u}{\sigma'_{v0}}\right)$	$q_{b,ult} = 9.6s_u$

Note: The method predicts the ultimate load capacity Q_{ult} of the pile corresponding to a pile head settlement w equal to 10% of the pile diameter B. The equation for the ultimate unit base resistance $q_{b,ult}$ of drilled shafts in sand is applicable for $L/B < 50$. The method is intended to estimate the shaft resistance in clay after dissipation of the excess pore water pressure generated during pile installation. The relative density D_R and undrained shear strength s_u can be estimated from CPT results using the equations provided in the chapter.

Notation: PPDM = Purdue pile design method, p_A = reference stress (= 100 kPa or 14.5 psi), K = coefficient of lateral earth pressure, σ'_{v0} = *in situ* vertical effective stress at the depth being considered, δ_c = critical-state interface friction angle (which, for drilled shafts, is equal to the internal critical-state friction angle ϕ_c of the soil), σ'_{h0} = *in situ* horizontal effective stress at the depth being considered (= $K_0\sigma'_{v0}$), K_0 = coefficient of lateral earth pressure at-rest (Appendix B), and $\phi_{r,\min}$ = minimum residual-state friction angle (Appendix E).

TABLE 4.13
MnDOT equations (Modified UniCone method) for the unit shaft and base resistances for nondisplacement piles (drilled shafts) in sand and clay (Dagger et al., 2018)

Soil Type	Limit Unit Shaft Resistance q_{sL}	Ultimate Unit Base Resistance $q_{b,ult}$
Sand	$q_{sL} = q_E\theta_{pt}\theta_{tc}\theta_{rate}\left(10^{0.732I_c - 3.605}\right)$ $I_c = \sqrt{(3.47 - \log Q_{tn})^2 + (1.22 + \log F_r)^2}$ $Q_{tn} = \left(\frac{q_t - \sigma_{v0}}{p_A}\right)\left(\frac{p_A}{\sigma'_{v0}}\right)^n$ and $F_r = \frac{f_s}{q_t - \sigma_{v0}} \times 100\%$ $n = \min\left[0.381I_c + 0.05\left(\frac{\sigma'_{v0}}{p_A}\right) - 0.15; 1\right]$	$q_{b,ult} = q_{cb}\left(10^{0.325I_c - 1.218}\right)$ I_c is calculated using the same set of equations as those in the estimation of q_{sL}.
Clay	Use the same equation as for sand	Use the same equation as for sand

Note: The method predicts the maximum load capacity $Q_{\max}$ of the pile (i.e., the maximum load applied on the piles considered in the database). For most (> 90%) of the pile load tests considered in the database, the value of $Q_{\max}$ was nearly equal to the value of Q_{ult} based on the 10% relative settlement criterion (i.e., the load corresponding to a pile head settlement w equal to 10% of the pile diameter B). The following adjustment was proposed to estimate Q_{ult} from $Q_{\max}$: $Q_{ult} = 0.986Q_{\max}$ (Niazi & Mayne, 2016).

The value of the exponent n is approximately equal to 1 for clay, 0.75 for silt, and 0.5 for sand. For mixed or intermediate soils, iterative calculations are needed to determine the value of I_c. For the first iteration, the method recommends the use of $n = 1$ to obtain an initial value of I_c at the depth being considered. In the next iteration, this initial value of I_c is used to update the value of n, which is then used to obtain a new value of I_c. The process is repeated until the value of I_c converges, which is generally after the third cycle. Additional information on sensitive clays can be found in Niazi and Mayne (2016).

The representative cone resistance q_{cb} for base resistance calculation is q_E averaged over a vertical distance of B below the pile base (Dagger et al., 2018).

Notation: MnDOT = Minnesota Department of Transportation, B = pile diameter, q_E = effective cone resistance (= $q_t - u_2$); q_t = corrected, total cone resistance; f_s = sleeve resistance; u_2 = pore water pressure measured at the shoulder position behind the cone face; I_c = soil behavior type index; Q_{tn} = normalized cone resistance; F_r = normalized friction ratio; σ_{v0} and σ'_{v0} = *in situ* vertical total and effective stresses, respectively, at the depth being considered; p_A = reference stress (= 100 kPa or 14.5 psi); θ_{pt} = coefficient for pile type (= 0.84 for drilled shafts); θ_{tc} = coefficient for loading direction (= 0.85 for tension and 1.11 for compression); and θ_{rate} = coefficient for loading procedure (= 1.09 for constant rate of penetration test and 0.97 for maintained load test).

4.5.2 Design Methods for Displacement Piles in Sandy Soil

TABLE 4.14
PPDM equations for the unit shaft and base resistances for displacement piles driven in sand (modified from Han et al., 2019b)

Pile Type	Limit Unit Shaft Resistance q_{sL}	Ultimate Unit Base Resistance $q_{b,ult}$
Closed-ended pipe pile	$q_{sL} = F_{\text{load}} K \sigma'_{v0} \tan \delta_c$ $K = K_{\min} + (K_{\max} - K_{\min}) \exp\left(\frac{-\alpha h}{L_R}\right)$ $K_{\max} = \frac{0.01(q_c/p_A)}{\sqrt{\sigma'_{h0}/p_A}}$ $K_{\min}$=0.2 and α=0.14	$q_{b,ult}$=(1–0.0058D_R)q_{cb}
Open-ended pipe pile	$q_{sL} = K(1-0.66\text{PLR})\sigma'_{v0} \tan \delta_c$ K and $K_{\max}$ take the same formulae as above, with $K_{\min}$ = 0.2 and α = 0.14	$q_{b,ult} = \min\left[0.21(\text{IFR})^{-1.2} q_{cb}; 0.6 q_{cb}\right]$ $IFR \approx \min\left[1; \left(\frac{B_i}{1.5 L_R}\right)^{0.2}\right]$

Note: The method predicts the ultimate load capacity Q_{ult} of the pile corresponding to a pile head settlement w equal to 10% of the pile diameter B. The method considers open-ended pipe piles in sand to behave as fully-plugged piles during static loading. Accordingly, the ultimate base capacity $Q_{b,ult}$ of an open-ended pipe pile is calculated using the gross cross-sectional area ($\pi B^2/4$) of the pile base. The exponential term in the equation for K accounts for shaft resistance degradation due to pile driving.

For open-ended pipe piles, the plug length ratio (PLR) used in the equation for q_{sL} is that measured at the specific depth where q_{sL} is calculated. If the PLR is not measured, it can be approximated using the same equation provided for the IFR. IFR is the incremental filling ratio averaged over the last 3B of pile driving; if not measured, it can be estimated using the equation provided.

The representative cone resistance q_{cb} for base resistance calculation is q_c averaged from 1B above to 2B below the pile base.

Notation: PPDM = Purdue pile design method, F_{load} = factor that accounts for loading direction (≈ 0.5–0.6 for tension and 1.0 for compression), p_A = reference stress (= 100 kPa or 14.5 psi), L_R = reference length (= 1 m or 39.4 in.), K = coefficient of lateral earth pressure, σ'_{v0} = *in situ* vertical effective stress at the depth being considered, δ_c = critical-state interface friction angle (Figure 4.2), h = vertical distance from the pile base to the depth being considered, B_i = inner diameter of open-ended pipe pile, σ'_{h0} = *in situ* horizontal effective stress at the depth being considered (= $K_0\sigma'_{v0}$), K_0 = coefficient of lateral earth pressure at-rest (Appendix B), q_c = cone resistance, and D_R = relative density (estimated from CPT results using Eq. 4.30).

TABLE 4.15
ICPDM equations for the unit shaft and base resistances for displacement piles driven in sand (Jardine et al., 2005)

Pile Type	Limit Unit Shaft Resistance q_{sL}	Ultimate Unit Base Resistance $q_{b,ult}$
Closed-ended pipe pile	$q_{sL} = (F_{\text{load}}\sigma'_{rc} + \Delta\sigma'_{rd}) \tan \delta_c$ $\sigma'_{rc} = 0.029 q_c \left(\frac{\sigma'_{v0}}{p_A}\right)^{0.13} \left(\max\left[\frac{h}{R}; 8\right]\right)^{-0.38}$ and $\Delta\sigma'_{rd} = \frac{2G\Delta r}{R}$ $G = q_c \left[0.0203 + 0.00125\eta - 1.216 \times 10^{-6}\eta^2\right]^{-1}$ and $\eta = \frac{q_c/p_A}{\sqrt{\sigma'_{v0}/p_A}}$	$q_{b,ult} = \max\left[0.3; 1 - 0.5\log\left(\frac{B}{d_c}\right)\right] q_{cb}$
Open-ended pipe pile	Use the same equations as for closed-ended pipe pile but with an equivalent pile radius R given by: $R = \sqrt{R_o^2 - R_i^2}$ For piles in tension, the value of q_{sL} is decreased further by 10%.	The pile responds as a plugged pile during static loading if: $\frac{B_i}{L_R} < 0.02(D_R - 30)$ or $\frac{B_i}{d_c} < 0.083\frac{q_{cb}}{p_A}$ Response as a plugged pile during static loading: $q_{b,ult} = \max\left[0.15; 0.5 - 0.25\log\left(\frac{B}{d_c}\right); \left(1 - \frac{R_i{}^2}{R_o{}^2}\right)\right] q_{cb}$ $Q_{b,ult} = q_{b,ult}\pi R_o^2$ Response as an unplugged pile during static loading: $q_{ann,ult} = q_{cb}$ and $Q_{b,ult} = q_{ann,ult}\pi(R_o^2 - R_i^2)$
H-pile	Use the same equations as for closed-ended pipe pile but with an equivalent pile radius R given by: $R = \sqrt{\frac{A_b}{\pi}}$ $A_b = 2b_f t_f + (2X_p + t_w)(d - 2t_f)$ $X_p = b_f/8$ if $b_f/2 < (d - 2t_f) < b_f$, and $X_p = b_f 2/[16(d - 2t_f)]$ if $(d - 2t_f) \geq b_f$ 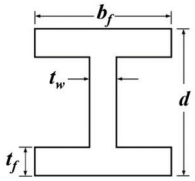	$q_{b,ult} = q_{cb}$
Square or rectangular pile	Use the same equations as for closed-ended pipe pile but with an equivalent pile radius R given by: $R = \sqrt{\frac{A_b}{\pi}}$ $A_b = B_w B_l$; where B_w and B_l = width and length, respectively, of the pile cross-section (in plan)	$q_{b,ult} = 0.7 q_{cb}$

Note: The method predicts the ultimate load capacity Q_{ult} of the pile corresponding to a pile head settlement w equal to 10% of the pile diameter B. In addition, the method is intended to predict the pile capacity measured 10 days after driving for "virgin" piles (i.e., piles that have not been load-tested). The representative cone resistance q_{cb} for base resistance calculation is q_c averaged from $1.5B$ above to $1.5B$ below the pile base.

Notation: ICPDM = Imperial College pile design method, F_{load} = factor that accounts for loading direction (= 0.8 for tension and 1.0 for compression), Δr = radial displacement of soil during pile loading (≈ 0.02 mm or 0.8 mil for lightly rusted steel piles), p_A = reference stress (= 100 kPa or 14.5 psi), L_R = reference length (= 1 m or 39.4 in.), σ'_{rc} = local radial effective stress acting on the pile segment after installation, $\Delta\sigma'_{rd}$ = increase in local radial effective stress associated with constrained dilation during pile loading, σ'_{v0} = *in situ* vertical effective stress at the depth being considered, δ_c = critical-state interface friction angle, B_i = inner diameter of open-ended pipe pile, d_c = cone diameter, R = pile radius, h = vertical distance from the pile base to the depth being considered, q_c = cone resistance, D_R = relative density, R_o = outer radius of open-ended pipe pile, R_i = inner radius of open-ended pipe pile, A_b = area of pile base, G = shear modulus, b_f = width of flange, d = depth of H-section, t_f = thickness of flange, t_w = thickness of web, and $q_{ann,ult}$ = ultimate unit annulus resistance.

TABLE 4.16
UWAPDM equations for the unit shaft and base resistances for displacement piles driven in sand (Lehane et al., 2005)

Pile Type	Limit Unit Shaft Resistance q_{sL}	Ultimate Unit Base Resistance $q_{b,ult}$
Closed-ended pipe pile	$q_{sL} = \frac{f_t}{f_c}\left(\sigma'_{rc} + \Delta\sigma'_{rd}\right)\tan\delta_c$ $\sigma'_{rc} = 0.03 q_c \left[\max\left(\frac{h}{B}; 2\right)\right]^{-0.5}$ $\Delta\sigma'_{rd} = \frac{4G\Delta r}{B}$ and $\frac{G}{q_c} = 185\left[\frac{q_c/p_A}{\sqrt{\sigma'_{v0}/p_A}}\right]^{-0.75}$	$q_{b,ult} = 0.6 q_{cb}$
Open-ended pipe pile	$q_{sL} = \frac{f_t}{f_c}\left(\sigma'_{rc} + \Delta\sigma'_{rd}\right)\tan\delta_c$ $\sigma'_{rc} = 0.03 q_c (A_{rs})^{0.3}\left[\max\left(\frac{h}{B}; 2\right)\right]^{-0.5}$ and $A_{rs} = 1 - \mathrm{IFR}\left(\frac{B_i}{B}\right)^2$ $\Delta\sigma'_{rd} = \frac{4G\Delta r}{B}$ and $\frac{G}{q_c} = 185\left[\frac{q_c/p_A}{\sqrt{\sigma'_{v0}/p_A}}\right]^{-0.75}$ IFR is the average incremental filling ratio measured over the final $20B$ of pile driving; when plug length measurements are not available, it can be estimated using: $\mathrm{IFR} \approx \min\left[1; \left(\frac{B_i}{1.5 L_R}\right)^{0.2}\right]$	$q_{b,ult} = (0.15 + 0.45 A_{rb}) q_{cb}$ $A_{rb} = 1 - \mathrm{FFR}\left(\frac{B_i}{B}\right)^2$ FFR is the final filling ratio, which is defined as the average incremental filling ratio measured over the final $3B$ of pile driving; if not measured, it can be roughly approximated by using the same equation for the IFR.

Note: The method predicts the ultimate load capacity Q_{ult} of the pile corresponding to a pile base settlement equal to 10% of the pile diameter (Lehane et al., 2007; Xu, 2007; Xu et al., 2008). In addition, the method is intended to predict the pile capacity measured 10–20 days after driving.

The method considers open-ended pipe piles in sand to behave as fully-plugged piles during static loading. Accordingly, the ultimate base capacity $Q_{b,ult}$ of an open-ended pipe pile is calculated using the gross cross-sectional area ($\pi B^2/4$) of the pile base.

The representative cone resistance q_{cb} for base resistance calculation is q_c averaged using the Dutch technique (Figure 4.5): $q_{cb} = 0.5(q_{c1}+q_{c2})$, with $q_{c1} = 0.5(q_{c1a} + q_{c1b})$, q_{c1a} = average of the q_c values over a vertical distance of λB below the pile base, q_{c1b} = average of the q_c values over a vertical distance of λB below the pile base following a minimum path rule, and q_{c2} = average of the q_c values over a vertical distance of $8B$ above the pile base following a minimum path rule. The value of q_{c1} is calculated for different λ values ranging from 0.7 to 4.0, and the minimum value of q_{c1} obtained is used in the calculation of q_{cb}. Additional information about the computation of q_{c1} and q_{c2} can be found in Schmertmann (1978). For open-ended pipe piles, B is replaced by B_{eff} [$= B(A_{rb})^{0.5}$] in the calculation of q_{cb}.

In the absence of plug length measurements, the value of the IFR may also be estimated using: IFR $\approx \tanh[0.3(B_i/d_c)^{0.5}]$ (Lehane, 2019). The FFR can be roughly approximated by using the same equation for the IFR.

Notation: UWAPDM = University of Western Australia pile design method, f_t/f_c = ratio of tension to compression capacity (= 0.75 for tension and 1.0 for compression), Δr = radial displacement of soil during pile loading (≈ 0.02 mm or 0.8 mil for lightly rusted steel piles), p_A = reference stress (= 100 kPa or 14.5 psi), L_R = reference length (= 1 m or 39.4 in.), σ'_{rc} = local radial effective stress acting on the pile segment after installation, $\Delta\sigma'_{rd}$ = increase in local radial effective stress associated with constrained dilation during pile loading, σ'_{v0} = *in situ* vertical effective stress at the depth being considered, δ_c = critical-state interface friction angle, A_{rs} = effective shaft area ratio, A_{rb} = effective base area ratio, B_i = inner diameter of open-ended pipe pile, B_{eff}= effective pile diameter, d_c = cone diameter, h = vertical distance from the pile base to the depth being considered, q_c = cone resistance, and G = shear modulus.

TABLE 4.17
AASHTO equations for the unit shaft and base resistances for displacement piles driven in sand (AASHTO, 2020; Nottingham & Schmertmann, 1975)

Pile Type	Limit Unit Shaft Resistance q_{sL}	Limit Unit Base Resistance q_{bL}
Closed-ended pile	$q_{sL} = \begin{cases} 0.125\, K_s f_s \left(\frac{z}{B}\right) \text{ for } 0 \le z \le 8B \\ K_s f_s \text{ for } 8B \le z \le L \end{cases}$	$q_{bL} = q_{cb}$

Note: The representative cone resistance q_{cb} for base resistance calculation is q_c averaged using the Dutch technique (Figure 4.5): $q_{cb} = 0.5(q_{c1}+q_{c2})$, with $q_{c1} = 0.5(q_{c1a} + q_{c1b})$, q_{c1a} = average of the q_c values over a vertical distance of λB below the pile base, q_{c1b} = average of the q_c values over a vertical distance of λB below the pile base following a minimum path rule, and q_{c2} = average of the q_c values over a vertical distance of $8B$ above the pile base following a minimum path rule. The value of q_{c1} is calculated for different λ values ranging from 0.7 to 4.0, and the minimum value of q_{c1} obtained is used in the calculation of q_{cb}. Additional information about the computation of q_{c1} and q_{c2} can be found in AASHTO (2020).

Notation: K_s = correction factor (estimated from the chart provided by AASHTO (2020) as a function of L/B, penetrometer type (electrical versus mechanical), and pile material (steel, concrete, or timber)), f_s = sleeve resistance, L = embedded length of the pile, B = width or diameter of the pile, z = depth measured from the ground surface, and q_c = cone resistance.

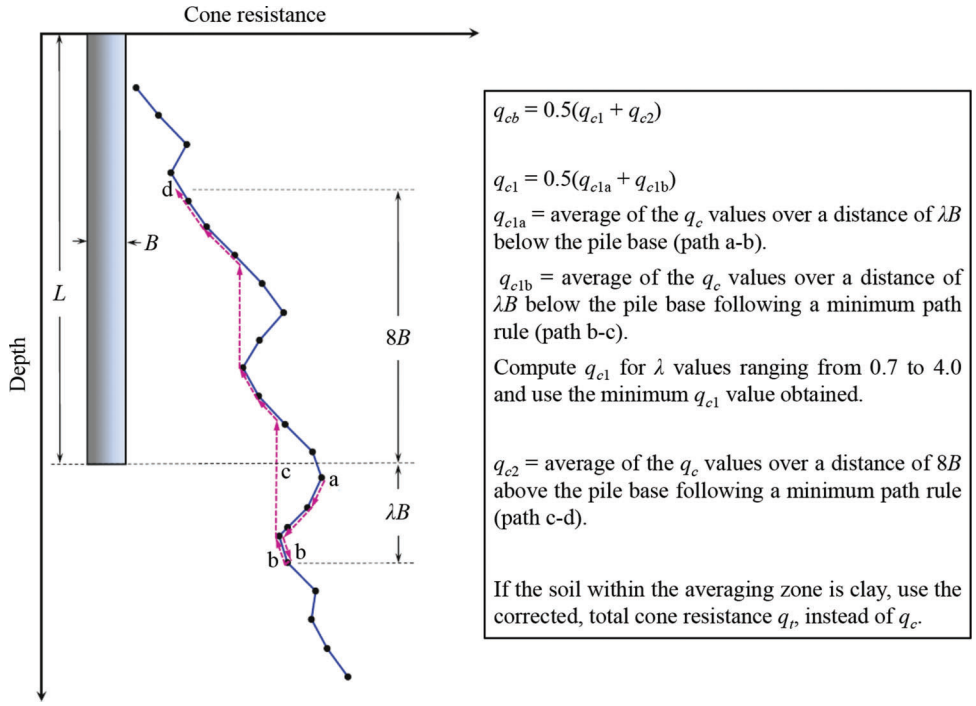

Figure 4.5 Dutch technique for estimation of q_{cb} (modified from Schmertmann, 1978).

TABLE 4.18
MnDOT equations (Modified UniCone method) for the unit shaft and base resistances for displacement piles driven in sand (Dagger et al., 2018)

Pile Type	Limit Unit Shaft Resistance q_{sL}	Ultimate Unit Base Resistance $q_{b,ult}$
Closed-ended pipe pile Open-ended pipe pile H-pile	$q_{sL} = q_E \theta_{pt} \theta_{tc} \theta_{rate} \left(10^{0.732 I_c - 3.605}\right)$ $I_c = \sqrt{(3.47 - \log Q_{tn})^2 + (1.22 + \log F_r)^2}$ $Q_{tn} = \left(\frac{q_t - \sigma_{v0}}{p_A}\right)\left(\frac{p_A}{\sigma'_{v0}}\right)^n$ and $F_r = \frac{f_s}{q_t - \sigma_{v0}} \times 100\%$ $n = \min\left[0.381 I_c + 0.05\left(\frac{\sigma'_{v0}}{p_A}\right) - 0.15; 1\right]$	$q_{b,ult} = \left(10^{0.325 I_c - 1.218}\right) q_{cb}$ I_c is calculated using the same set of equations as those in the estimation of q_{sL}.

Note: The method predicts the maximum load capacity $Q_{\max}$ of the pile (i.e., the maximum load applied on the piles considered in the database). For most (> 90%) of the pile load tests considered in the database, the value of $Q_{\max}$ was nearly equal to the value of Q_{ult} based on the 10% relative settlement criterion (i.e., the load corresponding to a pile head settlement w equal to 10% of the pile diameter B). The following adjustment was proposed to estimate Q_{ult} from $Q_{\max}$: $Q_{ult} = 0.986 Q_{\max}$ (Niazi & Mayne, 2016).

The value of the exponent n is approximately equal to 1 for clay, 0.75 for silt, and 0.5 for sand. For mixed or intermediate soils, iterative calculations are needed to determine the value of I_c. For the first iteration, the method recommends the use of $n = 1$ to obtain an initial value of I_c at the depth being considered. In the next iteration, this initial value of I_c is used to update the value of n, which is then used to obtain a new value of I_c. The process is repeated until the value of I_c converges, which is generally after the third cycle.

The ultimate base capacity $Q_{b,ult}$ of an open-ended pipe pile is calculated using the gross cross-sectional area ($\pi B^2/4$) of the pile base. The representative cone resistance q_{cb} for base resistance calculation is q_E averaged over a vertical distance of B below the pile base (Dagger et al., 2018).

Notation: MnDOT = Minnesota Department of Transportation, B = pile diameter, q_E = effective cone resistance (= $q_t - u_2$); q_t = corrected, total cone resistance; f_s = sleeve resistance; u_2 = pore water pressure measured at the shoulder position behind the cone face; I_c = soil behavior type index; Q_{tn} = normalized cone resistance; F_r = normalized friction ratio; σ_{v0} and σ'_{v0} = *in situ* vertical total and effective stresses, respectively, at the depth being considered; p_A = reference stress (= 100 kPa or 14.5 psi); θ_{pt} = coefficient for pile type (= 1.13 for driven piles); θ_{tc} = coefficient for loading direction (= 0.85 for tension and 1.11 for compression); and θ_{rate} = coefficient for loading procedure (= 1.09 for constant rate of penetration test and 0.97 for maintained load test).

TABLE 4.19
UPDM equations for the unit shaft and base resistances for displacement piles driven in sand (Lehane et al., 2020)

Pile Type	Limit Unit Shaft Resistance q_{sL}	Ultimate Unit Base Resistance $q_{b,ult}$
Closed-ended pipe pile	$q_{sL} = \frac{f_t}{f_c}\left(\sigma'_{rc} + \Delta\sigma'_{rd}\right)\tan\delta_c$ $\sigma'_{rc} = \frac{q_c}{44}\left[\max\left(\frac{h}{B};1\right)\right]^{-0.4}$ and $\Delta\sigma'_{rd} = 0.1q_c\left(\frac{q_c}{\sigma'_{v0}}\right)^{-0.33}\left(\frac{d_c}{B}\right)$	$q_{b,ult} = 0.5q_{cb}$
Open-ended pipe pile	$q_{sL} = \frac{f_t}{f_c}\left(\sigma'_{rc} + \Delta\sigma'_{rd}\right)\tan\delta_c$ $\sigma'_{rc} = \frac{q_c}{44}(A_{rs})^{0.3}\left[\max\left(\frac{h}{B};1\right)\right]^{-0.4}$ and $A_{rs} = 1 - \mathrm{PLR}\left(\frac{B_i}{B}\right)^2$ $\Delta\sigma'_{rd} = 0.1q_c\left(\frac{q_c}{\sigma'_{v0}}\right)^{-0.33}\left(\frac{d_c}{B}\right)$ PLR is the plug length ratio; when plug length measurements are not available, it can be estimated using: $\mathrm{PLR} \approx \tanh\left[0.3\left(\frac{B_i}{d_c}\right)^{0.5}\right]$	$q_{b,ult} = (0.12 + 0.38A_{rb})q_{cb}$ $A_{rb} = 1 - \mathrm{FFR}\left(\frac{B_i}{B}\right)^2$ FFR is the final filling ratio, which is defined as the average incremental filling ratio measured over the final $3B$ of pile driving; if not measured, it can be roughly approximated by using the same equation for the PLR.

Note: The method predicts the ultimate load capacity Q_{ult} of the pile corresponding to a pile base settlement equal to 10% of the pile diameter. In addition, the method is intended to predict the pile capacity measured 14 days after driving.

The method considers open-ended pipe piles in sand to behave as fully-plugged piles during static loading. Accordingly, the ultimate base capacity $Q_{b,ult}$ of an open-ended pipe pile is calculated using the gross cross-sectional area ($\pi B^2/4$) of the pile base.

For piles installed in relatively homogeneous sands, the representative cone resistance q_{cb} for base resistance calculation is q_c averaged from $1.5B$ above to $1.5B$ below the pile base. For piles installed in highly variable soil profiles (i.e., when q_c varies significantly in the vicinity of the pile base), q_{cb} can be either taken as $1.2q_{c,\mathrm{Dutch}}$ or estimated using the procedure developed by Boulanger and DeJong (2018); $q_{c,\mathrm{Dutch}} = q_c$ averaged using the Dutch technique (Schmertmann, 1978). For open-ended pipe piles, B is replaced by B_{eff} [$= B(A_{rb})^{0.5}$] in the calculation of q_{cb}.

Notation: UPDM = Unified pile design method, f_t/f_c = ratio of tension to compression capacity (= 0.75 for tension and 1.0 for compression), σ'_{rc} = local radial effective stress acting on the pile segment after installation, $\Delta\sigma'_{rd}$ = increase in local radial effective stress associated with constrained dilation during pile loading, σ'_{v0} = *in situ* vertical effective stress at the depth being considered, δ_c = critical-state interface friction angle (= 29° in the absence of laboratory interface shear test results), A_{rs} = effective shaft area ratio, A_{rb} = effective base area ratio, B_i = inner diameter of open-ended pipe pile, B_{eff} = effective pile diameter, d_c = cone diameter, h = vertical distance from the pile base to the depth being considered, and q_c = cone resistance.

4.5.3 Design Methods for Displacement Piles in Clayey Soil

TABLE 4.20
PPDM equations for the unit shaft and base resistances for displacement piles driven in clay (Basu et al., 2009; Salgado, 2008)

Pile Type	Limit Unit Shaft Resistance q_{sL}	Ultimate Unit Base Resistance $q_{b,ult}$
Closed-ended pipe pile	$q_{sL} = \alpha s_u$ $\alpha = A_1 + (1 - A_1)\exp\left[-\left(\frac{\sigma'_{v0}}{p_A}\right)(\phi_c - \phi_{r,\min})^{A_2}\right]$ for short-term resistance, and $\alpha = 1.28\left(\frac{s_u}{\sigma'_{v0}}\right)^{-0.05}\left\{A_1 + (1 - A_1)\exp\left[-\left(\frac{\sigma'_{v0}}{p_A}\right)(\phi_c - \phi_{r,\min})^{A_3}\right]\right\}$ for long-term resistance A_1 = 0.75 for $\phi_c - \phi_{r,\min} \le 5°$, 0.43 for $\phi_c - \phi_{r,\min} \ge 12°$ and a linearly interpolated value for $5° < \phi_c - \phi_{r,\min} < 12°$ $A_2 = 0.55 + 0.43\ln\left(\frac{s_u}{\sigma'_{v0}}\right)$ and $A_3 = 0.64 + 0.40\ln\left(\frac{s_u}{\sigma'_{v0}}\right)$	$q_{b,ult} \approx \begin{cases} 10s_u \text{ for short-term resistance} \\ 12s_u \text{ for long-term resistance} \end{cases}$

Note: The method predicts the ultimate load capacity Q_{ult} of the pile corresponding to a pile head settlement w equal to 10% of the pile diameter B.

Short-term resistance refers to the resistance available immediately after pile installation (corresponding to zero dissipation of excess pore water pressure). Long-term resistance refers to the resistance available after dissipation of the excess pore water pressure generated during pile installation.

Notation: PPDM = Purdue pile design method, p_A = reference stress (= 100 kPa or 14.5 psi), σ'_{v0} = *in situ* vertical effective stress at the depth being considered, ϕ_c = critical-state friction angle, $\phi_{r,\min}$ = minimum residual-state friction angle (Appendix E), and s_u = undrained shear strength (estimated from CPT results using the equations provided in the chapter).

TABLE 4.21
ICPDM equations for the unit shaft and base resistances for displacement piles driven in clay (Jardine et al., 2005)

Pile Type	Limit Unit Shaft Resistance q_{sL}	Ultimate Unit Base Resistance $q_{b,ult}$
Closed-ended pipe pile	$q_{sL} = F_{\text{load}} K \sigma'_{v0} \tan \delta_r$ $K = \left[2.2 + 0.016\text{OCR} - 0.87\Delta I_{vy}\right]\text{OCR}^{0.42}\left(\max\left[\frac{h}{R}; 8\right]\right)^{-0.20}$ $\Delta I_{vy} = \log_{10} S_t$ and $S_t = \frac{s_u}{s_{ur}}$	$q_{b,ult} = \begin{cases} 0.8q_{cb} \text{ for undrained loading} \\ 1.3q_{cb} \text{ for drained loading} \end{cases}$
Open-ended pipe pile	Use the same equations as for closed-ended pipe pile but with an equivalent pile radius R given by: $R = \sqrt{R_o^2 - R_i^2}$	The pile responds as a plugged pile during static loading if: $\frac{B_i}{d_c} + 0.45\frac{q_{cb}}{p_A} < 36$ Response as a plugged pile during static loading: $q_{b,ult} = \begin{cases} 0.4q_{cb} \text{ for undrained loading} \\ 0.65q_{cb} \text{ for drained loading} \end{cases}$ $Q_{b,ult} = q_{b,ult}\pi R_o^2$ Response as an unplugged pile during static loading: $q_{ann,ult} = \begin{cases} q_{cb} \text{ for undrained loading} \\ 1.6q_{cb} \text{ for drained loading} \end{cases}$ $Q_{b,ult} = q_{ann,ult}\pi\left(R_o^2 - R_i^2\right)$
H-pile	Use the same equations as for closed-ended pipe pile but with an equivalent pile radius R given by: $R = \sqrt{\frac{A_b}{\pi}}$ $A_b = 2b_f t_f + (2X_p + t_w)(d - 2t_f)$ $X_p = b_f/8$ if $b_f/2 < (d - 2t_f) < b_f$, and $X_p = b_f^2/[16(d - 2t_f)]$ if $(d - 2t_f) \geq b_f$ 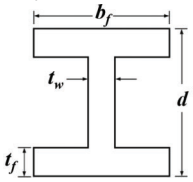	$q_{b,ult} = q_{cb}$
Square or rectangular pile	Use the same equations as for closed-ended pipe pile but with an equivalent pile radius R given by: $R = \sqrt{\frac{A_b}{\pi}}$ $A_b = B_w B_l$; where B_w and B_l = width and length, respectively, of the pile cross-section (in plan)	$q_{b,ult} = 0.7q_{cb}$

Note: The method predicts the ultimate load capacity Q_{ult} of the pile corresponding to a pile head settlement w equal to 10% of the pile diameter B. In addition, the method is intended to estimate the shaft resistance after dissipation of the excess pore water pressure generated during pile installation. The representative cone resistance q_{cb} for base resistance calculation is q_t averaged from $1.5B$ above to $1.5B$ below the pile base.

The residual interface friction angle δ_r can be determined from the results of ring shear interface tests performed for the applicable value of normal effective stress (Ramsey et al., 1998). If such test results are unavailable, it is possible to estimate the value of δ_r by recognizing that it varies with the normal effective stress σ' acting on the pile shaft, which, for production piles, is typically rough, so that δ_r is approximately equal to ϕ_r. Note that σ', in the context of pile shaft resistance calculation, is the horizontal effective stress σ'_h on the pile operative at the time of shearing: $\sigma'_h = F_{\text{load}} K \sigma'_{v0}$.

Notation: ICPDM = Imperial College pile design method, $F_{\text{load}} = 0.8$ regardless of the loading direction, p_A = reference stress (= 100 kPa or 14.5 psi), L_R = reference length (= 1 m or 39.4 in.), q_t = corrected, total cone resistance, σ'_{v0} = *in situ* vertical effective stress at the depth being considered, A_b = area of pile base, B_i = inner diameter of open-ended pipe pile, d_c = cone diameter, R = pile radius, h = vertical distance from the pile base to the depth being considered, OCR = overconsolidation ratio, s_u = undrained shear strength, ΔI_{vy} = relative void index at yield in e–log σ'_v space, S_t = sensitivity, s_{ur} = remolded undrained shear strength, LI = liquidity index [= (wc – PL)/PI], wc = water content, PL = plastic limit, PI = plasticity index, R_o = outer radius of open-ended pipe pile, R_i = inner radius of open-ended pipe pile, b_f = width of flange, d = depth of H-section, t_f = thickness of flange, t_w = thickness of web, and $q_{ann,ult}$ = ultimate unit annulus resistance.

TABLE 4.22
UWAPDM equations for the unit shaft and base resistances for displacement piles driven in clay (Lehane, 2019; Lehane et al., 2013)

Pile Type	Limit Unit Shaft Resistance q_{sL}	Ultimate Unit Base Resistance $q_{b,ult}$
Closed-ended pipe pile	$q_{sL}=\dfrac{0.23q_t\left[\max\left(\dfrac{h}{R};1\right)\right]^{-0.2}}{\left(\dfrac{q_t}{\sigma'_{v0}}\right)^{0.15}}\tan\delta_r$ or $q_{sL}=0.055q_t\left[\max\left(\dfrac{h}{R};1\right)\right]^{-0.2}$	$q_{b,ult}\approx 0.5q_{cb}$ for undrained loading
Open-ended pipe pile	Use the same equations as for closed-ended pipe pile but with an equivalent pile radius R given by: $R=\sqrt{R_o^2-R_i^2}$	Response as a plugged pile during static loading: $q_{b,ult}\approx 0.5q_{cb}$ for undrained loading

Note: The method is intended to estimate the shaft resistance after dissipation of the excess pore water pressure generated during pile installation (Lehane, 2019; Lehane et al., 2017). Two equations were proposed for the limit unit shaft resistance q_{sL} and the second one was reported by Lehane et al. (2013) to be slightly more reliable than the first. The ultimate base capacity $Q_{b,ult}$ of an open-ended pipe pile is calculated using the gross cross-sectional area ($\pi B^2/4$) of the pile base.

The residual interface friction angle δ_r can be determined from the results of ring shear interface tests performed for the applicable value of normal effective stress (Ramsey et al., 1998). If such test results are unavailable, it is possible to estimate the value of δ_r by recognizing that it varies with the normal effective stress σ' acting on the pile shaft, which, for production piles, is typically rough, so that δ_r is approximately equal to ϕ_r. Note that σ', in the context of pile shaft resistance calculation, is the horizontal effective stress σ'_h on the pile operative at the time of shearing: $\sigma'_h = 0.23q_t[\max(h/R;1)]^{-0.2}/(q_t/\sigma'_{v0})^{0.15}$.

Notation: UWAPDM = University of Western Australia pile design method, q_t = corrected, total cone resistance, σ'_{v0} = *in situ* vertical effective stress at the depth being considered, R = pile radius, h = vertical distance from the pile base to the depth being considered, R_o = outer radius of open-ended pipe pile, and R_i = inner radius of open-ended pipe pile.

TABLE 4.23
AASHTO equations for the unit shaft and base resistances for displacement piles driven in clay (AASHTO, 2020; Nottingham & Schmertmann, 1975)

Pile Type	Limit Unit Shaft Resistance q_{sL}	Limit Unit Base Resistance q_{bL}
Closed-ended pile	$q_{sL}=\begin{cases}0.125K_cf_s\left(\dfrac{z}{B}\right) \text{ for } 0\le z\le 8B\\ K_cf_s \text{ for } 8B\le z\le L\end{cases}$	$q_{bL}=q_{cb}$

Note: The representative cone resistance q_{cb} for base resistance calculation is q_t averaged using the Dutch technique (Figure 4.5): q_{cb} = $0.5(q_{c1}+q_{c2})$, with q_{c1} = $0.5(q_{c1a} + q_{c1b})$, q_{c1a} = average of the q_t values over a vertical distance of λB below the pile base, q_{c1b} = average of the q_t values over a vertical distance of λB below the pile base following a minimum path rule, and q_{c2} = average of the q_t values over a vertical distance of $8B$ above the pile base following a minimum path rule. The value of q_{c1} is calculated for different λ values ranging from 0.7 to 4.0, and the minimum value of q_{c1} obtained is used in the calculation of q_{cb}. Additional information about the computation of q_{c1} and q_{c2} can be found in AASHTO (2020).

Notation: K_c = correction factor [estimated from the chart provided by AASHTO (2020) as a function of f_s and pile material (steel, concrete, or timber)], f_s = sleeve resistance, L = embedded length of the pile, B = width or diameter of the pile, z = depth measured from the ground surface, and q_t = corrected, total cone resistance (Eq. 4.1).

TABLE 4.24
MnDOT equations (Modified UniCone method) for the unit shaft and base resistances for displacement piles driven in clay (Dagger et al., 2018)

Pile Type	Limit Unit Shaft Resistance q_{sL}	Ultimate Unit Base Resistance $q_{b,ult}$
Closed-ended pipe pile Open-ended pipe pile H-pile	$q_{sL} = q_E \theta_{pt} \theta_{tc} \theta_{rate} \left(10^{0.732 I_c - 3.605}\right)$ $I_c = \sqrt{(3.47 - \log Q_{tn})^2 + (1.22 + \log F_r)^2}$ $Q_{tn} = \left(\frac{q_t - \sigma_{v0}}{p_A}\right)\left(\frac{p_A}{\sigma'_{v0}}\right)^n$ and $F_r = \frac{f_s}{q_t - \sigma_{v0}} \times 100\%$ $n = \min\left[0.381 I_c + 0.05\left(\frac{\sigma'_{v0}}{p_A}\right) - 0.15; 1\right]$	$q_{b,ult} = \left(10^{0.325 I_c - 1.218}\right) q_{cb}$ I_c is calculated using the same set of equations as those in the estimation of q_{sL}.

Note: The method predicts the maximum load capacity $Q_{\max}$ of the pile (i.e., the maximum load applied on the piles considered in the database). For most (> 90%) of the pile load tests considered in the database, the value of $Q_{\max}$ was nearly equal to the value of Q_{ult} based on the 10% relative settlement criterion (i.e., the load corresponding to a pile head settlement w equal to 10% of the pile diameter B). The following adjustment was proposed to estimate Q_{ult} from $Q_{\max}$: $Q_{ult} = 0.986 Q_{\max}$ (Niazi & Mayne, 2016).

The value of the exponent n is approximately equal to 1 for clay, 0.75 for silt, and 0.5 for sand. For mixed or intermediate soils, iterative calculations are needed to determine the value of I_c. For the first iteration, the method recommends the use of $n = 1$ to obtain an initial value of I_c at the depth being considered. In the next iteration, this initial value of I_c is used to update the value of n, which is then used to obtain a new value of I_c. The process is repeated until the value of I_c converges, which is generally after the third cycle. Additional information on sensitive clays can be found in Niazi and Mayne (2016).

The ultimate base capacity $Q_{b,ult}$ of an open-ended pipe pile is calculated using the gross cross-sectional area ($\pi B^2/4$) of the pile base. The representative cone resistance q_{cb} for base resistance calculation is q_E averaged over a vertical distance of B below the pile base (Dagger et al., 2018).

Notation: MnDOT = Minnesota Department of Transportation, B = pile diameter, q_E = effective cone resistance (= $q_t - u_2$); q_t = corrected, total cone resistance; f_s = sleeve resistance; u_2 = pore water pressure measured at the shoulder position behind the cone face; I_c = soil behavior type index; Q_{tn} = normalized cone resistance; F_r = normalized friction ratio; σ_{v0} and σ'_{v0} = *in situ* vertical total and effective stresses, respectively, at the depth being considered; p_A = reference stress (= 100 kPa or 14.5 psi); θ_{pt} = coefficient for pile type (= 1.13 for driven piles); θ_{tc} = coefficient for loading direction (= 0.85 for tension and 1.11 for compression); and θ_{rate} = coefficient for loading procedure (= 1.09 for constant rate of penetration test and 0.97 for maintained load test).

TABLE 4.25
NDOT equations for the unit shaft and base resistances for displacement piles driven in clay (Song et al., 2019)

Pile Type and Reference	Unit Shaft Resistance	Unit Base Resistance
Closed-ended pipe pile Precast prestressed concrete pile (modified from de Ruiter and Beringen, 1979)	$q_s = \frac{q_t}{60}$	$q_b = 0.54 q_{cb}$
H-pile (modified from Tumay and Fakhroo, 1982)	$q_s = \min\left[m^* f_{s,avg}; 0.72 p_A\right]$ $m^* = 0.45 + 8.55 \exp\left(-0.09 f_{s,avg}\right)$ $f_{s,avg} = \frac{\sum_{i=1}^{n} f_{si} \Delta z_i}{\sum_{i=1}^{n} \Delta z_i}$	$q_b = \min\left[0.5 q_{cb}; 150 p_A\right]$

Note: The method is applicable to fine-grained Nebraska soils and predicts the pile capacity that would be obtained from dynamic load tests performed using the pile driving analyzer (PDA) at the end of initial driving and post-processed using the signal matching program CAPWAP (Case Pile Wave Analysis Program).

In the de Ruiter and Beringen (1979) method, the representative cone resistance q_{cb} for base resistance calculation is q_t averaged using the Dutch technique (Figure 4.5). In the Tumay and Fakhroo (1982) method, q_{cb} is calculated in a manner similar to the Dutch technique: $q_{cb} = 0.5(q_{c1} + q_{c2})$, with $q_{c1} = 0.5(q_{c1a} + q_{c1b})$, q_{c1a} = average of the q_t values over a vertical distance of $4B$ below the pile base, q_{c1b} = average of the q_t values over a vertical distance of $4B$ below the pile base following a minimum path rule, and q_{c2} = average of the q_t values over a vertical distance of $8B$ above the pile base following a minimum path rule.

Notation: NDOT = Nebraska Department of Transportation, m^* = modified friction coefficient, $f_{s,avg}$ = weighted-average sleeve resistance, f_{si} = sleeve resistance of soil layer i, Δz_i = thickness of soil layer i, n = number of soil layers in contact with the pile shaft, p_A = reference stress (= 100 kPa or 14.5 psi), B = pile diameter, and q_t = corrected, total cone resistance (Eq. 4.1).

REFERENCES

AASHTO. (1991). *AASHTO M 145: Standard specification for classification of soils and soil-aggregate mixtures for highway construction purposes*. American Association of State Highway and Transportation Officials.

AASHTO. (2020). *AASHTO LRFD bridge design specifications* (9th ed.). American Association of State Highway and Transportation Officials.

Akinlotan, O. (2017). Mineralogy and palaeoenvironments: the Weald Basin (Early Cretaceous), Southeast England. *The Depositional Record*, *3*(2), 187–200.

Allen, T. M. (2005, February). *Development of geotechnical resistance factors and downdrag load factors for LRFD foundation strength limit state design* (Report No. FHWA-NHI-05-052). National Highway Institute, Federal Highway Administration.

Altuhafi, F. N., Coop, M. R., & Georgiannou, V. N. (2016). Effect of particle shape on the mechanical behavior of natural sands. *Journal of Geotechnical and Geoenvironmental Engineering*, *142*(12), 04016071.

Altuhafi, F. N., Jardine, R. J., Georgiannou, V. N., & Moinet, W. W. (2018, June). Effects of particle breakage and stress reversal on the behaviour of sand around displacement piles. *Géotechnique*, *68*(6), 546–555.

Altuhafi, F., O'Sullivan, C., & Cavarretta, I. (2013). Analysis of an image-based method to quantify the size and shape of sand particles. *Journal of Geotechnical and Geoenvironmental Engineering*, *139*(8), 1290–1307.

Anderson, J. B., Townsend, F. C., & Horta, E. (2004). A brief study on the repeatability of in-situ tests at the Florida department of transportation deep foundations research site in Orlando, Florida. In A. V. de Fonseca, & P. W. Mayne (Eds.), *Geotechnical and Geophysical Site Characterization*, *2*, 1597–1604.

Argyilan, E. P., Johnston, J. W., Lepper, K., Monaghan, G. W., & Thompson, T. A. (2018). Lake level, shoreline, and dune behavior along the Indiana southern shore of Lake Michigan. *Ancient Oceans, Orogenic Uplifts, and Glacial Ice: Geologic Crossroads in America's Heartland*. Geological Society of America Field Guide, *51*, 181–203.

ASTM. (2012). *ASTM D5778-12: Standard test method for electronic friction cone and piezocone penetration testing of soils*. ASTM International.

ASTM. (2017). *ASTM D2487: Standard practice for classification of soils for engineering purposes (unified soil classification system)*. ASTM International.

Ault, C. H., & Sullivan, D. M. (1982, October). *Faulting in southwest Indiana* (U.S. Nuclear Regulatory Commission Report NUREG/CR-2908). Indiana Geological Survey.

Basu, D., & Salgado, R. (2012). Load and resistance factor design of drilled shafts in sand. *Journal of Geotechnical and Geoenvironmental Engineering*, *138*(12), 1455–1469.

Basu, D., & Salgado, R. (2014). Closure to "Load and resistance factor design of drilled shafts in sand" by D. Basu and Rodrigo Salgado. *Journal of Geotechnical and Geoenvironmental Engineering*, *140*(3), https://doi.org/10.1061/(ASCE)GT.1943-5606.0001055

Basu, P., Prezzi, M., Salgado, R., & Chakraborty, T. (2014). Shaft resistance and setup factors for piles jacked in clay. *Journal of Geotechnical and Geoenvironmental Engineering*, *140*(3), 04013026.

Basu, P., Salgado, R., Prezzi, M., & Chakraborty, T. (2009). *A method for accounting for pile setup and relaxation in pile design and quality assurance* (Joint Transportation Research Program Publication FHWA/IN/JTRP-2009/24). West Lafayette, IN: Purdue University. https://doi.org/10.5703/1288284314282.

Becker, D. E. (1996). Eighteenth Canadian geotechnical colloquium: Limit states design for foundations. Part I. An overview of the foundation design process. *Canadian Geotechnical Journal*, *33*(6), 956–983.

De Beer, E., Lousberg, E., De Jonghe, A., Carpentier, R., & Wallays, M. (1980). Analysis of the results of loading tests performed on displacement piles of different types and sizes penetrating at a relatively small depth into a very dense sand layer. *Recent Developments in the Design and Construction of Piles* (pp. 199–211). The Institution of Civil Engineers.

Bellotti, R., Jamiolkowski, M., Presti, D. C. F. Lo, & O'Neill, D. A. (1996). Anisotropy of small strain stiffness in Ticino sand. *Géotechnique*, *46*(1), 115–131.

Bishop, A. W., Green, G. E., Garga, V. K., Andresen, A., & Brown, J. D. (1971, December). A new ring shear apparatus and its application to the measurement of residual strength. *Géotechnique*, *21*(4), 273–328.

Bisht, V., Salgado, R., & Prezzi, M. (2021, December 1). The material point method for cone penetration in clays. *Journal of Geotechnical and Geoenvironmental Engineering*, *147*(12), 04021158.

Bolton, M. D. (1986). The strength and dilatancy of sands. *Géotechnique*, *36*(1), 65–78.

Bonaparte, R. (1982). *A time-dependent constitutive model for cohesive soils* [Doctoral dissertation, University of California, Berkeley].

Boulanger, R. W. W., & DeJong, J. T. T. (2018). Inverse filtering procedure to correct cone penetration data for thin-layer and transition effects (pp. 25–44). In *Cone Penetration Testing 2018* (1st ed.). CRC Press.

Bozozuk, M. (1978). Bridge foundations move. *Transportation Research Record: Journal of the Transportation Research Board*, No. 678, 17–21.

Brooker, E. W., & Ireland, H. O. (1965). Earth pressures at rest related to stress history. *Canadian Geotechnical Journal*, *2*(1), 1–15.

Brown, D. A., Turner, J. P., & Castelli, R. J. (2010). *Drilled shafts: construction procedures and LRFD design methods* (Report No. FHWA NHI-10-016). Federal Highway Administration.

Brown, R. (2016). Geomorphons: Landform and property predictions in a glacial moraine in Indiana landscapes. *Catena*, *142*, 66–76.

Campanella, R. G., Robertson, P. K., & Gillespie, D. (1986). Seismic cone penetration test. *Use of In-Situ Tests in Geotechnical Engineering*, *GSP 6*, 116–130. American Society of Civil Engineers.

Campanella, R. G., & Weemees, I. (1990). Development and use of an electrical resistivity cone for groundwater contamination studies. *Canadian Geotechnical Journal*, *27*(5), 557–567.

Cao, Z., & Wang, Y. (2013, February). Bayesian approach for probabilistic site characterization using cone penetration tests. *Journal of Geotechnical and Geoenvironmental Engineering, 139*(2), 267–276.

Carraro, J. A. H., Prezzi, M., & Salgado, R. (2009). Shear strength and stiffness of sands containing plastic or nonplastic fines. *Journal of Geotechnical and Geoenvironmental Engineering*, *135*(9), 1167–1178.

Chakraborty, T. (2009). *Development of a clay constitutive model and its application to pile boundary value problems* [Doctoral dissertation, Purdue University].

Chakraborty, T., Salgado, R., Basu, P., & Prezzi, M. (2013). Shaft resistance of drilled shafts in clay. *Journal of Geotechnical and Geoenvironmental Engineering*, *139*(4), 548–563.

Cho, G.-C., Dodds, J., & Santamarina, J. C. (2006, May). Particle shape effects on packing density, stiffness, and strength: natural and crushed sands. *Journal of Geotechnical and Geoenvironmental Engineering*, *132*(5), 591–602.

Colgan, P. M., Mickelson, D. M., & Cutler, P. M. (2003). Ice-marginal terrestrial landsystems: Southern-Laurentide Ice Sheet margin. In D. A. Evans (Ed.), *Glacial Landsystems* (pp. 111–142). Routledge.

Coop, M. R., & Lee, I. K. (1993). The behaviour of granular soils at elevated stresses. *Predictive Soil Mechanics: Proceedings of the Wroth Memorial Symposium* (pp. 186–198). Thomas Telford.

Cressey, G. B. (1928). *The Indiana sand dunes and shorelines of the Lake Michigan basin*. University of Chicago Press.

Dafalias, Y. F., Manzari, M. T., & Papadimitriou, A. G. (2006). SANICLAY: Simple anisotropic clay plasticity model. *International Journal for Numerical and Analytical Methods in Geomechanics*, *30*(12), 1231–1257.

Dagger, R., Saftner, D., & Mayne, P. W. (2018, November). *Cone penetration test design guide for state geotechnical engineers* (Report No. MN/RC 2018-32). University of Minnesota.

Davis, E. H., & Booker, J. R. (1973, December). The effect of increasing strength with depth on the bearing capacity of clays. *Géotechnique*, *23*(4), 551–563.

DeJong, J. T., Jaeger, R. A., Boulanger, R. W., Randolph, M. F., & Wahl, D. A. J. (2013). Variable penetration rate cone testing for characterization of intermediate soils. In R. Q. Coutinho & P. W. Mayne (Eds.), *Geotechnical and Geophysical Site Characterization 4*, *1*, 25–42.

DeJong, J. T., & Randolph, M. (2012). Influence of partial consolidation during cone penetration on estimated soil behavior type and pore pressure dissipation measurements. *Journal of Geotechnical and Geoenvironmental Engineering*, *138*(7), 777–788.

Finno, R. J. (1989). Subsurface conditions and pile installation data: 1989 foundation engineering congress test section. *Proceedings of Symposium on Predicted and Observed Axial Behavior of Piles*, *GSP 23*, 1–74. American Society of Civil Engineers.

Fleming, A. H., Brown, S. E., & Ferguson, V. R. (1993). *The hydrogeologic framework of Marion County, Indiana*. Indiana Geological Survey Open-File Report 93.

Florea, L. J., Hasenmueller, N. R., Branam, T. D., Frushour, S. S., & Powell, R. L. (2018). Karst geology and hydrogeology of the Mitchell Plateau of south-central Indiana. *Ancient Oceans, Orogenic Uplifts, and Glacial Ice: Geologic Crossroads in America's Heartland*, *Geological Society of America Field Guide 51*, 95–112. Geological Society of America.

Foye, K. C. (2005). *A rational, probabilistic method for the development of geotechnical load and resistance factor design* [Doctoral dissertation, Purdue University]. Purdue e-Pubs.

Foye, K. C., Abou-Jaoude, G., Prezzi, M., & Salgado, R. (2009). Resistance factors for use in load and resistance factor design of driven pipe piles in sands. *Journal of Geotechnical and Geoenvironmental Engineering*, *135*(1), 1–13.

Foye, K. C., Basu, P., & Prezzi, M. (2008, September). Immediate settlement of shallow foundations bearing on clay. *International Journal of Geomechanics*, *8*(5), 300–310.

Foye, K. C., Salgado, R., & Scott, B. (2006a). Assessment of variable uncertainties for reliability-based design of foundations. *Journal of Geotechnical and Geoenvironmental Engineering*, *132*(9), 1197–1207.

Foye, K. C., Salgado, R., & Scott, B. (2006b). Resistance factors for use in shallow foundation LRFD. *Journal of Geotechnical and Geoenvironmental Engineering*, *132*(9), 1208–1218.

Fukue, M., Minato, T., Matsumoto, M., Horibe, H., & Taya, N. (2001). Use of resistivity cone for detecting contaminated soil layers. *Engineering Geology*, *60*(1–4), 361–369.

Galvis-Castro, A. C., Tovar-Valencia, R. D., Salgado, R., & Prezzi, M. (2019). Effect of loading direction on the shaft resistance of jacked piles in dense sand. *Géotechnique*, *69*(1), 16–28.

Ganju, E., Han, F., Prezzi, M., & Salgado, R. (2020). Static capacity of closed-ended pipe pile driven in gravelly sand. *Journal of Geotechnical and Geoenvironmental Engineering*, *146*(4), 04020008.

Ganju, E., Han, F., Prezzi, M., Salgado, R., & Pereira, J. S. (2020). Quantification of displacement and particle crushing around a penetrometer tip. *Geoscience Frontiers*, *11*(2), 389–399.

Ganju, E., Prezzi, M., & Salgado, R. (2017). Algorithm for generation of stratigraphic profiles using cone penetration test data. *Computers and Geotechnics*, *90*, 73–84.

Ganju, E., Salgado, R., & Prezzi, M. (2019). Site variability characterization using cone penetration test data. *Proceedings of Geo-Congress 2019—Eighth International Conference on Case Histories in Geotechnical Engineering* (pp. 152–157).

Gao, Z., Zhao, J., Li, X.-S., & Dafalias, Y. F. (2014). A critical state sand plasticity model accounting for fabric evolution. *International Journal for Numerical and Analytical Methods in Geomechanics*, *38*(4), 370–390.

Gasparre, A. (2005, July). *Advanced laboratory characterisation of London clay* [Doctoral dissertation, Imperial College]. http://hdl.handle.net/10044/1/45389

Gavin, K., Adekunte, A., & O'Kelly, B. (2009). A field investigation of vertical footing response on sand. *Proceedings of the ICE–Geotechnical Engineering*, *162*(5), 257–267.

Gens, A. (1982). *Stress-strain and strength of a low plasticity clay* [Doctoral dissertation, Imperial College]. http://hdl.handle.net/10044/1/8410

Giroud, J.-P. (1968). Settlement of a linearly loaded rectangular area. *Journal of the Soil Mechanics and Foundations Division*, *94*(4), 813–831.

Gooding, A. M. (1973). *Characteristics of late Wisconsinan tills in eastern Indiana* (Department of Natural Resources Geological Survey Bulletin 49). Indiana Geological Survey.

Gray, H. (n.d.). *Loess* [Webpage]. Indiana Geological and Water Survey. https://igws.indiana.edu/surficial/loess

Gray, H. H. (2000). *Physiographic divisions of Indiana* (Indiana Geological Survey Special Report 61). Indiana Geological Survey.

Hall, R. D., & Anderson, A. K. (2000). Comparative soil development of Quaternary paleosols of the central United States. *Palaeogeography, Palaeoclimatology, Palaeoecology*, *158*(1–2), 109–145.

Han, F., Ganju, E., Prezzi, M., Salgado, R., & Zaheer, M. (2020). Axial resistance of open-ended pipe pile driven in gravelly sand. *Géotechnique*, *70*(2), 138–152.

Han, F., Ganju, E., Salgado, R., & Prezzi, M. (2018). Effects of interface roughness, particle geometry, and gradation on the sand-steel interface friction angle. *Journal of Geotechnical and Geoenvironmental Engineering*, *144*(12), 04018096.

Han, F., Ganju, E., Salgado, R., & Prezzi, M. (2019a). Closure to "Effects of interface roughness, particle geometry, and gradation on the sand–steel interface friction angle" by Fei Han, Eshan Ganju, Rodrigo Salgado, and Monica Prezzi. *Journal of Geotechnical and Geoenvironmental Engineering*, *145*(11), 07019017.

Han, F., Ganju, E., Salgado, R., & Prezzi, M. (2019b). Comparison of the load response of closed-ended and open-ended pipe piles driven in gravelly sand. *Acta Geotechnica*, *14*, 1785–1803.

Han, F., Lim, J., Salgado, R., Prezzi, M., & Zaheer, M. (2015). *Load and resistance factor design of bridge foundations accounting for pile group–soil interaction* (Joint Transportation Research Program Publication No. FHWA/IN/JTRP-2015/24) West Lafayette, IN: Purdue University. http://dx.doi.org/10.5703/1288284316009

Han, F., Salgado, R., Prezzi, M., & Lim, J. (2017, March). Shaft and base resistance of non-displacement piles in sand. *Computers and Geotechnics*, *83*, 184–197.

Han, F., Salgado, R., Prezzi, M., & Lim, J. (2019). Axial resistance of non-displacement pile groups in sand. *Journal of Geotechnical and Geoenvironmental Engineering*, *145*(7), 04019027.

Hasenmueller, N. R., & Packman, D. M. (n.d.). *Karst features in Indiana* [Webpage]. Indiana Geological and Water Survey. https://igws.indiana.edu/bedrock/karst

Herle, I., & Gudehus, G. (1999, September). Determination of parameters of a hypoplastic constitutive model from properties of grain assemblies. *Mechanics of Cohesive-Frictional Materials*, *4*(5), 461–486.

Hildenbrand, T. G., & Ravat, D. (1997). Geophysical setting of the Wabash Valley Fault System. *Seismological Research Letters*, *68*(4), 567–585.

Hill, J. R. (1974). *The Indiana dunes–legacy of sand* (Indiana Geological Survey Special Report 8). Indiana Geological Survey.

Hogentogler & Co. Inc. (2004). *CPT brochure 2004*.

Hryciw, R. D., Zheng, J., & Shetler, K. (2016). Particle roundness and sphericity from images of assemblies by chart estimates and computer methods. *Journal of Geotechnical and Geoenvironmental Engineering*, *142*(9), 04016038.

IGWS. (n.d.). *Bedrock geology of Indiana* [Webpage]. Indiana Geological and Water Survey. https://igws.indiana.edu/bedrock

Ireland, H. O., Moretto, O., & Vargas, M. (1970, June). The dynamic penetration test: A standard that is not standardized. *Géotechnique*, *20*(2), 185–192.

Jamiolkowski, M., Ladd, C. C., Germaine, J. T., & Lancellotta, R. (1985, August). New developments in field and lab testing of soils. *Proceedings of the 11th International Conference on Soil Mechanics and Foundation Engineering* (pp. 57–153). A. A. Balkema.

Jardine, R., Chow, F., Overy, R., & Standing, J. (2005). *ICP design methods for driven piles in sands and clays*. Thomas Telford Publishing.

Jovičić, V., & Coop, M. R. (1997, June). Stiffness of coarse-grained soils at small strains. *Géotechnique*, *47*(3), 545–561.

Kassab, C. M., Brickles, S. L., Licht, K. J., & Monaghan, G. W. (2017). Exploring the use of zircon geochronology as an indicator of Laurentide Ice Sheet till provenance, Indiana, USA. *Quaternary Research*, *88*(3), 525–536. https://doi.org/10.1017/qua.2017.71

Kilibarda, Z., & Blockland, J. (2011). Morphology and origin of the Fair Oaks Dunes in NW Indiana, USA. *Geomorphology*, *125*(2), 305–318.

Kilibarda, Z., & Shillinglaw, C. (2014). A 70 year history of coastal dune migration and beach erosion along the southern shore of Lake Michigan. *Aeolian Research*, *17*, 263–273.

Kim, D., Chung, M., & Kwak, K. (2011). Resistance factor calculations for LRFD of axially loaded driven piles in sands. *KSCE Journal of Civil Engineering*, *15*(7), 1185–1196.

Kim, D., & Kang, S.-S. (2013). Engineering properties of compacted loesses as construction materials. *KSCE Journal of Civil Engineering*, *17*(2), 335–341.

Kim, D., & Lee, J. (2012). Resistance factor contour plot analyses of load and resistance factor design of axially-loaded driven piles in clays. *Computers and Geotechnics*, *44*, 9–19.

Kim, D., & Salgado, R. (2012a). Load and resistance factors for external stability checks of mechanically stabilized earth walls. *Journal of Geotechnical and Geoenvironmental Engineering*, *138*(3), 241–251.

Kim, D., & Salgado, R. (2012b). Load and resistance factors for internal stability checks of mechanically stabilized earth walls. *Journal of Geotechnical and Geoenvironmental Engineering*, *138*(8), 910–921.

Kim, K. K., Prezzi, M., & Salgado, R. (2006). *Interpretation of cone penetration tests in cohesive soils* (Joint Transportation Research Program Publication FHWA/IN/JTRP-2006/22). West Lafayette, IN: Purdue University. https://doi.org/10.5703/1288284313387

Kim, K., Prezzi, M., Salgado, R., & Lee, W. (2008, August). Effect of penetration rate on cone penetration resistance in saturated clayey soils. *Journal of Geotechnical and Geoenvironmental Engineering*, *134*(8), 1142–1153.

Kirkgard, M., & Lade, P. (1991). Anisotropy of normally consolidated San Francisco Bay Mud. *Geotechnical Testing Journal*, *14*(3), 231–246.

Krinitzsky, E. L., & Turnbull, W. J. (1967). *Loess deposits of Mississippi* (Geological Society of America Special Paper No. 94). Geological Society of America.

Krumbein, W. C., & Sloss, L. L. (1951). *Stratigraphy and sedimentation*. W. H. Freeman and Company.

Kulhawy, F. H., & Mayne, P. W. (1990, August). *Manual on estimating soil properties for foundation design* (Report EPRI EL-6800). Cornell University Geotechnical Engineering Group.

Ladd, C. C., & Edgers, L. (1972, July). *Consolidated-undrained direct-simple shear tests on saturated clay* (Research Report No. R72-82). MIT Department of Civil Engineering.

Ladd, C. C., Foott, R., Ishihara, K., Schlosser, F., & Poulos, H. G. (1977). Stress deformation and strength characteristics. *Proceedings of the 9th International Conference on Soil Mechanics and Foundation Engineering*, *2*, 421–494.

Ladd, C. C., & Varallyay, J. (1965, July 1). *The influence of the stress system on the behavior of saturated clays during undrained shear* (Research Report No. R65-11). Department of Civil Engineering, MIT.

Lee, J., Eun, J., Prezzi, M., & Salgado, R. (2008). Strain influence diagrams for settlement estimation of both isolated and multiple footings in sand. *Journal of Geotechnical and Geoenvironmental Engineering*, *134*(4), 417–427.

Lee, J., & Salgado, R. (2002). Estimation of footing settlement in sand. *International Journal of Geomechanics*, *2*(1), 1–28.

Lee, J., & Salgado, R. (2005, April). Estimation of bearing capacity of circular footings on sands based on cone penetration test. *Journal of Geotechnical and Geoenvironmental Engineering*, *131*(4), 442–452.

Lehane, B., Liu, Z., Bittar, E., Nadim, F., Lacasse, S., Jardine, R., Carotenuto, P., Rattley, M., Jeanjean, P., Gavin, K.,

Gilbert, R., Bergan-Haavik, J., & Morgan, N. (2020). In Z. Westgate (Ed.), A new 'unified' CPT-based axial pile capacity design method for driven piles in sand. *Proceedings of 4th International Symposium on Frontiers in Offshore Geotechnics (ISFOG 2020)* (pp. 462–477).

Lehane, B. M. (2013). Relating foundation capacity in sands to CPT q_c. In R. Q. Coutinho & P. W. Mayne (Eds.), Proceedings of the Fourth International Conference on Cite Characterization*: Geotechnical and Geophysical Site Characterization 4*, *1*, 63–81. Taylor & Francis.

Lehane, B. M. (2019). CPT-based design of foundations. *Australian Geomechanics Journal*, *54*(4), 23–48.

Lehane, B. M., Jardine, R. J., Bond, A. J., & Frank, R. (1993). Mechanisms of shaft friction in sand from instrumented pile tests. *Journal of Geotechnical Engineering*, *119*(1), 19–35.

Lehane, B. M., Li, Y., & Williams, R. (2013, February). Shaft capacity of displacement piles in clay using the cone penetration test. *Journal of Geotechnical and Geoenvironmental Engineering*, *139*(2), 253–266.

Lehane, B. M., Lim, J. K., Carotenuto, P., Nadim, F., Lacasse, S., Jardine, R. J., & van Dijk, B. (2017, September). Characteristics of unified databases for driven piles. *Proceedings of the 8th International Conference of Offshore Site Investigation and Geotechnics: Smarter Solutions for Offshore Developments*, *1*, 162–191. Society for Underwater Technology (SUT).

Lehane, B. M., Schneider, J. A., & Xu, X. (2005). The UWA-05 method for prediction of axial capacity of driven piles in sand. In M. J. Cassidy & S. Gourvenec (Eds.), *Proceedings of the International Symposium on Frontiers in Offshore Geotechnics* (pp. 683–689).

Lehane, B. M., Schneider, J. A., & Xu, X. (2007). CPT-based design of displacement piles in siliceous sands. In Y. Kikuchi, M. Kimura, J. Otani, & Y. Morikawa (Eds.), *Advances in Deep Foundations* (pp. 69–86). CRC Press.

Lings, M. L., & Dietz, M. S. (2004, May). An improved direct shear apparatus for sand. *Géotechnique*, *54*(4), 245–256.

Liu, Q., & Lehane, B. M. (2021, May). A centrifuge investigation of the relationship between the vertical response of footings on sand and CPT end resistance. *Géotechnique*, *71*(5), 455–465.

Logan, W. N., Cumings, E. R., Malott, C. A., Visher, S. S., Tucker, W. M., & Reeves, J. R. (1922). *Handbook of Indiana Geology* (Publication No. 21). Department of Conservation.

Look, B. (2016). The SPT N-value errors examined with digital technology. In B. M. Lehane, H. E. Acosta-Martínez, & R. Kelley (Eds.), *Geotechnical and Geophysical Site Characterization 5*, *1*, 333–338. Australian Geomechanics Society.

Look, B. G., Seidel, J. P., Sivakumar, S. T., & Welikala, D. L. C. (2015). Real time monitoring of SPT using a PDM device–the failings of our standard test revealed. *Proceedings of International Conference on Geotechnical Engineering (ICGE)* (pp. 435–438).

Loope, H. M., Antinao, J. L., Monaghan, G. W., Autio, R. J., Curry, B. B., Grimley, D. A., Huot, S., Lowell, T. V., & Nash, T. A. (2018). At the edge of the Laurentide ice sheet: Stratigraphy and chronology of glacial deposits in central Indiana. In L. J. Florea (Ed.), *Ancient Oceans, Orogenic Uplifts, and Glacial Ice: Geologic Crossroads in America's Heartland*, Geological Society of America Field Guide, *51*, 245–258.

Loukidis, D. (2006). *Advanced constitutive modeling of sands and applications to foundation engineering* [Doctoral dissertation, Purdue University]. Purdue e-Pubs. https://docs.lib.purdue.edu/dissertations/AAI3232127/

Loukidis, D., & Salgado, R. (2009). Modeling sand response using two-surface plasticity. *Computers and Geotechnics*, *36*(1–2), 166–186.

Loukidis, D., & Salgado, R. (2011). Effect of relative density and stress level on the bearing capacity of footings on sand. *Géotechnique*, *61*(2), 107–119.

Lunne, T., Robertson, P. K., & Powell, J. J. M. (1997). *Cone Penetration Testing in Geotechnical Practice*. Blakie Academic and Professional.

Lupini, J. F. (1980). *The residual strength of soils* [Doctoral dissertation, Imperial College]. http://hdl.handle.net/10044/1/11442

Lupini, J. F., Skinner, A. E., & Vaughan, P. R. (1981). The drained residual strength of cohesive soils. *Géotechnique*, *31*(2), 181–213.

Lyamin, A. V., Salgado, R., Sloan, S. W., & Prezzi, M. (2007). Two- and three-dimensional bearing capacity of footings in sand. *Géotechnique*, *57*(8), 647–662.

Madhav, M. R., & Abhishek, S. V. (2016). Ground versus soil: A new paradigm in geotechnical engineering education. *Proceedings of the International Conference on Geo-Engineering Education (TC 306)–Shaping the Future of Geotechnical Education (SFGE)*. https://doi.org/10.20906/CPS/SFGE-09-0002

Madhav, M. R., & Abhishek, S. V. (2017). A non-mechanistic perspective of geotechnical engineering. *Proceedings of the International Convention on Civil Engineering (ICCE)* (pp. 7–18).

Madhira, M., & Sakleshpur, V. A. (2018). Geotechnics of soft ground. In A. Krishna, A. Dey, & S. Sreedeep (Eds.), *Geotechnics for Natural and Engineered Sustainable Technologies* (pp. 27–44). Springer.

Madhira, M., & Sakleshpur, V. A. (2019). Mining geotechnical parameters from the ground. *8th Annual Praphulla Kumar Lecture* (pp. 1–35). Indian Geotechnical Society (Kochi Chapter).

Maksimović, M. (1989). On the residual shearing strengh of clays. *Géotechnique*, *39*(2), 347–351.

Malott, C. A. (1922). The physiography of Indiana. In W. N. Logan, E. R. Cumings, C. A. Malott, S. S. Visher, W. M. Tucker, & J. R. Reeves (Eds.), *Handbook of Indiana Geology* (Publication No. 21, Part 2, pp. 59–256). Indiana Department of Conservation.

Martin, C. M. (2004, October). *User guide for ABC: Analysis of bearing capacity* (OUEL Report No. 2261/03). University of Oxford.

Martin, C. M. (2005). Exact bearing capacity calculations using the method of characteristics. *Proceedings of 11th International Conference of IACMAG*, *4*, 441–450.

Mayne, P. W. (2007). *Cone penetration testing: A synthesis of highway practice* (NCHRP Synthesis Report 368). Transportation Research Board.

Mayne, P. W., & Campanella, R. G. (2005). Versatile site characterization by seismic piezocone. *Proceedings of 16th International Conference on Soil Mechanics and Geotechnical Engineering* (pp. 721–724). International Society for Soil Mechanics and Geotechnical Engineering.

Mayne, P. W., & Dasenbrock, D. (2018). Direct CPT method for 130 footings on sands. In X. Zhang, P. J. Cosentino, & M. H. Hussein (Eds.), Proceedings of IFCEE 2018*: Innovations in Geotechnical Engineering*, *GSP 299*, 135–146. American Society of Civil Engineers.

Mayne, P. W., & Harris, D. E. (1993). *Axial load-displacement behavior of drilled shaft foundations in Piedmont residuum* (Report No. 41-30-2175). Federal Highway Administration.

Mayne, P. W., & Peuchen, J. (2018). Evaluation of CPTU N_{kt} cone factor for undrained strength of clays. In M. A. Hicks, F. Pisanò, & J. Peuchen (Eds.), *Proceedings of the 4th International Symposium on Cone Penetration Testing* (pp. 423–429). CRC Press.

Mayne, P. W., Uzielli, M., & Illingworth, F. (2012). Shallow footing response on sands using a direct method based on cone penetration tests. *Proceedings of GeoCongress 2012* (pp. 664–679). American Society for Civil Engineers.

Mayne, P. W., & Woeller, D. J. (2014). Generalized direct CPT method for evaluating footing deformation response and capacity on sands, silts, and clays. *Proceedings of Geo-Congress 2014*, *GSP 234*, 1983–1997.

McKnight, T., Cho, Y. M., Townsend, T. G., & Choate, A. (2015). Cone penetration testing for characterizing land-filled municipal solid waste. *Journal of Geotechnical and Geoenvironmental Engineering*, *141*(3), 06014018.

Meehan, C. L. (2006). *An experimental study of the dynamic behavior of slickensided surfaces* [Doctoral dissertation, Virginia Polytechnic Institute and State University]. VTechWorks. http://hdl.handle.net/10919/26074

Meyerhof, G. G. (1956). Penetration tests and bearing capacity of cohesionless soils. *Journal of the Soil Mechanics and Foundations Division*, *82*(1), 1–19.

Mitchell, J. K. (1988, March). New developments in penetration tests and equipment. In J. de Ruiter (Ed.), *Proceedings of the 1st International Symposium on Penetration Testing*, 245–261. A. A. Balkema.

Mitchell, J. K., & Soga, K. (2005). *Fundamentals of soil behavior* (3rd ed.). John Wiley & Sons.

Mondelli, G., Giacheti, H., & Howie, J. (2010). Interpretation of resistivity piezocone tests in a contaminated municipal solid waste disposal site. *Geotechnical Testing Journal*, *33*(2), 123–136.

Munfakh, G., Arman, A., Collin, J. G., Hung, J. C. J., & Brouillette, R. P. (2001). *Shallow foundations reference manual* (Publication No. FHWA-NHI-01-023). Federal Highway Administration.

Murthy, T. G., Loukidis, D., Carraro, J. A. H., Prezzi, M., & Salgado, R. (2007). Undrained monotonic response of clean and silty sands. *Géotechnique*, *57*(3), 273–288.

Niazi, F. S., & Mayne, P. W. (2016). CPTu-based enhanced UniCone method for pile capacity. *Engineering Geology*, *212*, 21–34.

Niazi, F. S., Mayne, P. W., & Woeller, D. J. (2010). Drilled shaft O-cell response at Golden Ears Bridge from seismic piezocone tests. *The Art of Foundation Engineering Practice Congress* (pp. 452–469). http://dx.doi.org/10.1061/41093(372)22

Nishimura, S. (2005). *Laboratory study on anisotropy of natural London clay* [Doctoral dissertation, Imperial College].

Nottingham, L. C., & Schmertmann, J. H. (1975). *An investigation of pile capacity design procedures* (Engineering and Industrial Experiment Station Final Report D629). University of Florida Department of Civil Engineering.

Paik, K., Salgado, R., Lee, J., & Kim, B. (2003, April). Behavior of open- and closed-ended piles driven into sands. *Journal of Geotechnical and Geoenvironmental Engineering*, *129*(4), 296–306.

Paikowsky, S. G., Birgisson, B., McVay, M., Nguyen, T., Kuo, C., Baecher, G., Ayyub, B., Stenersen, K., O'Malley, K., Chernauskas, L., & O'Neill, M. (2004). *Load and resistance factor design (LRFD) for deep foundations* (NCHRP Report 507). Transportation Research Board.

Parry, R. H. G. (1960, December). Triaxial compression and extension tests on remoulded saturated clay. *Géotechnique*, *10*(4), 166–180.

Phoon, K.-K., & Kulhawy, F. H. (1999a). Characterization of geotechnical variability. *Canadian Geotechnical Journal*, *36*(4), 612–624.

Phoon, K.-K., & Kulhawy, F. H. (1999b). Evaluation of geotechnical property variability. *Canadian Geotechnical Journal*, *36*(4), 625–639.

Powers, M. C. (1953, June). A new roundness scale for sedimentary particles. *Journal of Sedimentary Research*, *23*(2), 117–119.

Prandtl, L. (1920). Über die Härte Plastischer Körper. *Nachrichten von der Gesellschaft der Wissenschaften zu Göttingen, Mathematisch-Physikalische Klasse*, *12*, 74–85.

Prandtl, L. (1921). Eindringungsfestigkeit und Festigkeit von Schneiden. *Zeitschrift für Angewandte Mathematik und Mechanik*, *1*(1), 15–20.

Rahman, S., Salgado, R., Prezzi, M., & Becker, P. J. (2020). *Improvement of stiffness and strength of backfill soils through optimization of compaction procedures and specifications* (Joint Transportation Research Program Publication No. FHWA/IN/JTRP-2020/16). West Lafayette, IN: Purdue University. https://doi.org/10.5703/1288284317134

Ramsey, N., Jardine, R., Lehane, B., & Ridley, A. (1998). A review of soil-steel interface testing with the ring shear apparatus. *Offshore Site Investigation and Foundation Behaviour: New Frontiers–Proceedings of an International Conference*, *1*, 237–258. Society for Underwater Technology (SUT).

Randolph, M. F. (2003, December). Science and empiricism in pile foundation design. *Géotechnique*, *53*(10), 847–875.

Randolph, M. F., Dolwin, J., & Beck, R. (1994). Design of driven piles in sand. *Géotechnique*, *44*(3), 427–448.

Reissner, H. (1924). Zum erddruckproblem. *Proceedings of the 1st International Congress of Applied Mechanics* (pp. 295–311).

René, R. M., & Stanonis, F. L. (1995). Reflection seismic profiling of the Wabash Valley fault system in the Illinois Basin (U.S. Geological Survey Professional Paper 1538-O). In K. M. Shedlock & A. C. Johnston (Eds.), *Investigations of the New Madrid Seismic Zone.*

Riemer, M. F., Seed, R. B., Nicholson, P. G., & Jong, H.-L. (1990). Steady state testing of loose sands: Limiting minimum density. *Journal of Geotechnical Engineering*, *116*(2), 332–337.

Robertson, P. K. (1990). Soil classification using the cone penetration test. *Canadian Geotechnical Journal*, *27*(1), 151–158.

Robertson, P. K. (2016). Cone penetration test (CPT)-based soil behaviour type (SBT) classification system—an update. *Canadian Geotechnical Journal*, *53*(12), 1910–1927.

Robertson, P. K., Campanella, R. G., Gillespie, D., & Greig, J. (1986, June). Use of piezometer cone data. *Use of In-Situ Testing in Geotechnical Engineering*, *GSP 6*, 1263–1280. American Society of Civil Engineers.

Robertson, P. K., Campanella, R. G., & Wightman, A. (1983). SPT-CPT correlations. *Journal of Geotechnical Engineering*, *109*(11), 1449–1459.

Rodríguez, J. M., Johansson, J. M. A., & Edeskär, T. (2012). Particle shape determination by two-dimensional image analysis in geotechnical engineering. *Proceedings of Nordic Conference on Soil Mechanics and Geotechnics* (pp. 207–218). Danish Geotechnical Society.

de Ruiter, J., & Beringen, F. L. (1979). Pile foundations for large North Sea structures. *Marine Geotechnology*, *3*(3), 267–314.

Rupp, J. A. (1991). *Structure and isopach maps of the Paleozoic rocks of Indiana* (Indiana Geological Survey Special Report 48). Indiana Geological Survey.

Rutledge, E. M., Guccione, M. J., Markewich, H. W., Wysocki, D. A., & Ward, L. B. (1996, December). Loess stratigraphy of the Lower Mississippi Valley. *Engineering Geology*, *45*(1–4), 167–183.

Salgado, R. (2006). The role of analysis in non-displacement pile design. In W. Wu & H. S. Yu (Eds.), *Modern Trends in Geomechanics*, *106*, 521–540. Springer.

Salgado, R. (2008). *The engineering of foundations* (1st ed.). McGraw-Hill.

Salgado, R. (2013). The mechanics of cone penetration: contributions from experimental and theoretical studies. R. Q. Coutinho & P. W. Mayne (Eds.), *Geotechnical and Geophysical Site Characterization 4*, *1*, 131–153. CRC Press.

Salgado, R. (2014). Experimental research on cone penetration resistance. *Geo-Congress 2014 Keynote Lecture*, *GSP 235*, 140–163. American Society of Civil Engineers.

Salgado, R., Bandini, P., & Karim, A. (2000). Shear strength and stiffness of silty sand. *Journal of Geotechnical and Geoenvironmental Engineering*, *126*(5), 451–462.

Salgado, R., Ganju, E., & Prezzi, M. (2019). Site variability analysis using cone penetration test data. *Computers and Geotechnics*, *105*, 37–50.

Salgado, R., & Kim, D. (2014). Reliability analysis of load and resistance factor design of slopes. *Journal of Geotechnical and Geoenvironmental Engineering*, *140*(1), 57–73.

Salgado, R., Lyamin, A. V., Sloan, S. W., & Yu, H. S. (2004). Two-and three-dimensional bearing capacity of foundations in clay. *Géotechnique*, *54*(5), 297–306.

Salgado, R., & Prezzi, M. (2007). Computation of cavity expansion pressure and penetration resistance in sands. *International Journal of Geomechanics*, *7*(4), 251–265.

Salgado, R., & Prezzi, M. (2014, September–December). Penetration rate effects on cone resistance: Insights from calibration chamber and field testing. *Soils and Rocks*, *37*(3), 233–242.

Salgado, R., Prezzi, M., & Ganju, E. (2015). *Assessment of site variability from analysis of cone penetration test data* (Joint Transportation Research Program Publication No. FHWA/IN/JTRP-2015/04). West Lafayette, IN: Purdue University. https://doi.org/10.5703/1288284315523

Salgado, R., Woo, S. I., & Kim, D. (2011). *Development of load and resistance factor design for ultimate and serviceability limit states of transportation structure foundations* (Joint Transportation Research Program Publication No. FHWA/IN/JTRP-2011/03). West Lafayette, IN: Purdue University. https://doi.org/10.5703/1288284314618

Schmertmann, J. H. (1970). Static cone to compute static settlement over sand. *Journal of the Soil Mechanics and Foundations Division*, *ASCE*, *96*(3), 1011–1043.

Schmertmann, J. H. (1978, July). *Guidelines for cone penetration test (performance and design)* (Report No. FHWA-TS-78-209). Federal Highway Administration.

Schmertmann, J. H., Hartmann, J. P., & Brown, P. R. (1978). Improved strain influence factor diagrams. *Journal of the Geotechnical Engineering Division*, *104*(8), 1131–1135.

Schneider, J. A., Xu, X., & Lehane, B. M. (2008). Database assessment of CPT-based design methods for axial capacity of driven piles in siliceous sands. *Journal of Geotechnical and Geoenvironmental Engineering*, *134*(9), 1227–1244.

Shaw, E. W. (1915). On the origin of the Loess of southwestern Indiana. *Science*, *41*(1046), 104–108.

Skempton, A. W. (1951). The bearing capacity of clays. *Building Research Congress*, *1*, 180–189.

Skempton, A. W. (1985, March). Residual strength of clays in landslides, folded strata and the laboratory. *Géotechnique*, *35*(1), 3–18.

Skempton, A. W. (1986). Standard penetration test procedures and the effects in sands of overburden pressure, relative density, particle size, ageing and overconsolidation. *Géotechnique*, *36*(3), 425–447.

Skempton, A. W., & Bjerrum, L. (1957). A contribution to the settlement analysis of foundations on clay. *Géotechnique*, *7*(4), 168–178.

Skempton, A. W., & MacDonald, D. H. (1956). The allowable settlements of buildings. *Proceedings of the Institution of Civil Engineers*, *5*(6), 727–768.

Sladen, J. A., D'Hollander, R. D., & Krahn, J. (1985). The liquefaction of sands, a collapse surface approach. *Canadian Geotechnical Journal*, *22*(4), 564–578.

Song, C. R., Kim, S., Bekele, B., Zhang, J., & Silvey, A. (2019). *CPT-based pile design* (Report No. SPR-P1 M076). Nebraska Department of Transportation.

Sukumaran, B., & Ashmawy, A. K. (2001). Quantitative characterisation of the geometry of discret particles. *Géotechnique*, *51*(7), 619–627.

Tehrani, F. S., Arshad, M. I., Prezzi, M., & Salgado, R. (2018). Physical modeling of cone penetration in layered sand. *Journal of Geotechnical and Geoenvironmental Engineering*, *144*(1), 04017101.

Terzaghi, K. (1943). *Theoretical soil mechanics*. John Wiley & Sons.

Terzaghi, K., Peck, R. B., & Mesri, G. (1996, February). *Soil mechanics in engineering practice* (3rd ed.). Wiley.

Thurairajah, A. (1962). *Some shear properties of kaolin and of sand* [Doctoral dissertation, University of Cambridge].

Tippett, L. H. C. (1925). On the extreme individuals and the range of samples taken from a normal population. *Biometrika*, *17*(3/4), 364–387. Oxford University Press.

Tsomokos, A., & Georgiannou, V. N. (2010). Effect of grain shape and angularity on the undrained response of fine sands. *Canadian Geotechnical Journal*, *47*(5), 539–551.

Tumay, M. (1985). *Field calibration of electric cone penetrometers in soft soils* (Publication No. FHWA/LA/LSU-GE-85/02). Federal Highway Administration.

Tumay, M. T., & Fakhroo, M. (1982). *Friction pile capacity prediction in cohesive soils using electric quasi-static penetration tests* (Interim Research Report No. 1). Louisiana Department of Transportation and Development, Research and Development.

USACE. (2001, January 1). *Engineer manual: Engineering and design – geotechnical investigations* (Publication No. EM 1110-1-1804). U.S. Army Corps of Engineers.

USGS. (n.d.). *United states geological survey – earthquake hazards program* [Data set]. https://earthquake.usgs.gov/research/cpt/data/txt/VHC028.txt

Uthayakumar, M., & Vaid, Y. P. (1998). Static liquefaction of sands under multiaxial loading. *Canadian Geotechnical Journal*, *35*(2), 273–283.

Verdugo, R., & Ishihara, K. (1996). The steady state of sandy soils. *Soils and Foundations*, *36*(2), 81–91.

Viggiani, G., & Atkinson, J. H. (1995). Stiffness of fine-grained soil at very small strains. *Géotechnique*, *45*(2), 249–265.

Wadell, H. (1932). Volume, shape, and roundness of rock particles. *The Journal of Geology*, *40*(5), 443–451.

Wadell, H. (1933). Sphericity and roundness of rock particles. *The Journal of Geology*, *41*(3), 310–331.

Walker, G., Jefferies, N., Lennard, M., & Lightfoot, J. (2009). Cone penetration testing of radiologically contaminated burial trenches. *Proceedings of the 12th International Conference on Environmental Remediation and Radioactive Waste Management*, 475–486.

Wayne, W. J. (1965). *The Crawfordsville and Knightstown moraines in Indiana* (Indiana Geological Survey Report of Progress 28). Indiana Geological Survey.

Wayne, W. J., & Thornbury, W. D. (1951). *Glacial geology of Wabash County, Indiana*. (Indiana Geological Survey Bulletin 5). Indiana Geological Survey.

Weary, D. J., & Doctor, D. H. (2014). *Karst in the United States: A digital map compilation and database* (U.S. Geological Survey Open-File Report 2014-1156). https://pubs.er.usgs.gov/publication/ofr20141156#:~:text=https%3A//doi.org/10.3133/ofr20141156

West, T. R. (2010). *Geology applied to engineering*. Waveland Press.

White, D. J., & Lehane, B. M. (2004). Friction fatigue on displacement piles in sand. *Géotechnique*, *54*(10), 645–658.

White, W. B. (1988, May). *Geomorphology and hydrology of karst terrains*. Oxford University Press.

Wilcox, D. A., Shedlock, R. J., & Hendrickson, W. H. (1986). Hydrology, water chemistry and ecological relations in the raised mound of Cowles Bog. *Journal of Ecology*, *74*(4), 1103–1117.

Wilcox, D. A., & Simonin, H. A. (1988, June). The stratigraphy and development of a floating peatland, Pinhook Bog, Indiana. *Wetlands*, *8*(1), 75–91.

Wilson, J. (2008). *How the Ice Age shaped Indiana* (2nd ed.). Wilstar Media.

Woolery, E. W., Whitt, J. W., Van Arsdale, R. B., & Almayahi, A. (2018). Geophysical and geological evidence for quaternary displacement on the caborn fault, Wabash Valley fault system, southwestern Indiana. *Seismological Research Letters*, *89*(6), 2473–2480.

Wroth, C. P. (1979). Correlations of some engineering properties of soils. *Proceedings of the 2nd International Conference on Behaviour of Offshore Structures*, *1*, 121–132.

Wroth, C. P. (1984). The interpretation of in situ soil tests. *Géotechnique*, *34*(4), 449–489.

Wroth, C. P., & Wood, D. M. (1978). The correlation of index properties with some basic engineering properties of soils. *Canadian Geotechnical Journal*, *15*(2), 137–145.

Xiao, T., Li, D.-Q., Cao, Z.-J., & Zhang, L.-M. (2018). CPT-based probabilistic characterization of three-dimensional spatial variability using MLE. *Journal of Geotechnical and Geoenvironmental Engineering*, *144*(5), 04018023.

Xu, X. (2007). *Investigation of the end bearing performance of displacement piles in sand* [Doctoral dissertation, The University of Western Australia].

Xu, X., & Lehane, B. M. (2008, April). Pile and penetrometer end bearing resistance in two-layered soil profiles. *Géotechnique*, *58*(3), 187–197.

Xu, X., Schneider, J. A., & Lehane, B. M. (2008). Cone penetration test (CPT) methods for end-bearing assessment of open- and closed-ended driven piles in siliceous sand. *Canadian Geotechnical Journal*, *45*(8), 1130–1141.

Yang, J., & Wei, L. M. (2012). Collapse of loose sand with the addition of fines: the role of particle shape. *Géotechnique*, *62*(12), 1111–1125.

Yang, Z. X., Jardine, R. J., Zhu, B. T., Foray, P., & Tsuha, C. H. C. (2010). Sand grain crushing and interface shearing during displacement pile installation in sand. *Géotechnique*, *60*(6), 469–482.

Zheng, J., & Hryciw, R. D. (2015). Traditional soil particle sphericity, roundness and surface roughness by computational geometry. *Géotechnique*, *65*(6), 494–506.

Zheng, J., & Hryciw, R. D. (2016). Index void ratios of sands from their intrinsic properties. *Journal of Geotechnical and Geoenvironmental Engineering*, *142*(12), 06016019.

APPENDICES

Appendix A. Critical-State Friction Angle of Sand

Appendix B. OCR and K_0 of Soil

Appendix C. Iterative Scheme for Footing Settlement in Sand

Appendix D. Penetration Rate Effect on Cone Resistance

Appendix E. Residual-State Friction Angle of Clay

APPENDIX A. CRITICAL-STATE FRICTION ANGLE OF SAND

The critical-state friction angle ϕ_c is simply the friction angle that a given soil has at critical state. It is independent of soil state (i.e., relative density and confining stress) but depends on particle size (e.g., D_{50}), morphology (e.g., roundness R and sphericity S), mineralogy (e.g., silicates versus carbonates), and gradation (e.g., coefficient of uniformity C_U) (Han et al., 2018; Salgado, 2008). The value of ϕ_c for a silica sand typically ranges from 28°–36°; sands with rounded, smooth particles with a poorly-graded particle size distribution have values near the low end of this range, while sands with angular, rough particles with a well-graded particle size distribution have values near the high end of this range (Salgado, 2008). In contrast, the value of ϕ_c for a carbonate sand typically ranges from 37°–44° (Altuhafi et al., 2016; Coop & Lee, 1993; Salgado, 2008).

A.1 Roundness

Roundness is a measure of sharpness of the particle corners (Figure A.1). It is defined as the ratio of the average radius of curvature of the corners of a 2D projection of the particle to the radius r_{ins} of the largest inscribed circle for the same projection (Wadell, 1932):

$$R = \frac{\sum_{i=1}^{N} \frac{r_i}{N}}{r_{ins}} \qquad \text{(Eq. A.1)}$$

where r_i = radius of curvature of corner i of the particle, and N = number of particle corners. Table A.1 summarizes the different roundness classes proposed by Powers (1953).

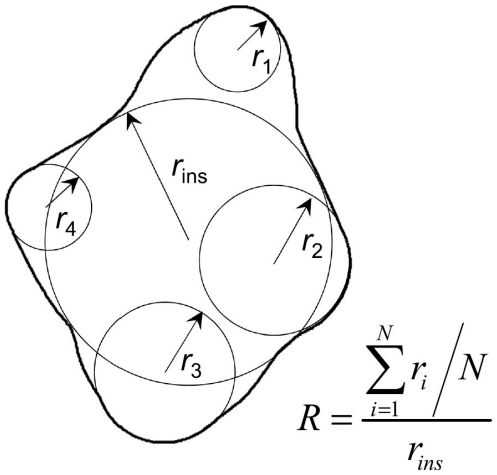

Figure A.1 Definition of roundness for a 2D projected outline of a particle (Hryciw et al., 2016; Wadell, 1932).

Table A.1 Classification of particles based on roundness (Powers, 1953)

Roundness Class	Roundness Interval	Mean Roundness[1]
Very angular	0.12–0.17	0.14
Angular	0.17–0.25	0.21
Subangular	0.25–0.35	0.30
Subrounded	0.35–0.49	0.41
Rounded	0.49–0.70	0.59
Well-rounded	0.70–1.00	0.84

[1]Geometric mean

A.2 Sphericity

Sphericity is a measure of the extent to which a particle resembles the shape of a sphere. Particle sphericity has been defined in several ways in the literature (Mitchell & Soga, 2005; Rodríguez et al., 2012); three widely used definitions are detailed below.

1. *Diameter sphericity S_D:* It is defined as the ratio of the diameter D_c of a circle having the same area as the projected 2D area of the particle to the diameter D_{cir} of the smallest circle circumscribed about the 2D projection of the particle (Wadell, 1933):

$$S_D = \frac{D_c}{D_{cir}} \qquad \text{(Eq. A.2)}$$

2. *Width-to-length ratio sphericity S_{WL}:* It is defined as the ratio of the width d_2 to the length d_1 of the particle (Zheng & Hryciw, 2015):

$$S_{WL} = \frac{d_2}{d_1} \qquad \text{(Eq. A.3)}$$

   The length d_1 and width d_2 of the particle are defined as the largest and smallest dimensions, respectively, of a rectangle enclosing the particle; the selected rectangle is the one with the largest possible dimension circumscribing the particle. The reciprocal of the width-to-length ratio sphericity is commonly referred to as the elongation ratio.

3. *Perimeter sphericity S_P:* It is defined as the ratio of the perimeter P_c of a circle having the same area as the projected 2D area A of the particle to the projected perimeter P of the particle (Altuhafi et al., 2013):

$$S_P = \frac{P_c}{P} = \frac{2\sqrt{\pi A}}{P} \qquad \text{(Eq. A.4)}$$

Figure A.2 illustrates the definitions of diameter sphericity S_D and width-to-length ratio sphericity S_{WL}. Figure A.3 shows a chart developed by Krumbein and Sloss (1951) with 20 reference particle silhouettes having roundness and sphericity values ranging from 0.1–0.9 and 0.3–0.9, respectively, in increments of 0.2. If access to digital, computer-based tools, such as ImageJ and MATLAB, is limited, the chart can be used to estimate particle roundness and sphericity by comparing the shapes of individual particles viewed under a microscope with the

reference particle silhouettes given in the chart. The sphericity obtained from the Krumbein and Sloss (1951) chart is the width-to-length ratio sphericity S_{WL} (Zheng & Hryciw, 2015).

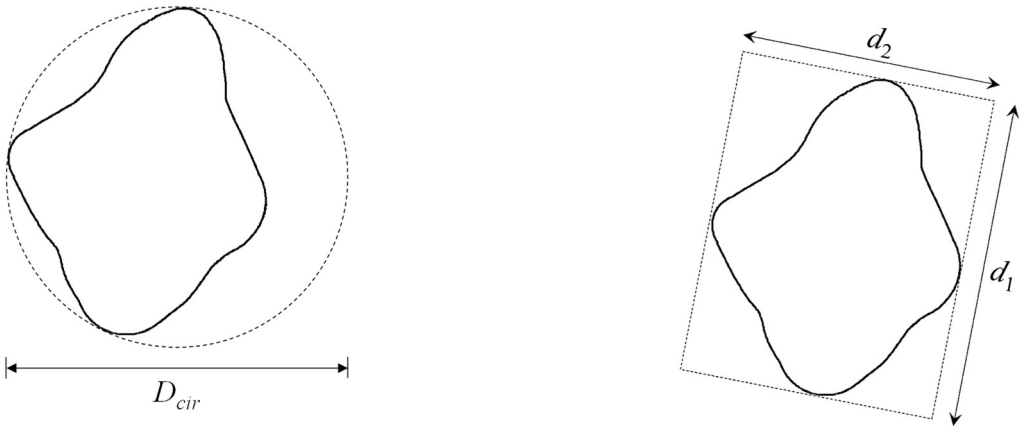

Figure A.2 Illustrations of (a) diameter D_{cir} of the smallest circle circumscribed about the 2D projection of the particle, and (b) length d_1 and width d_2 of the particle.

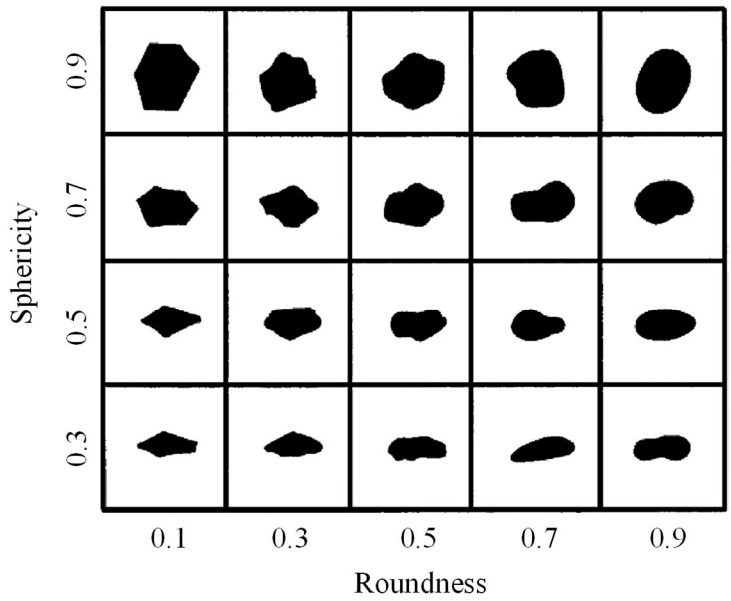

Figure A.3 Chart for estimating roundness and sphericity (Krumbein & Sloss, 1951).

A.3 Silica Sand Database

Table A.2 summarizes the intrinsic parameters of 23 clean silica sands reported in the literature. The parameters include mean particle size D_{50}, coefficient of uniformity C_U, roundness R, sphericity S, minimum void ratio e_{min}, maximum void ratio e_{max}, and critical-state friction angle

ϕ_c in triaxial compression. All the sands are poorly-graded, except FS Ohio SW, which is classified as well-graded according to the Unified Soil Classification System (USCS) (ASTM, 2012). The number designations for some of the uniform sands (e.g., Ottawa 20–30) listed in Table A.2 indicate the sieve numbers between which the sand particles were retained. The D_{50}, C_U, and R values for the sands are in the range of 0.15–2.68 mm (0.006–0.105 in.), 1.2–7.9, and 0.3–0.8, respectively. Although different researchers have defined particle sphericity in different ways for the sands listed in Table A.2, the S values were found to lie within a relatively narrow range of 0.65–0.90 regardless of the definition used. Zheng and Hryciw (2016) also found the S values to lie within a similar range for the sands considered in their database. They reasoned that sand particles are usually bulky in nature and that slender, elongated sand particles are rarely found in practice because such particles are susceptible to breakage.

Table A.2 Intrinsic parameters of 23 clean silica sands reported in the literature

	Gradation		Morphology		Packing		Strength	
Sand	D_{50} (mm)	C_U	R	S	e_{min}	e_{max}	ϕ_c (°)	Reference
FS Ohio 6–10	2.68	1.31	0.43	0.86	0.66	0.92	34.6	Han et al. (2018)
FS Ohio 10–16	1.59	1.30	0.44	0.83	0.65	0.92	33.7	Han et al. (2018)
FS Ohio 16–20	1.01	1.25	0.40	0.78	0.66	0.97	32.9	Han et al. (2018)
FS Ohio 20–40	0.63	1.42	0.39	0.82	0.62	0.91	31.8	Han et al. (2018)
FS Ohio 50–100	0.23	1.56	0.35	0.82	0.63	0.93	31.7	Han et al. (2018)
FS Ohio Coarse	1.50	2.00	—	—	0.45	0.72	33.6	Han et al. (2018)
FS Ohio Fine	0.35	2.00	—	—	0.48	0.72	33.4	Han et al. (2018)
FS Ohio SW	1.04	7.90	—	—	0.37	0.65	33.2[1]	Han et al. (2018)
Fontainebleau NE34	0.21	1.53	0.45	0.75[2]	0.51	0.90	30.0	Altuhafi et al. (2018); Yang et al. (2010); Zheng & Hryciw (2016)
Fraser River	0.30	2.40	0.43	0.83	0.68	1.00	33.0	Gao et al. (2014); Sukumaran & Ashmawy (2001); Uthayakumar & Vaid (1998)
Ham River	0.30	1.59	0.45	0.65[2]	0.59	0.92	32.0	Coop & Lee (1993); Jovičić & Coop (1997); Zheng & Hryciw (2016)
Lausitz	0.25	3.09	0.51	—	0.44	0.85	32.2	Herle & Gudehus (1999); Zheng & Hryciw (2016)
Leighton Buzzard	0.78	1.27	0.75	0.80[2]	0.51	0.80	30.0	Lings & Dietz (2004); Thurairajah (1962); Zheng & Hryciw (2016)
Longstone	0.15	1.43	0.30	0.65[2]	0.61	1.00	32.5	Tsomokos & Georgiannou (2010); Zheng & Hryciw (2016)
M31	0.28	1.54	0.62	0.70[2]	0.53	0.87	30.2	Tsomokos & Georgiannou (2010); Zheng & Hryciw (2016)
Monterey No. 0	0.38	1.58	—	0.89[3]	0.53	0.86	32.8	Altuhafi et al. (2013); Riemer et al. (1990)
Ohio Gold Frac	0.62	1.60	0.43	0.83	0.58	0.87	32.5	Ganju et al. (2020); Han et al. (2018)
Ottawa Graded	0.31	1.89	0.80[4]	0.90[4]	0.49	0.76	29.5	Carraro et al. (2009)
Ottawa 20–30	0.72	1.18	0.72	0.88	0.50	0.74	29.2	Han et al. (2018)
Q-Rok[4]	0.63	1.50	0.40	0.73	0.70	1.03	33.0	Unpublished research
Sacramento River	0.30	1.80	—	0.88[3]	0.53	0.87	33.2	Altuhafi et al. (2013); Riemer et al. (1990)
Ticino	0.58	1.50	0.40	0.80[2]	0.57	0.93	33.0	Altuhafi et al. (2016); Bellotti et al. (1996); Cho et al. (2006);
Toyoura	0.17	1.70	0.35	0.65[2]	0.60	0.98	31.6	Loukidis & Salgado (2009); Verdugo & Ishihara (1996); Zheng & Hryciw (2016)

Note: D_{50} = mean particle size, C_U = coefficient of uniformity (= D_{60}/D_{10}), e_{min} = minimum void ratio, e_{max} = maximum void ratio, R = roundness, S = diameter sphericity S_D (unless otherwise indicated), and ϕ_c = critical-state friction angle in triaxial compression (unless otherwise indicated).
The properties of INDOT No. 4 sand, which is a backfill material typically used for retaining wall construction in Indiana, are: D_{50} = 0.85 mm, C_U = 4.58, R = 0.72, S_{WL} = 0.73, e_{min} = 0.29, e_{max} = 0.54, and ϕ_c = 38.0° in direct shear (Rahman et al., 2020).
[1] Obtained from direct shear test results.
[2] Width-to-length ratio sphericity S_{WL} (Mitchell & Soga, 2005; Zheng & Hryciw, 2015).
[3] Perimeter sphericity S_P (Altuhafi et al., 2013).
[4] Unpublished research.

A.4 Simple Correlation

In the absence of direct shear (DS) or triaxial compression (TXC) test results, a simple approach to critical-state friction angle estimation is to use an equation of the form:

$$\phi_c = C_1 \left(\frac{D_{50}}{D_{\text{ref}}} \right)^{C_2} \left(C_U \right)^{C_3} \left(R \right)^{C_4} \qquad \text{(Eq. A.5)}$$

where D_{ref} = reference particle size (= 1 mm or 0.04 in.); and C_1, C_2, C_3, and C_4 = regression coefficients. The values of C_1, C_2, C_3, and C_4 were obtained by performing a least squares regression in Microsoft Excel. The following equation was found to fit the ϕ_c values reported in Table A.2 quite well:

$$\phi_c (^\circ) = 28.3 \left(\frac{D_{50}}{D_{\text{ref}}} \right)^{\zeta} \left(C_U \right)^{2\zeta} \left(R \right)^{-3\zeta} \qquad \text{(Eq. A.6)}$$

where ϕ_c = critical-state friction angle in triaxial compression, and ζ = exponent (= 0.045). The adjusted coefficient of determination r^2, mean absolute error, and mean absolute percentage error are 0.89, 0.4°, and 1.3%, respectively. The adjusted r^2 is a modified version of r^2 that has been adjusted for the number of independent variables considered in the model. Equation A.6 is applicable for poorly-graded, clean silica sands with D_{50} = 0.15–2.68 mm (0.006–0.105 in.), C_U = 1.2–3.1, and R = 0.3–0.8; however, it should be used with caution for (a) well-graded sands with $C_U \geq 6$, (b) sands with D_{50}, C_U and R values that lie outside these ranges, and (c) sands with plastic or non-plastic fines greater than 5%. Equation A.6 could be further improved through future research.

Figure A.4 compares the critical-state friction angle predicted using Eq. A.6 with that obtained from TXC test results for the poorly-graded, clean silica sands listed in Table A.2. The differences between the predicted and measured ϕ_c values are within 1°. The value of ϕ_c predicted using Eq. A.6 may be decreased by a degree or two, if needed, to obtain a conservative estimate for use in foundation design. However, we re-emphasize that laboratory direct shear or triaxial compression test results provide the best means for estimating the critical-state friction angle of sands, particularly those that contain plastic or non-plastic fines greater than 5% (Carraro et al., 2009; Murthy et al., 2007).

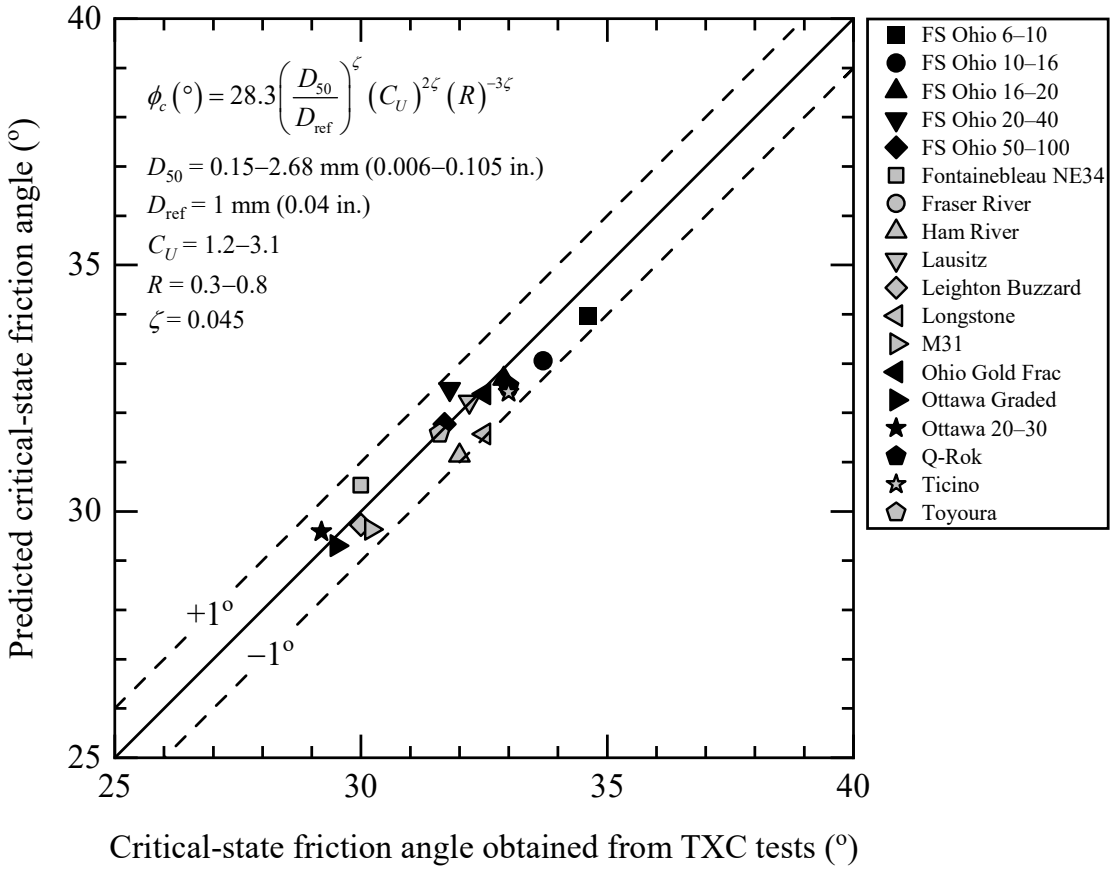

Figure A.4 Comparison of critical-state friction angles obtained from Eq. A.6 and TXC tests on poorly-graded, clean silica sands.

To evaluate the performance of Eq. A.6 in an unbiased manner, a blind test was performed on two additional, poorly-graded, clean silica sands—Nerlerk sand and Fujian sand; these sands were not used in the development of Eq. A.6. The properties of Nerlerk sand are: D_{50} = 0.23 mm (0.009 in.), C_U = 1.56, R = 0.43, S_{WL} = 0.75, e_{min} = 0.66, e_{max} = 0.89, and ϕ_c = 30° in triaxial compression (Sladen et al., 1985); the values of R and S_{WL} are based on Krumbein and Sloss (1951). The properties of Fujian sand are: D_{50} = 0.40 mm (0.016 in.), C_U = 1.53, R = 0.55, and ϕ_c = 30.8° in triaxial compression (Yang & Wei, 2012). The critical-state friction angle of Nerlerk sand and Fujian sand obtained from Eq. A.6 is shown below.

Nerlerk Sand

$$\phi_c = 28.3\left(\frac{D_{50}}{D_{ref}}\right)^{\zeta}(C_U)^{2\zeta}(R)^{-3\zeta} = 28.3\times\left(\frac{0.009}{0.04}\right)^{0.045}\times(1.56)^{0.09}\times(0.43)^{-0.135} = 30.9°$$

Fujian Sand

$$\phi_c = 28.3\left(\frac{D_{50}}{D_{ref}}\right)^{\zeta}(C_U)^{2\zeta}(R)^{-3\zeta} = 28.3\times\left(\frac{0.016}{0.04}\right)^{0.045}\times(1.53)^{0.09}\times(0.55)^{-0.135} = 30.6°$$

The difference between the predicted and measured ϕ_c value is equal to 0.9° for Nerlerk sand and 0.2° for Fujian sand.

A.5 Procedure for Estimation of ϕ_c from Intrinsic Soil Variables

In the absence of direct shear or triaxial compression test results, the critical-state friction angle ϕ_c of a poorly-graded, clean silica sand may be estimated from intrinsic soil variables by following these steps.

1. Perform a sieve analysis test and obtain the particle-size distribution curve.
2. Determine the mean particle size D_{50} and the coefficient of uniformity C_U (= D_{60}/D_{10}) from the particle-size distribution curve.
3. Determine the dominant particle size of the sand (i.e., the sieve size with the maximum percentage by mass of particles retained on the sieve).
4. Select a reasonable number of random particles (say 25 particles) from those retained on the sieve identified in step 3 and place them in an orderly fashion on a flat surface (e.g., glass slide). The number of random particles may be increased or decreased depending on how variable the morphology is from one particle to the next.
5. Execute one of the following methods, based on the desired level of sophistication, to determine particle roundness and sphericity.

   Method 1 (Visual)
   a. Observe the particles through a microscope.
   b. Compare the observed shapes of the particles against the reference particle silhouettes given in the chart by Krumbein and Sloss (1951) (Figure A.3).
   c. Determine the roundness R and sphericity S of each particle and average the values for all the particles selected.

   Method 2 (Computational)
   a. Observe the particles through a microscope and obtain high-resolution images of the particles using a digital camera attached to the microscope.
   b. Analyze the particle images using the software ImageJ (https://imagej.nih.gov/ij/download.html) or the MATLAB code developed by Zheng and Hryciw (2015) (https://www.mathworks.com/matlabcentral/fileexchange/60651-particle-roundness-and-sphericity-computation).
   c. Determine the roundness R and sphericity S of each particle and average the values for all the particles selected.
6. Estimate the critical-state friction angle ϕ_c of the sand using Eq. A.6.

APPENDIX B. OCR AND K_0 OF SOIL

B.1 Overconsolidation Ratio (OCR)

Laboratory consolidation tests, such as the oedometer test or the constant rate of strain (CRS) test, provide the best means of determining the OCR of clays. In addition, the OCR may be known from the site history (e.g., if soil was previously removed or structures were demolished at the site), or it may be deduced from geologic considerations or from *in situ* testing observations. A preliminary estimate of the OCR of clay can be obtained from CPT results using the following approximate correlation (Ladd et al., 1977; Salgado, 2008; Wroth, 1984):

$$\text{OCR} = \max\left\{\left[\frac{\left(s_u/\sigma'_{v0}\right)_{\text{OC}}}{\left(s_u/\sigma'_{v0}\right)_{\text{NC}}}\right]^{1.25}\ ;\ 1\right\} \approx \max\left\{\left[\frac{q_{tn}/N_k}{\left(s_u/\sigma'_{v0}\right)_{\text{NC}}}\right]^{1.25}\ ;\ 1\right\} \qquad \text{(Eq. B.1)}$$

where $(s_u/\sigma'_{v0})_{OC}$ = normalized undrained shear strength of an OC clay; $(s_u/\sigma'_{v0})_{NC}$ = normalized undrained shear strength of the same clay when normally consolidated (≈ 0.2–0.3 for most clays); q_{tn} = normalized cone resistance (= $(q_t - \sigma_{v0})/\sigma'_{v0}$); q_t = corrected, total cone resistance measured under undrained conditions (Eq. 2.1); σ_{v0} and σ'_{v0} = *in situ* vertical total and effective stresses, respectively, at the depth being considered; and N_k = cone factor (≈ 9–15 as long as the CPT is performed at a penetration rate that is sufficiently high to ensure undrained penetration (refer to Appendix D); soft NC clays tend to have N_k values near the low end of this range, while stiff OC clays tend to have N_k values near the high end of this range) (Bisht et al., 2021; Mayne & Peuchen, 2018; Salgado, 2008, 2013, 2014; Salgado et al., 2004). An average N_k value of 12 may be used in Eq. B.1 to obtain a preliminary estimate of the OCR.

The normalized undrained shear strength $(s_u/\sigma'_{v0})_{NC}$ of an NC clay can be estimated using (Wroth, 1984):

$$\left(\frac{s_u}{\sigma'_{v0}}\right)_{\text{NC}} \approx \begin{cases} \dfrac{1.7\sin\phi_c}{3-\sin\phi_c} & \text{for CIUC conditions} \\ \dfrac{\sin\phi_c}{2a}\left(\dfrac{a^2+1}{2}\right)^{\Lambda} & \text{for CK}_0\text{UC conditions} \end{cases} \qquad \text{(Eq. B.2)}$$

$$a = \frac{3-\sin\phi_c}{2\left(3-2\sin\phi_c\right)} \qquad \text{(Eq. B.3)}$$

where CIUC = isotropically-consolidated undrained triaxial compression, CK_0UC = K_0-consolidated undrained triaxial compression, Λ = plastic volumetric strain ratio (≈ 0.8), and ϕ_c = critical-state friction angle (≈ 15°–30° for most clays; high-plasticity clays with high smectite and clay contents tend to have values near the low end of this range, while low-plasticity clays with low smectite and clay contents tend to have values near the high end of this range (refer to Table E.1 of Appendix E)). An alternative expression that provides conservative estimates of $(s_u/\sigma'_{v0})_{NC}$ for both CIUC and CK_0UC test conditions is $(s_u/\sigma'_{v0})_{NC} = \phi_c/100$ (Kulhawy & Mayne, 1990; Salgado, 2008).

The OCR (= σ'_{vp}/σ'_v) of sand may be evaluated based on the geologic history of the site, where σ'_{vp} = preconsolidation stress, which is the maximum vertical effective stress ever

experienced by the soil, and σ'_v = current vertical effective stress. The reader may also refer to Section 2.3.7 of Volume I for additional information on the OCR.

B.2 Coefficient of Lateral Earth Pressure At-Rest K_0

The coefficient of lateral earth pressure at-rest K_0 of soil can be determined using (Brooker & Ireland, 1965):

$$K_0 = K_{0,\mathrm{NC}}\sqrt{\mathrm{OCR}} \qquad \text{(Eq. B.4)}$$

where $K_{0,\mathrm{NC}}$ = value of K_0 if the soil is normally consolidated (= 0.40–0.50 for NC sand, with dense sands tending to have lower values and loose sands having higher values, and 0.50–0.75 for NC clay) (Salgado, 2008; Salgado & Prezzi, 2007), and OCR = overconsolidation ratio, which is equal to 1 for NC soil and greater than 1 for OC soil. The reader may also refer to Section 2.3.9 of Volume I for additional information on K_0.

APPENDIX C. ITERATIVE SCHEME FOR FOOTING SETTLEMENT IN SAND

Because the representative elastic modulus of each sublayer is a function of footing settlement, an iterative scheme is needed if we wish to generate a load-settlement curve for a given footing geometry. Figure C.1 shows the iterative scheme proposed to achieve this objective. An initial guess value for w (= w_{max} established in step 5(c) of Section 3.1) is first chosen, and the representative elastic modulus of each sublayer is then calculated using Eq. 3.12. Next, the footing settlement computed using Eq. 3.14 is compared with the initial guess value. If the convergence criterion of 10^{-5} is satisfied, the value of w obtained from Eq. 3.14 is reported as the footing settlement corresponding to the load acting on the footing. However, if the convergence criterion is not satisfied, the footing settlement obtained from Eq. 3.14 is used as the initial guess value for w in the next iteration. A convergence criterion of 10^{-5} was found to be adequate with respect to accuracy and computational time, and convergence was typically achieved within a few iterations. The iterative scheme can be used to obtain the load-settlement curve of the footing up to a footing settlement w equal to 10% of the footing size B; however, it should not be used to estimate the limit unit bearing capacity q_{bL} of the footing (i.e., the unit load on the footing base that causes the footing to plunge into the ground). The iterations can be performed in Microsoft Excel either by going to *File* → *Options* → *Formulas* and selecting *Enable iterative calculation* in the *Calculation options* tab or by using the *Solver* tool. Note that parameters D_R, E/q_c, and I_z should be calculated for each sublayer within the influence depth z_{f0} below the footing base.

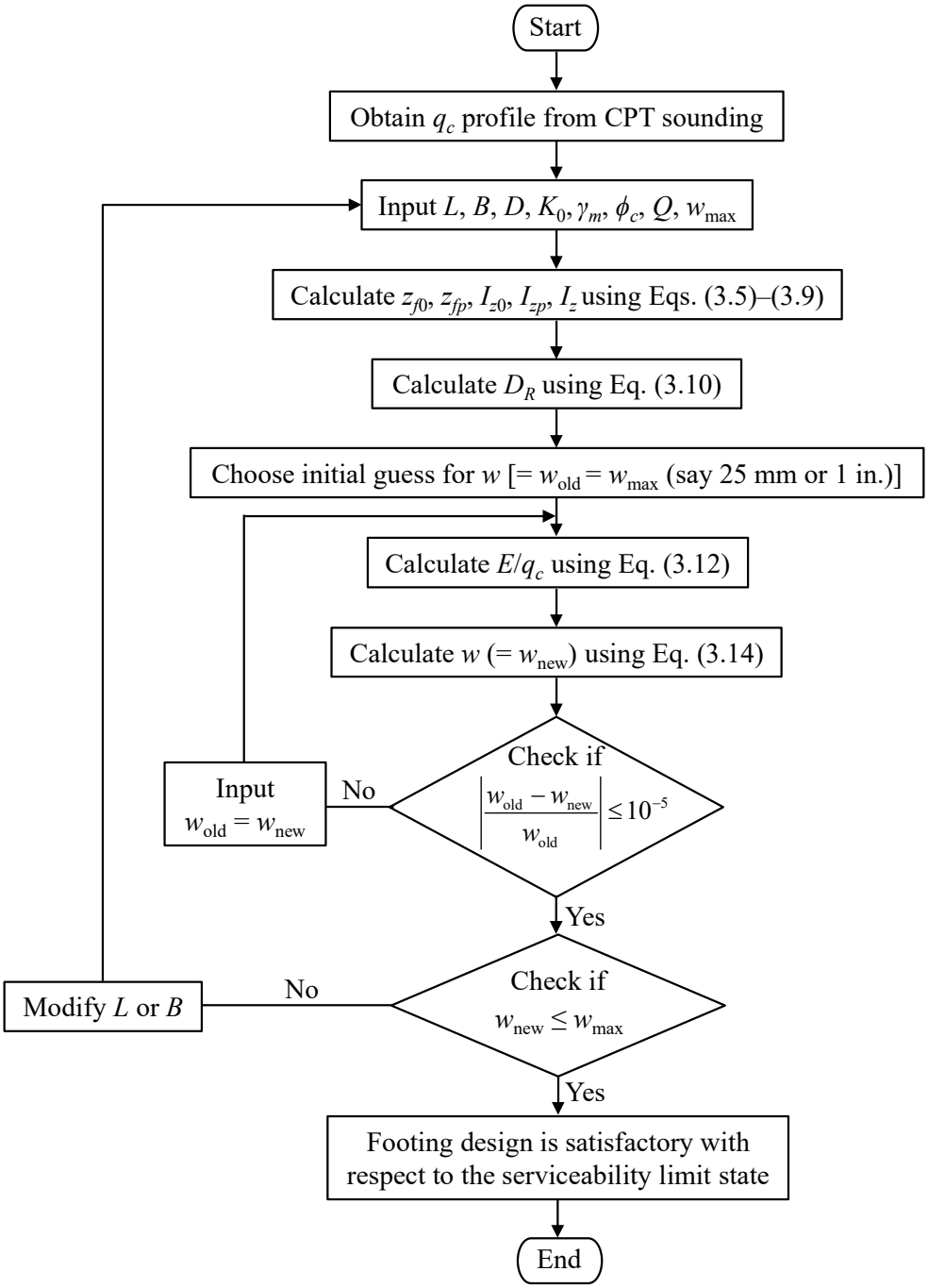

Figure C.1 Iterative scheme for estimation of footing settlement in sand using CPT results.

APPENDIX D. PENETRATION RATE EFFECT ON CONE RESISTANCE

Cone penetration at the standard rate of 2 cm/s (0.8 in./s) is fully drained for clean sand and fully undrained for pure clay. However, for soils containing mixtures of sand, silt, and clay, cone penetration at the standard rate of 2 cm/s (0.8 in./s) may take place under partially drained conditions depending on the ratios of these three broad particle size groups and the fabric of the soil. According to Kim et al. (2008, 2006), the undrained cone resistance is expected to be measured in CPTs performed with the standard cone (d_c = 35.7 mm or 1.4 in.) at the standard rate (v = 2 cm/s or 0.8 in./s) in soils having coefficient of consolidation c_v values less than roughly 10^{-4} m^2/s (0.15 in.^{2}/s). However, if the c_v value of the soil is greater than about 10^{-4} m^2/s (0.15 in.^{2}/s), the CPT sounding should be performed at a faster rate so that the normalized penetration rate V (= vd_c/c_v) is greater than 10 (Salgado & Prezzi, 2014). This approach would be the easiest way to ensure that cone penetration in mixed or intermediate soils takes place under undrained conditions. However, as this is still a topic of ongoing research, the implementation of this approach is optional and not mandatory in INDOT construction projects. The alternative would be to attempt to interpret the results of a CPT sounding actually performed under partial drainage conditions; however, there are no reliable methods for doing that at the present time. The coefficient of consolidation can be determined from the results of laboratory consolidation tests or CPT pore pressure dissipation tests (DeJong & Randolph, 2012), as discussed in Sections 1.3.6 and 2.3.14 of Volume I. Dissipation tests are valuable in clayey soils and they should be done whenever engineers judge that the value of the information obtained from the test justifies the expense for the site being investigated.

Volume I of the manual includes a synthesis of the work done by researchers on the aspect of penetration rate vis-à-vis the drainage conditions. The methodology proposed by DeJong et al. (2013) to address partial drainage conditions during cone penetration in intermediate soils is provided in Section 1.3.7 of Volume I. However, this methodology has not been standardized or formally adopted in practice.

APPENDIX E. RESIDUAL-STATE FRICTION ANGLE OF CLAY

The residual shear strength τ_r of clay is the product of the normal effective stress σ' on the shearing plane and the tangent of the residual-state friction angle ϕ_r, which in turn depends on the value of σ', the clay mineralogy, the clay fraction (CF), and the magnitude and rate of shear displacement. According to Skempton (1985), the shear displacements needed for an intact clay with CF > 30% and $\sigma' < 600$ kPa to attain residual-state friction angles of ϕ_r and $\phi_r + 1°$ range from 100–500 mm (4–20 in.) and 30–200 mm (1.2–8.0 in.), respectively. Based on the clay fraction of the soil, different residual-state shearing mechanisms are possible, resulting in different values of ϕ_r (Lupini, 1980; Lupini et al., 1981). Based on Skempton's observations on the variation of ϕ_r with the clay fraction of sand-bentonite mixtures tested in ring shear, Salgado (2006) proposed the following equation for ϕ_r of clay-silt-sand mixtures as a function of the clay fraction at a given stress level:

$$\phi_r = \phi_r\big|_{\text{pure clay}} + \left(\frac{\phi_{c,\text{mix}} - \phi_r\big|_{\text{pure clay}}}{27\%}\right)\left[52\% - \text{CF}(\%)\right] \qquad \text{(Eq. E.1)}$$

where $\phi_{c,\text{mix}}$ = critical-state friction angle of the clay-silt-sand mixture, and $\phi_r\big|_{\text{pure clay}}$ = residual-state friction angle of the clay fraction of the mixture. For CF ≤ 25%, the bulky sand/silt particles are likely to control the behavior of the mixture and thus $\phi_r = \phi_{c,\text{mix}}$, whereas for CF ≥ 52%, the platy/tube-like/needle-like clay particles are likely to control the behavior of the mixture and thus $\phi_r = \phi_r\big|_{\text{pure clay}} \approx 5°$, 10°, and 15° for montmorillonite, illite, and kaolinite clay minerals, respectively (Skempton, 1985). For intermediate values of CF between 25% and 52%, ϕ_r lies between $\phi_{c,\text{mix}}$ and $\phi_r\big|_{\text{pure clay}}$.

Besides the clay fraction and mineralogy, the residual-state friction angle ϕ_r also depends on the magnitude of the normal effective stress σ' acting on the shearing plane; ϕ_r decreases nonlinearly with increasing σ' (Figure E.1) because a larger normal stress forces greater realignment of clay particles in the direction of shearing. Soils with high clay fraction (CF ≥ 52%) and high smectite content, such as London clay, exhibit a significant drop in ϕ_r with increasing σ', while soils with low clay fraction (CF ≤ 25%) and low smectite content may not exhibit any residual behavior. Following the work by Maksimović (1989), ϕ_r can be expressed in terms of σ' using (Salgado, 2006):

$$\phi_r = \phi_{r,\text{min}} + \frac{\phi_c - \phi_{r,\text{min}}}{1 + \dfrac{\sigma'}{\sigma'_{\text{median}}}} \qquad \text{(Eq. E.2)}$$

where σ' = normal effective stress on the plane of shearing, $\phi_{r,\text{min}}$ = minimum residual-state friction angle (attained at large normal effective stress), ϕ_c = critical-state friction angle, and σ'_{median} = value of σ' at which the friction angle is equal to the average of $\phi_{r,\text{min}}$ and ϕ_c. At very large stresses, ϕ_r reaches an absolute minimum, denoted by $\phi_{r,\text{min}}$. For σ' on the shearing plane approaching zero, ϕ_r approaches the critical-state friction angle ϕ_c due to the negligible reorientation of the clay particles in the absence of a normal stress forcing this reorientation to happen.

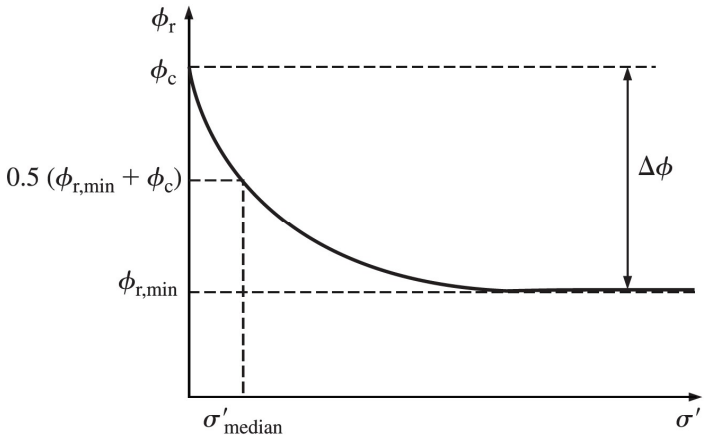

Figure E.1 Residual-state friction angle ϕ_r versus normal effective stress σ' on the shearing plane (Salgado, 2006).

Table E.1 summarizes the values of ϕ_c and $\phi_{r,min}$ of some well-known soils in the literature, such as Lower Cromer till, Boston blue clay, San Francisco bay mud, London clay, and Weald clay as a function of their CF and PI values. Although Lower Cromer till is a glacial till composed of sand (> 50%), clay (= 14%–20%), and almost no silt (Gens, 1982), it has been considered in the literature to behave like a "clay" but with no residual behavior. Boston blue clay is a low-plasticity, insensitive, marine clay, composed of illite and quartz (Terzaghi et al., 1996), and does not exhibit any residual behavior (Ladd & Edgers, 1972). San Francisco bay mud is a highly-plastic silt containing a large amount of clay-size particles (montmorillonite and illite), organic substances, shell fragments, and traces of sand (Bonaparte, 1982). London clay is composed of illite, kaolinite, montmorillonite, and quartz (Gasparre, 2005); both San Francisco bay mud and London clay exhibit residual strength with sustained shearing beyond the critical state. Figure E.2 illustrates the fit of Eq. E.2 to ring shear test data for Weald clay. The fit was done by first estimating the value of ϕ_c in triaxial compression (Parry, 1960) and then finding the values of σ'_{median} and $\phi_{r,min}$ that minimize the sum of least squares.

Table E.1 Critical-state and residual-state strength data for clayey soils reported in the literature

Soil	Mineralogy	CF (%)	PI (%)	A	ϕ_c (°)	$\phi_{r,\min}$ (°)	Reference
Boston Blue Clay	Illite, quartz	35	13.1	0.37	32.4[1]	—	Ladd & Varallyay (1965)
London Clay	Kaolinite, illite, montmorillonite, quartz	53–62	42–45	0.73–0.79	21.3	9.4[2]	Bishop et al. (1971); Gasparre (2005); Nishimura (2005)
Lower Cromer Till	Illite, calcite, quartz	14–20	10–12	0.60–0.71	30.0	—	Dafalias et al. (2006); Gens (1982); Lupini et al. (1981)
San Francisco Bay Mud	Illite, montmorillonite	47	47	1.00	28.9[1]	16.2	Kirkgard & Lade (1991); Meehan (2006)
Weald Clay	Illite, kaolinite, illite-montmorillonite, vermiculite	52	33	0.63	20.9	8.3[3]	Akinlotan (2017); Bishop et al. (1971); Parry (1960)

Note: CF = clay fraction, PI = plasticity index, A = activity (= PI/CF), ϕ_c = critical-state friction angle in triaxial compression, and $\phi_{r,\min}$ = minimum residual-state friction angle in ring shear.

[1] Extrapolated value corresponding to 30% axial strain (Chakraborty, 2009).

[2] Value corresponds to blue London clay at Wraysbury (CF = 57%, PI = 43%, A = 0.75). For brown London clay at Walthamstow (CF = 53%, PI = 42%, A = 0.79), $\phi_{r,\min}$ = 7.5° (Bishop et al., 1971).

[3] Obtained from the fit of Eq. E.2 to ring shear test data reported by Bishop et al. (1971).

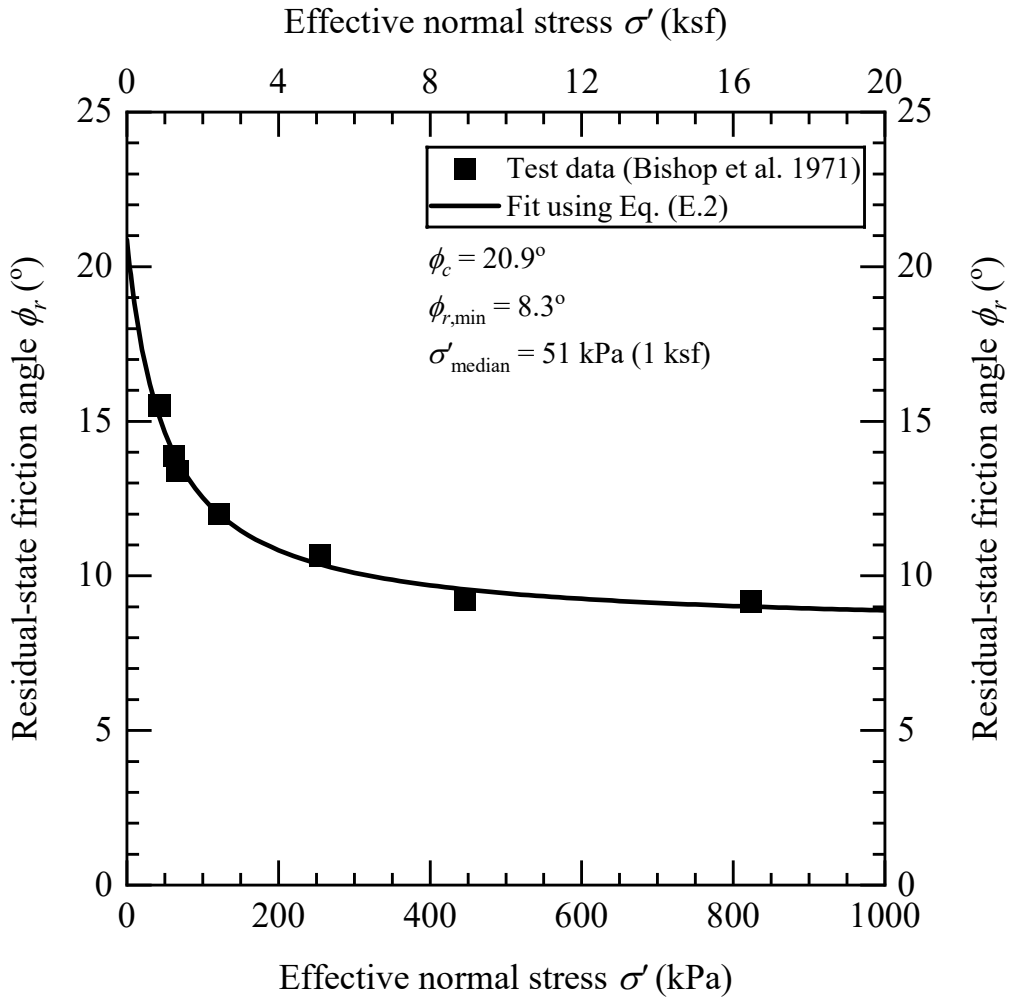

Figure E.2 Fit of Eq. E.2 to ring shear test data for Weald clay.

About the Joint Transportation Research Program (JTRP)

On March 11, 1937, the Indiana Legislature passed an act which authorized the Indiana State Highway Commission to cooperate with and assist Purdue University in developing the best methods of improving and maintaining the highways of the state and the respective counties thereof. That collaborative effort was called the Joint Highway Research Project (JHRP). In 1997 the collaborative venture was renamed as the Joint Transportation Research Program (JTRP) to reflect the state and national efforts to integrate the management and operation of various transportation modes.

The first studies of JHRP were concerned with Test Road No. 1—evaluation of the weathering characteristics of stabilized materials. After World War II, the JHRP program grew substantially and was regularly producing technical reports. Over 1,600 technical reports are now available, published as part of the JHRP and subsequently JTRP collaborative venture between Purdue University and what is now the Indiana Department of Transportation.

Free online access to all reports is provided through a unique collaboration between JTRP and Purdue Libraries. These are available at http://docs.lib.purdue.edu/jtrp.

Further information about JTRP and its current research program is available at http://www.purdue.edu/jtrp.

About This Report

An open access version of this publication is available online. See the URL in the citation below.

Sakleshpur, V. A., Prezzi, M., Salgado, R., & Zaheer, M. (2021). *CPT-based geotechnical design manual, Volume 2: CPT-based design of foundations—Methods* (Joint Transportation Research Program Publication No. FHWA/IN/JTRP-2021/23). West Lafayette, IN: Purdue University. https://doi.org/10.5703/1288284317347